

A THIN FILM TRANSISTOR DRIVEN MICROCHANNEL DEVICE  
FOR PROTEIN AND DNA ELECTROPHORESIS

A Dissertation

by

HYUN HO LEE

Submitted to the Office of Graduate Studies of  
Texas A&M University  
in partial fulfillment of the requirements for the degree of

DOCTOR OF PHILOSOPHY

December 2004

Major Subject: Chemical Engineering

A THIN FILM TRANSISTOR DRIVEN MICROCHANNEL DEVICE  
FOR PROTEIN AND DNA ELECTROPHORESIS

A Dissertation

by

HYUN HO LEE

Submitted to Texas A&M University  
in partial fulfillment of the requirements  
for the degree of

DOCTOR OF PHILOSOPHY

Approved as to style and content by:

---

Yue Kuo  
(Chair of Committee)

---

Jorge M. Seminario  
(Member)

---

Victor M. Ugaz  
(Member)

---

Ohannes Eknoyan  
(Member)

---

Kenneth. R. Hall  
(Head of Department)

December 2004

Major Subject: Chemical Engineering

## ABSTRACT

A Thin Film Transistor Driven Microchannel Device  
for Protein and DNA Electrophoresis. (December 2004)  
Hyun Ho Lee, B.S., Seoul National University, Seoul, Korea;  
M.S., Stanford University.  
Chair of Advisory Committee: Dr. Yue Kuo

Novel electrophoresis devices for protein and DNA separation and identification have been presented and studied. The new device utilizes a contact resistance change detection method to identify protein and DNA *in situ*. The devices were prepared with a microelectronic micromechanical system (MEMS) fabrication method. Three model proteins and six DNA fragments were separated by polyacrylamide gel microchannel electrophoresis and surface electrophoresis. The detection of the proteins or DNA fragments was accomplished using the contact resistance increase of the detection electrode due to adsorption of the separated biomolecules. Key factors for the success of these devices were the optimization of fabrication process and the enhancement of detection efficiency of the devices. Parameters, such as microchannel configuration, size of electrode, and affinity of protein or polyacrylamide gel to the microchannel sidewall and bottom surface were explored in detail. For DNA analysis, the affinity to the bottom surface of the channel was critical. The surface modification method was used to enhance the efficiency of the microchannel surface electrophoresis device. The

adsorption of channel separated protein and DNA on the detection electrode was confirmed with the electron spectroscopy for chemical analysis (ESCA) method. The electrical current (I) from the protein microchannel electrophoresis was usually noisy and fluctuated at the early stage of the electrophoresis process. In order to remove the current perturbation, an amorphous silicon (a-Si:H) thin film transistor (TFT) was connected to the microchannel device. The self-aligned a-Si:H TFT was fabricated with a two-photomask process. The result shows that the attachment of the TFT successfully suppressed the current fluctuation of the microchannel electrophoresis process. In summary, protein and DNA samples were effectively separated and detected with the novel TFT-driven or surface microchannel electrophoresis device.

To my wife, Haewon  
and  
my parents and brother

## ACKNOWLEDGMENTS

I am thankful to the Chemical Engineering Department at Texas A&M University for supporting my research and study. I would like to express my sincere gratitude to my advisor, Dr. Yue Kuo, for distributing his wisdom, experience, and knowledge, and for guiding and supporting my research efforts throughout my graduate studies. Through his teaching, I have learned the sincere spirit of being a researcher and scientist in the fields of industry and academia. All the difficulties during my study were overcome with his considerate advice and discussion.

I would like to thank Dr. Eknayan in the Electrical Engineering Department and Dr. Ugaz in the Chemical Engineering Department for serving on my committee and for allowing me to use several valuable sets of equipment in their laboratory. I also thank Dr. Seminario for his opinions and discussion on my research subjects.

I acknowledge Dr. W. M. Lackowski of the Center for Integrated Microchemical System in the Chemistry Department for his training and help in examining many samples with ESCA analysis. I appreciate my colleagues in the Thin Film Nano & Microelectronics Research Laboratory for their help in sharing various vacuum technologies and preparing samples. Especially, I would like to thank Mr. Randy Marek in the Chemical Engineering Machine Shop for his invaluable assistance in setting up the system at the beginning of the project, and repairing some equipment problems.

Finally, I would like to dedicate this work to my wife and family. This work could not be accomplished without their spiritual support.

## TABLE OF CONTENTS

	Page
ABSTRACT.....	iii
DEDICATION.....	v
ACKNOWLEDGMENTS.....	vi
TABLE OF CONTENTS.....	vii
LIST OF FIGURES.....	ix
LIST OF TABLES.....	xiv
 CHAPTER	
I INTRODUCTION.....	1
II LITERATURE REVIEW.....	7
1. Electrophoresis.....	7
1.1. Principle of Electrophoresis.....	7
1.2. Capillary and Microchip Electrophoresis.....	12
1.3. Electrophoresis of DNA.....	17
2. Plasma Thin Film Deposition Process.....	20
2.1. Fundamentals of Plasma.....	20
2.2. Plasma Phase Chemical Reactions.....	23
2.3. Plasma Enhanced Chemical Vapor Deposition.....	24
2.4. PECVD Thin Film.....	25
3. Thin Film Transistor.....	29
III EXPERIMENTAL METHODS.....	36
1. Thin Film Deposition Process.....	36
2. Reactive Ion Etching.....	38
3. Solid State Surface Analysis.....	38
4. Anisotropic Etching of Silicon Wafer.....	45
5. Biomolecule Sample Preparation and Assay.....	47
6. Fabrication of Microchannel for Protein Analysis.....	48
7. Affinity Experiment of Protein and DNA on Substrates.....	50

CHAPTER	Page
8. Surface Modification of Microchannel.....	52
9. Microchannel Electrophoresis Preparation for Protein Analysis.....	52
10. Microchannel Surface Electrophoresis Preparation for DNA Analysis.....	53
11. TFT Fabrication.....	57
12. Electrical Characterization of a-Si:H TFT.....	59
13. TFT-Microchannel Electrophoresis.....	61
 IV SURFACE MODIFICATION OF MICROCHANNEL.....	 63
1. Si Microchannel Fabrication.....	63
2. Surface Modification and Protein Affinity.....	64
2.1. Substrate Surface Structure Influence.....	66
2.2. Substrates Effects on Protein Affinity.....	73
2.3. Substrate Effects on Solution Affinity.....	75
3. Substrate Surface Influence on DNA Affinity.....	82
 V MICROCHANNEL ELECTROPHORESIS OF PROTEIN AND DNA	 90
1. Microchannel Electrophoresis for Protein Analysis.....	90
1.1. Adsorption of Protein on Electrode.....	90
1.2. Detection Electrode Contact Resistance vs. Device Configuration.....	91
1.3. Separation of Multiple Proteins in a Fluid Solution.....	97
1.4. Estimation of Adsorbed Proteins.....	109
2. Microchannel Surface Electrophoresis for DNA Analysis.....	112
2.1. DNA Electrophoresis on Solid Surface.....	113
2.2. Substrate and Buffer Effects on DNA Mobility.....	120
 VI THIN FILM TRANSISTOR DRIVEN ELECTROPHORESIS.....	 127
1. Characteristics of PECVD SiN <sub>x</sub> .....	127
2. Electrical Characteristics of a-Si:H TFT .....	138
3. Electrophoresis of TFT-Connected Microchannel Device.....	146
 VII CONCLUSIONS.....	 155
 REFERENCES.....	 159
 APPENDIX.....	 163
 VITA.....	 166



## LIST OF FIGURES

FIGURE		Page
1	Schematic illustration of mechanism of an electrophoresis.....	8
2	Coomasie blue R 250 stained protein bands of slab-type SDS-PAGE	10
3	Schematic diagram of laser induced fluorescent (LIF) system.....	15
4	(a) Simulated snapshot of DNA undergoing surface electrophoresis, and (b) electropherogram of $\lambda$ -Hind III digested DNA on an oxidized Si surface.....	19
5	Physical model of plasma state and dc voltage profile as a function of position in rf plasma.....	21
6	Cross-sectional view of an inverted staggered tri-layer a-Si:H TFT...	32
7	(a) Typical output characteristics curves based on the linear approximation of the velocity-field, and (b) typical transfer characteristic curves of field effect transistor (FET).....	34
8	Schematic diagram of plasma enhanced chemical vapor deposition (PECVD) reactor.....	37
9	Schematic diagram of an ellipsometer and light reflection.....	39
10	Schematic diagram of an X-ray photoemission.....	42
11	Schematic diagram of the operational principle of Fourier transformed infrared (FT-IR) spectroscopy.....	44
12	Schematic diagram of an experimental setup of potassium hydroxide (KOH) anisotropic Si etching.....	46
13	(a) Flow chart diagram of a Si microchannel device fabrication process, and (b) photograph of a completed Si microchannel electrophoresis device.....	49
14	(a) Flow chart diagram of the SU-8 microchannel device fabrication, and (b) photograph of the completed SU-8 microchannel on glass....	55

FIGURE	Page
15	Flow chart diagram for the fabrication of an inverted, staggered, tri-layer a-Si:H TFT..... 58
16	Electrical characterization setup of a-Si:H TFT and microchannel device connected to a-Si:H TFT..... 60
17	SEM of cross-section view of KOH Si-etched microchannel: (a) with 30.0% KOH solution at 70°C, (b) with 30.0% KOH including 3.0% IPA at 70°C..... 65
18	Chemical structure of cross-linked polyacrylamide gel..... 67
19	Chemical structure of negative photoresist SU-8..... 69
20	Photograph of gel shrinkage, microscopic pictures of compatibility between SU-8 channel and polyacrylamide gel: (a) with untreated microchannel, and (b) with O <sub>2</sub> plasma-treated (1 min) microchannel. 70
21	ESCA spectra of C <sub>1s</sub> : (a) untreated SU-8, (b) H <sub>2</sub> O/H <sub>2</sub> O <sub>2</sub> /H <sub>2</sub> SO <sub>4</sub> oxidized SU-8, (c) H <sub>2</sub> plasma-treated SU-8, (d) O <sub>2</sub> plasma-treated SU-8..... 72
22	ESCA spectra for remaining protein after affinity examinations on (a) the modified SU-8 (1 min) and (b) glass substrate..... 76
23	(a) Contact angle of DI water on the sputtered SiO <sub>2</sub> , and (b) contact angle of 0.5× TBE buffer with 0.2% SDS on the glass..... 78
24	Contact angle measurement of DNA solution on (a) glass substrate and (b) solution oxidized glass..... 83
25	ESCA spectra of Si <sub>2p</sub> : (a) bare Si, (b) H <sub>2</sub> O/H <sub>2</sub> O <sub>2</sub> /H <sub>2</sub> SO <sub>4</sub> oxidized Si, (c) H <sub>2</sub> plasma-treated Si, (d) glass, (e) H <sub>2</sub> O/H <sub>2</sub> O <sub>2</sub> /H <sub>2</sub> SO <sub>4</sub> oxidized glass, and (f) H <sub>2</sub> plasma-treated glass..... 87
26	Cross-sectional view of a microchannel device and the schematic resistance model of a corresponding circuit..... 92
27	The R <sub>total</sub> with combination of four kinds of channel cross-section sizes and four kinds of detection electrodes..... 94

FIGURE	Page
28	Measurement of the total resistance ( $R_{total}$ ) with or without gel in microchannel and protein loading at feed reservoir..... 96
29	Coomassie Brilliant Blue R250-stained protein profile on detection electrode..... 98
30	ESCA $N_{1s}$ and $S_{2p}$ spectra of the detection electrode surface: (a) with protein, and (b) without protein..... 100
31	The microchannel's (a) current <i>vs.</i> time (I-t), and (b) (dI/dt) <i>vs.</i> t curves replotting of current change with time (dI/dt-t) at different protein samples. The channel size has depth of 30.2 $\mu\text{m}$ , width of 440 $\mu\text{m}$ at the bottom and 530 $\mu\text{m}$ at the top. The channel is made of Si with sputtered $\text{SiO}_x$ surface. .... 101
32	The dI/dt <i>vs.</i> run time (dI/dt-t): (a) device with a channel depth of 20.3 $\mu\text{m}$ and detection electrode area of 3.0 $\times$ 1.5 $\text{mm}^2$ , (b) device with a channel depth of 30.2 $\mu\text{m}$ and detection electrode area of 1.4 $\times$ 1.5 $\text{mm}^2$ ..... 104
33	The protein mobility <i>vs.</i> the molecular weight of protein obtained from a conventional slab-type SDS-PAGE equipment, and from Fig. 32(a) and (b)..... 106
34	Current <i>vs.</i> gel run time (I-t): (a) the feed solution containing no protein, (b) the feed solution containing three proteins, (c) subtraction of (b) from (a)..... 110
35	(a) Schematic setup of electrophoresis on a completed microchannel device, and (b) photograph of UV exposed $\lambda$ -EcoR I digest DNA sample attached with the ethidium bromide fluorescent agent..... 114
36	ESCA spectra of the detection electrode surface: (a) $N_{1s}$ and (b) $P_{2p}$ .. 115
37	The dI/dt-t for electrophoresis of $\lambda$ -EcoR I digest DNA fragments on glass and Si microchannels. The channel was made of SU-8 sidewall and glass or Si bottom surface with depth of 35 $\mu\text{m}$ , width of 485 $\mu\text{m}$ , and length of 0.5 cm..... 117

FIGURE	Page
38	Log scale of mobility <i>vs.</i> log scale of No. basepair of $\lambda$ -EcoR I digest DNA fragments on (a) oxidized glass surface, and (b) oxidized Si surface microchannel..... 119
39	Current <i>vs.</i> time (I-t) with the buffer solution not loaded with DNA. The channels were made of SU-8 sidewall and Si bottom surface with depth of 35 $\mu\text{m}$ , width of 485 $\mu\text{m}$ , and length of 0.5 cm as untreated, $\text{H}_2\text{O}/\text{H}_2\text{O}_2/\text{H}_2\text{SO}_4$ oxidized, and $\text{H}_2$ plasma-treated..... 121
40	The current <i>vs.</i> time (I-t) curves of DNA surface electrophoresis with different buffer concentration (0.1 $\times$ , 0.5 $\times$ , 1.0 $\times$ , 2.0 $\times$ , and 5.0 $\times$ TBE). The channel was made of a SU-8 sidewall and Si bottom surface with a depth of 35 $\mu\text{m}$ , width of 485 $\mu\text{m}$ , and length of 0.5 cm. The entire Si wafer devices were (a) $\text{H}_2\text{O}/\text{H}_2\text{O}_2/\text{H}_2\text{SO}_4$ solution-oxidized or (b) $\text{H}_2$ plasma-treated. .... 123
41	The $dI/dt$ -t curves of a microchannel surface electrophoresis on (a) oxidized and (b) $\text{H}_2$ plasma-treated microchannels with SU-8 sidewall and Si bottom surface in 0.1 $\times$ , 0.5 $\times$ , 1.0 $\times$ and 2.0 $\times$ TBE buffer..... 125
42	Mobility of 3.5 kbp fragment of $\lambda$ -EcoR I digest DNA <i>vs.</i> buffer concentration on (a) oxidized and (b) $\text{H}_2$ plasma-treated microchannels..... 126
43	PECVD $\text{SiN}_x$ deposition rate as a function of temperature at various plasma powers..... 128
44	PECVD $\text{SiN}_x$ refractive indices as a function of temperature at various plasma powers..... 130
45	FT-IR spectra of PECVD $\text{SiN}_x$ films: (a) at 100 $^\circ\text{C}$ , 150 $^\circ\text{C}$ , 200 $^\circ\text{C}$ and 250 $^\circ\text{C}$ with 700W rf power and (b) comparison of characteristic peaks of 100 $^\circ\text{C}$ $\text{SiN}_x$ films with various rf powers..... 131
46	ESCA spectra of $\text{Si}_{2p}$ peak of $\text{SiN}_x$ films: at 100 $^\circ\text{C}$ , 150 $^\circ\text{C}$ , and 250 $^\circ\text{C}$ with 500 W..... 133
47	Etch rate profile with various refractive index films from 100 $^\circ\text{C}$ , 150 $^\circ\text{C}$ , 200 $^\circ\text{C}$ , and 250 $^\circ\text{C}$ ..... 136

FIGURE	Page
48	I-V characteristics of metal-insulator-semiconductor (MIS) structure (Al-SiN <sub>x</sub> -Si wafer)..... 137
49	Output characteristics of an a-Si:H TFT, I <sub>ds</sub> vs. V <sub>ds</sub> ..... 139
50	Transfer characteristics of an a-Si:H TFT, I <sub>ds</sub> vs. V <sub>g</sub> ..... 140
51	Refractive index effect on TFT threshold voltage V <sub>th</sub> , PECVD SiN <sub>x</sub> at 500 mTorr, 250°C..... 142
52	Refractive index effect on TFT field effect mobility μ <sub>eff</sub> , at 500 mTorr, 250°C..... 144
53	Refractive index effect on TFT I <sub>on</sub> /I <sub>off</sub> ratio, PECVD SiN <sub>x</sub> at 500 mTorr, 250°C..... 145
54	TFT-connected microchannel device: (a) an inverted staggered tri-layer a-Si:H TFT-connected to the microchannel device, and (b) the equivalent circuit..... 148
55	The I-t curves of (a) the TFT alone, (b) the TFT-connected gel-filled microchannel with no protein in the feed reservoir, and (c) the TFT-connected gel-filled microchannel with protein in the feed reservoir.. 149
56	The dI/dt-t curves: (a) a gel-filled Si-based microchannel device, (b) a gel-filled SU-8 microchannel device, and (c) a gel-filled SU-8 microchannel device connected to a TFT..... 151
57	The protein mobility vs. the molecular weight of protein by electrophoresis: (a) a slab-type SDS-PAGE, (b) a gel-filled Si-based microchannel device, (c) a gel-filled SU-8 microchannel electrophoresis device, and (d) a gel-filled SU-8 microchannel electrophoresis device connected to the TFT..... 153

## LIST OF TABLES

TABLE		Page
I	Characteristics of microchip-type electrophoresis.....	13
II	Material properties of SiN <sub>x</sub> film.....	26
III	Physical properties of typical high quality a-Si:H.....	28
IV	Numerical table for modified least square method (Savitsky-Golay) with order 3.....	54
V	Percentage of carbon functional groups in untreated and O <sub>2</sub> plasma-treated SU-8 surface.....	74
VI	Contact angles of various solutions on various substrates.....	79
VII	Contact angle of DNA solution on various substrates.....	84
VIII	Contact angle of DNA solution on various modified substrates.....	86
IX	Analysis of electrophoresis performance of device (a) and device (b) by theoretical plate (N) and resolution (R).....	108
X	FT-IR N-H/Si-H peak ratio and ESCA atomic N/Si ratio of SiN <sub>x</sub> as a function of plasma power.....	135

## CHAPTER I

### INTRODUCTION

Separation and identification of biomolecules, such as protein and DNA, are important in the biological and biomedical fields. The identification of biomolecules is often dependent upon fundamental information, such as the size, of the protein or DNA.<sup>1</sup> The separation and identification of biomolecules is commonly done by electrophoresis. Electrophoresis is based on the principle that when a current is passed through a column or slab that contains a molecular sieving medium, charged biomolecules in the feed solution migrate through the medium at different rates due to the size-to-charge ratio difference. So far, various electrophoresis methods, such as slab-gel electrophoresis, capillary electrophoresis, and microchip-based electrophoresis, have been developed and introduced. The sodium dodecyl sulfate (SDS) polyacrylamide gel electrophoresis (PAGE) has been widely used for the separation of proteins. The SDS-attached protein molecules are negatively charged and move toward the anode under an applied electric field. Proteins of different sizes migrate at different rates in the gel phase and are eventually separated into various bands within the gel.<sup>1-3</sup>

Recently, due to the advantages of the microelectronic and micromechanical fabrication process, microchip-based electrophoresis systems have been actively investigated.<sup>2-9</sup>

---

This dissertation follows the style of the *Journal of the Electrochemical Society*.

Substrates that have been used in the microchip-based systems include glass, polymer, and silicon wafer. Protein and DNA could be separated with the microfabricated channel device with or without the existence of polyacrylamide gel in the channel region. For example, microchannel devices with channel dimensions of 9-40  $\mu\text{m}$  deep, 45-100  $\mu\text{m}$  wide, and 4.5-4.9 cm long were fabricated from a Pyrex glass or borofloat glass substrate.<sup>4-8</sup> Protein and DNA were separated, by this kind of device without the presence of gel in the channel, under a high electric field of 100-600 V/cm.<sup>4-8</sup> Advantages of this kind of device include a small sample volume, short separation time, and a low sample concentration. However, it also has some disadvantages. For example, the separated proteins need to be labeled with chemicals, such as fluorescent derivatizing reagents, which is a time-consuming process. In addition, the labeled protein or DNA has to be detected with a complicated optical equipment such as a laser-induced fluorescence (LIF) system.<sup>4-8</sup>

Recently, Kuo and Lee reported a new concept of a microchannel-based SDS-PAGE system, that separated and identified proteins from a mixture *in situ* without applying the protein labeling procedure.<sup>9-11</sup> The device could be prepared from either a silicon wafer or a glass substrate. For the glass substrate, a special type of negative photoresist, *i.e.*, SU-8, was selected because it is easily fabricated into a high aspect ratio channel structure.<sup>9,10</sup>

In the conventional electrophoresis system, proteins are separated into different bands and stay within the gel phase. However, with this new microchannel electrophoresis, all separated proteins pass through the gel into a detection reservoir.



Once arriving in the detection reservoir, the proteins quickly migrate to the detection electrode and are strongly adsorbed to the surface. The contact resistance between the solution and the detection electrode is drastically increased during the process, which causes a drastic decrease of the current passing through the device.

The phenomena of the protein adsorption on the metal surface have been extensively studied in the biomedical field.<sup>12</sup> For example, proteins such as human serum albumin (HSA) can be irreversibly adsorbed on a metal electrode.<sup>13</sup> The protein adsorption process is affected by various parameters and can be greatly accelerated by the application of a positive potential to the electrode.<sup>12-14</sup> In addition, the chemical constituent of the protein is critical to the adsorption process. Therefore, for the new microchannel electrophoresis device described in the previous section, a large drop of the current ( $I$ ) can be detected when protein molecules are adsorbed on the electrode surface. The time of the current drop corresponds to the arrival time of the specific strain of protein. Therefore, proteins are separated and identified with this kind of device.

Although the concept of the device has been proven, many detailed issues still need to be investigated. In this dissertation, influences of various geometric factors, such as the channel configuration and detection electrode size, to the device performance, were studied. The probability of quantifying the amount of protein in the feed solution using the  $I$ - $t$  (current vs. time) data was also investigated. Surface chemistry is of prime importance for the performance of the microchannel device.<sup>6,11</sup> This is especially true when a glass substrate and a polymer channel are used in the structure. Among several surface modification methods, the oxygen ( $O_2$ ) plasma is a possible candidate for adding

active functional groups to the polymer surface. The O<sub>2</sub> plasma can hydrophilize the polymer surface and degrade polymer into low molecular units.<sup>15</sup> In this dissertation, protein adsorption and gel compatibility to various modified surfaces were investigated. The O<sub>2</sub> plasma-treated surface was analyzed with physical and chemical methods. The suitability of the modified surface for the microchannel applied was discussed with respect to its surface structure.

In the new microchannel electrophoresis device, another detailed issue needs to be investigated. At the early operation stage, the current fluctuates drastically, and it is difficult to differentiate between the fluctuation peak and the protein detection peak. In order to diminish the current fluctuations during the electrophoresis, an amorphous silicon (a-Si:H) thin film transistor (TFT) is connected to the microchannel device. A-Si:H TFTs have been applied to many microelectronic devices such as liquid crystal displays (LCDs), x-ray medical imagers, radiation and chemical detectors, facsimile, digital image sensors, and bioanalytical sensors.<sup>16-18</sup> Substrates for these applications can be glass, polymers, and steel foils. The a-Si:H TFTs are commonly fabricated by plasma enhanced chemical vapor deposition (PECVD), which has the advantage of low temperature and good uniformity over a large area. In general, the PECVD SiN<sub>x</sub> is the most common dielectric material for an a-Si:H TFT. Since an a-Si:H TFT has a stable drain current ( $I_d$ ) under normal operation conditions, when connected to the microchannel electrophoresis device to eliminate the signal noise, it can be used as a current stabilizer. In principle, the microchannel electrophoresis can be taken as a variable resistor in which the resistance increases drastically with the arrival of a protein

to the detection electrode. Since the *a*-Si:H TFT can be fabricated on a low-temperature substrate using only two photomasks,<sup>17,18</sup> the addition of the TFT to the microchannel device causes little complication to the entire fabrication process.

With the surface modification method, a new type of surface electrophoresis device can be used for DNA analysis. The substrate can be made of glass or silicon while the microchannel structure can be made of polymer, such as SU-8. According to the Pernodet *et al.*'s report, if the surface movement of DNA is restricted to the microchannel area, the electrophoresis function can be improved.<sup>19,20</sup>

In this dissertation, the microchannel electrophoresis device was used for protein analysis, and the surface electrophoresis was used for DNA analysis.

Chapter II reviews the theoretical background of the electrophoresis for both protein and DNA analysis. The principle of the surface electrophoresis for DNA analysis is also presented. For the basic microelectronic fabrication process, the PECVD process and the TFT characteristics are presented.

Chapter III describes the experimental methods and procedures of the microchannel device.

Chapter IV discusses the interactions between the microchannel surface and the protein or DNA molecule. The effects of the surface modification method to the microchannel surface and physical and chemical properties are also discussed. Based on the result, optimized modification conditions were selected for the protein or DNA analysis.

Chapter V includes results of microchannel electrophoresis on protein and DNA molecules. The separation efficiency of the device was also studied and discussed.

Chapter VI presents the electrical performance of the a-Si:H TFT with respect to different SiN<sub>x</sub> gate dielectric films. The improvement of the detection signal with the addition of a TFT to the microchannel electrophoresis is discussed.

Finally, Chapter VII summarizes the studies.

## CHAPTER II

### LITERATURE REVIEW

#### 1. Electrophoresis

##### 1.1. Principle of Electrophoresis

A charged molecule migrates when it is placed in an electrolyte solution under an electric field. Biomolecules, such as protein and DNA, carry a net charge at certain pH levels other than their isoelectric points. Based on the principle of the biomolecule's movement, an analytical method, *i.e.*, electrophoresis, was developed in a proper pH buffer solution.<sup>1</sup> The speed of migration depends upon the ratio of the charge number to the mass of the molecule. Since the surface charge number of a protein or DNA molecule is linearly proportional to the size of the molecules, protein or DNA molecules can be separated by their size difference.<sup>2</sup> Figure 1 shows the mechanism of protein or DNA molecule separation with the electrophoresis time. Bands are formed as the electrophoresis time increases. The molecular bands can be formed with or without the existence of a molecular sieving material, such as gel, in the capillary or microchannel region of the electrophoresis device. The polyacrylamide polymer is the most commonly used molecular sieve material. Polyacrylamide gel electrophoresis (PAGE) has been shown to be a very powerful method for the fractionation or separation of proteins and DNA.<sup>1,2</sup> There are two critical reasons for applying gel in electrophoresis: *(i)* it suppresses convective flows produced by small gradients of temperature and ion concentration, and *(ii)* it serves as molecular sieves to enhance the separation efficiency.<sup>1</sup>

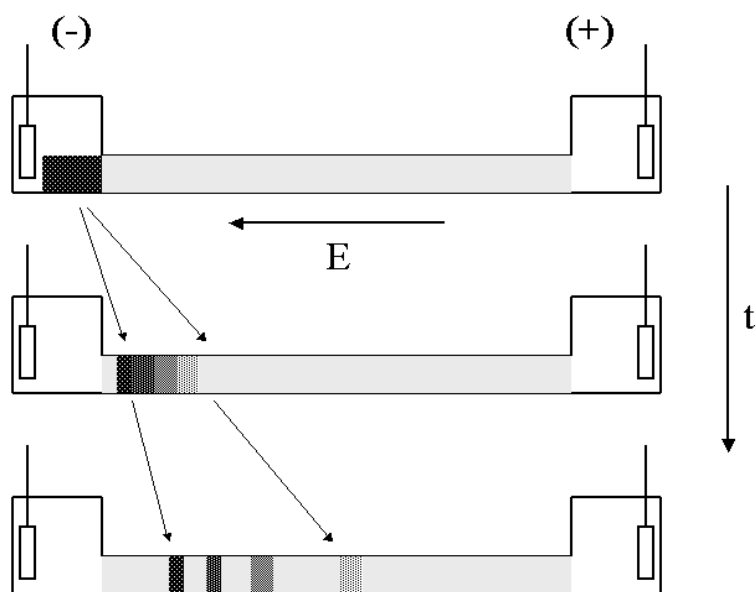


Figure 1. Schematic illustration of mechanism of an electrophoresis. (reference<sup>1,3</sup>)

The gel can be replaced by other porous materials, such as cellulose acetate, silica, alumina, cellulose, agarose, and starch. The polyacrylamide is easy to be formed in the gel structure. The conventional polyacrylamide gel electrophoresis is in the slab form.

Figure 2 shows an example of a typical sodium dodecyl sulfate (SDS) PAGE slab-gel electrophoresis with protein bands. The protein sample is loaded into a well located on the top of the gel. An electric field is applied between the two ends of the gel slab. The separated proteins remain inside of the gel and need to be stained by blue dye, such as Coomassie Brilliant Blue R250. Each stained band in Fig. 2 represents a certain size of the protein molecule. The gel solution and the sample loading or detecting reservoir contain a small amount (0.1%) of SDS to denature the protein molecule.<sup>1-3</sup>

The SDS is an anionic detergent that disrupts nearly all non-covalent interactions in a native protein. The SDS-to-protein binding ratio is 1.4:1, or each SDS is bound to two amino acid groups.<sup>3</sup> Through the binding process, the SDS confers a negative charge to the polypeptide. The amount of charge is proportional to its length. The denatured polypeptide has a rod or sphere shape surrounded with a negative charge cloud. An equal number of charges is attached with each unit length. Therefore, the migration of the peptide is determined not only by its intrinsic electrical charge but also by its molecular weight. When the negatively-charged cloud is assumed to be a sphere, the frictional force,  $f$ , which is balanced or equivalent to the electrostatic force,  $qE$ , the during the migration on a molecule can be expressed by Stokes' law as below:

$$f = qE = 6\pi r v \eta \quad [1]$$

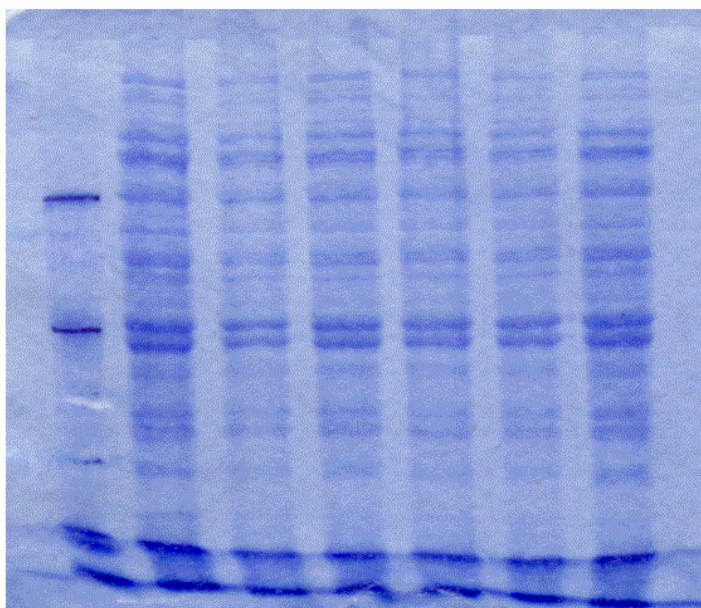


Figure 2. Coomassie blue R 250 stained protein bands of slab-type SDS-PAGE.  
(reference<sup>1</sup>)



where  $q$  is the total surface charge of the molecule,  $E$  is the electrical potential,  $r$  is the radius of the spherical or ellipsoidal molecule,  $v$  is the migration speed, and  $\eta$  is the viscosity of gel. Where  $d'$  is the distance of the region and  $V$  is the applied voltage through the gel length, the electrical potential  $E$  is expressed as below:

$$E = \frac{V}{d'} \quad [2]$$

The mobility of molecule,  $m$ , can be obtained as below:

$$m = \frac{d'd}{tV} = \frac{d}{tE} = \frac{v}{E} \quad [3]$$

where  $v = d/E$ ,  $d$  is the molecule running distance, and  $t$  is the protein running time. Conventionally, for a protein passing through a 5.0% or 10.0% PAGel, its mobility can be calculated as below:

$$\log m = \log m_o - K_R T \quad [4]$$

where  $T$  is the gel concentration,  $m_o$  is the free mobility without any gel concentration ( $T=0$ ), and  $K_R$  is the retardation coefficient.<sup>2</sup> Equation [4] indicates that the mobility decreases exponentially with the increase of the gel concentration for the same sized-protein. The  $K_R$  value is determined by the ionic strength of the buffer solution and the purity of the protein.<sup>3</sup> For different sized-proteins, the mobility,  $m$ , can be expressed from the relationship of the migration speed,  $v$ , by equations [1] and [3] as below:

$$m = \frac{v}{E} = \frac{q}{6\pi\eta r} \quad [5]$$


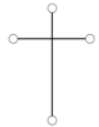

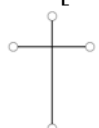
where the mobility is a function of the size of the different molecule,  $r$ , under same electrophoresis conditions.<sup>2</sup>

## 1.2. Capillary and Microchip Electrophoresis

The conventional SDS-PAGE can be used to determine the size of the protein or DNA molecule by comparing its mobility with that of a known size protein, *i.e.*, a marker. By measuring the migration length of the marker's band, the speed of the specific protein or DNA can be obtained by the calculation shown in equation [3]. Therefore, every electrophoresis experiment requires an extra slab to have the marker through the gel. The conventional SDS-PAGE or slab-type gel electrophoresis has many disadvantages, such as a long operation time, a large volume of sample, and band broadening. In order to overcome the difficulties of the slab-type system, many microchip or capillary electrophoresis (CE) systems have been developed.<sup>3-7</sup> Among the disadvantages, the band broadening is from a heterogeneous protein with an additional chemical group, such as a fluorescent labeling agent, and non-specific interaction between proteins and a charged inner-slab surface, which occurs under an electric field.<sup>3</sup> However, the band broadening is also frequently reported in the CE using a long glass tube (> 1.0 cm) and the microchip electrophoresis which uses a narrow microchannel on a glass.<sup>4</sup> Therefore, if the band broadening could be adequately controlled, a high separation efficiency is feasible with CE or microchip electrophoresis.<sup>3-5</sup> Protein separation systems with CE or microchip electrophoresis have been infrequently reported because of the difficulties in identification of protein bands at a specific detection position.<sup>5,7</sup>

Table I shows the characteristics of microchip electrophoresis systems from recent reports.<sup>4-8</sup> Most systems used the glass substrate.

Table I. Characteristics of microchip-type electrophoresis.

Method	Device size	Detection/Separation	Comment
T-junction injector [ref. 5] 	49 mm (l) × 66 – 25 μm (w) × 14 μm (d)	LIF, post -labeling No gel	Glass substrate, Electric field (1.6 kV/cm)
Cross-junction injector [ref. 6] 	49 mm (l) × 45 μm (w) × 9 μm (d)	LIF, pre -labeling No gel	Glass substrate, Electric field (0.6 kV/cm)
Cross-junction injector [ref. 7] 	45 mm (l) × 20 – 100 μm (w) × 40 μm (d)	LIF, pre -labeling Polyacryl-amide gel	Glass substrate, Electric field (0.2-1 kV/cm)
Cross-junction injector [ref. 8] 	5 mm (l) × 400 μm (w) × 40 μm (d)	LIF, pre -labeling Polyacryl-amide gel	Glass substrate, Electric field (20 V/cm)

The channel length ranged from 5 mm to 49 mm. All systems in Table I used a laser-induced fluorescence (LIF) technique to detect the separated protein bands. The LIF system is operated by exciting the fluorescent chemical attached to the protein with a laser light.<sup>5-7</sup> There are some disadvantages of these systems. For example, the labeling of protein is a complicated procedure.<sup>4-8</sup> Fluorescent reagents must be used before or after electrophoresis, and the sample needs to be incubated for a long time. In addition, if the labeled protein or DNA is detected with a LIF system, complicated optical equipment must be used.<sup>4-8</sup> Figure 3 shows the details of the basic mechanism of the LIF system. In order to detect movement of charged particles, laser light is focused near the end of the channel where the charged particles migrate. A green light with a wavelength of 488 nm is often used, and the fluorescence of the labeled protein or DNA can be detected by a photomultiplier.

The CE or microchip electrophoresis has many advantages over the conventional slab-type electrophoresis.<sup>3</sup> A major problem of protein separation with a CE or microchip electrophoresis is the adsorption of protein molecules to the capillary or microchannel glass wall, where an ion-exchange mechanism exists between the protein or DNA and silica surface. There can be several solutions for this problem: *(i)* the pH value of the buffer solution can be adjusted to ensure that the capillary wall and protein have the same charge polarity, *(ii)* the silica surface of the capillary or microchannel glass wall can be coated with a linear polyacrylamide or other hydrophobic functional polymer, and *(iii)* the high ionic strength or buffers containing a high concentration of alkali salts can be used.<sup>3,4,6,7</sup>

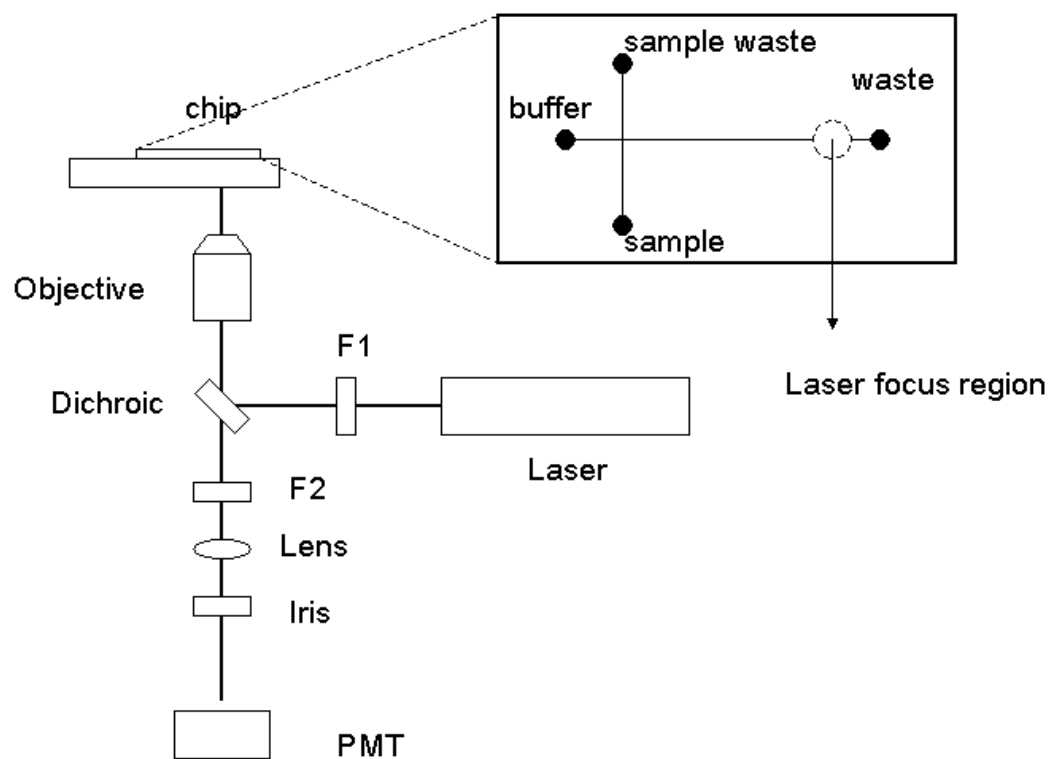


Figure 3. Schematic diagram of laser-induced fluorescent (LIF) system. (reference<sup>4</sup>)

The removal of joule heating is critical to the success of the linear polyacrylamide or other hydrophobic functional polymer.<sup>6</sup> One of the main drawbacks of a cross-linked polyacrylamide gel in the LIF system is the lack of low UV transparency of the gel in the on-column detection. Furthermore, cross-linked gels are heat-sensitive. When the temperature of the channel is high, bubbles are frequently formed, which block the current flow.<sup>2,3</sup> Another major problem of microchip electrophoresis is the low protein sensitivity.<sup>4,5</sup> The detection sensitivity could be improved by methods such as concentrating the sample through stacking by repetitive sample loading,<sup>3</sup> increasing the injection channel potentials between the sample and sample waste reservoir in Fig. 3 during separation to eliminate separation to reduce leakage,<sup>4</sup> or using better optics: a brighter source and a more sensitive photon detector. Automation would be another method for improvement.<sup>3</sup> In general, proteins are more difficult to detect with the microchannel device than DNA, because proteins have a stronger tendency to adsorb on the glass capillary wall.

Recently, Kuo and Lee reported a new microchannel device that separated and detected proteins in one step.<sup>9-11</sup> No optical identification procedure is required in this new method. The protein detection is based on the principle of a drastic increase of the contact resistance at the detection electrode surface during the adsorption of protein molecules. Therefore, the drawbacks from the usage of the LIF can be avoided, and the separated protein can be easily identified from the current vs. time (I-t) curve.

### 1.3. Electrophoresis of DNA

Electrophoresis of DNA is used for two purposes. One is to analyze the sequential composition of DNA nucleotides, Adenine (A), Guanine (G), Cytosine (C), and Thymine (T) by the PAGE with a high concentration gel or CE, which requires very high separation efficiency. The other purpose is to separate and identify relatively large-sized DNA molecules ( $> 0.5$  kbp (kilo-basepair)) for the cloning experiment.<sup>1,2</sup> Conventionally, the electrophoresis of large-sized DNA can be performed with a polyacrylamide or an agarose gel. Because of its easy handling, the agarose gel, which requires simple heating in the gel formation process, is widely used for the large-sized DNA. However, there are three advantages of polyacrylamide gel over agarose gel: (i) a greater resolving power, (ii) suitable for much larger quantities of DNA, and (iii) easy to recover DNA with high purity.<sup>1,2</sup> For an agarose gel, a low operation voltage is required to prevent the denaturing of double strand DNA by overheating, while a non-denaturing polyacrylamide gel can be used at a high operation voltage. Since the DNA molecule is larger than a protein molecule, a high gel concentration or a long capillary or microchannel is not useful for the separation of the large-sized DNA. For example, a low-concentration polyacrylamide gel, *e.g.*, containing 3.5% acrylamide, cannot resolve DNA larger than 2.0 kbp. The minimum practical acrylamide concentration for the gel formation is 3.0%. Therefore, a large pore-sized material such as agarose gel is suitable for the large-sized DNA electrophoresis. For the fabrication of a microchannel or a capillary electrophoresis, the agarose gel is not appropriate because the gel-formation process requires a high temperature. The high temperature can cause drastic gel

shrinkage inside of the capillary or microchannel after the gel formation. It is desirable to develop a new DNA electrophoresis method that does not require the agarose gel.

When a DNA molecule is adsorbed on a flat surface, its segments are present as either loops or tails. This is due to the balance between the loss of entropy from the localization of the molecule at the surface, and the increase of energy on adsorption of the molecule. When an electric field is applied parallel to the plane surface, the response of the molecule to the field is a function of its conformation on the surface. The mobility of the molecule along the surface is dependent upon its length. The above molecule migration phenomenon is called surface electrophoresis. Recently, Pernodet *et al.* reported the first surface electrophoresis system using an oxidized rectangular silicon surface.<sup>19</sup> Figure 4 shows (a) a simulated snapshot of DNA undergoing the surface electrophoresis, and (b) the electropherogram of  $\lambda$ -Hind III digested DNA on an oxidized Si surface.<sup>19,20</sup> Under an electric field, the loops and tails of the DNA strand repeatedly bind or detach from the oxidized Si surface while moving toward the positive electrode. In order to improve the affinity of the surface to DNA, it can be coated with a thin film of silicon containing polymer.<sup>20</sup> Surface electrophoresis is a good substitute for capillary or gel electrophoresis of large-sized DNA. As described above, the mechanism of the surface electrophoresis is fundamentally different from that of the polyacrylamide or agarose gel electrophoresis using the sieving effect.<sup>7,8</sup> The separation efficiency of the surface electrophoresis, *e.g.*, resolution, is a complicated function of the surface structure and chemical state of the substrate.<sup>20</sup> Therefore, a detailed analysis of the surface modification is most critical.



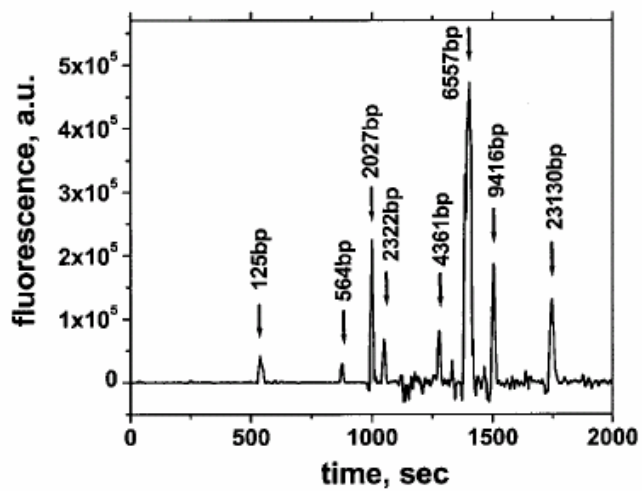
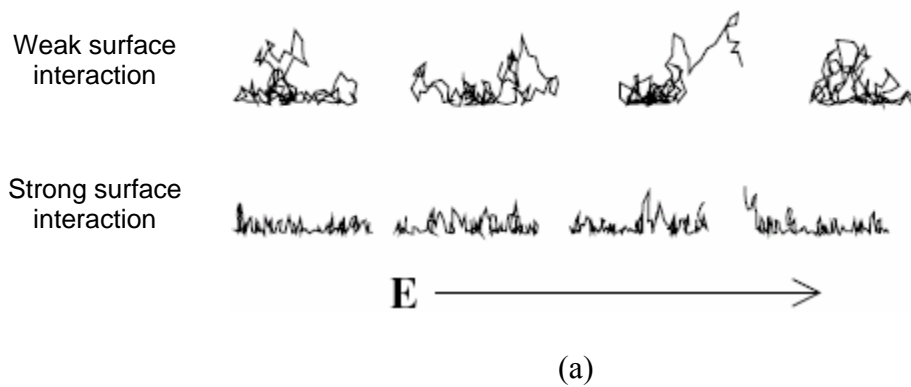


Figure 4. (a) Simulated snapshot of DNA undergoing surface electrophoresis, and (b) electropherogram of  $\lambda$ -Hind III digested DNA on an oxidized Si surface. (reference<sup>19,20</sup>)

## 2. Plasma Thin Film Deposition Process

### 2.1. Fundamentals of Plasma

Plasma processing is one of the most critical processes in microelectronics fabrication because it has many advantages over other fabrication methods. For example, plasma enhanced chemical vapor deposition (PECVD) can be used to deposit a uniformly thin film layer at a low temperature.<sup>21-23</sup> Thin film characteristics depend upon the conditions of the plasma, such as the generation of reactive radicals and ions. Therefore, it is necessary to discuss the basic background of plasma and plasma processing.

Plasma is composed of free charged particles, radicals, atoms, and molecules. It is electrically neutral. In microelectronics processing, weak plasma discharges are used. The extent of excitation and ionization is small. Typically the radicals may constitute 1.0% of the total plasma, and the total charged species may be less than 0.01%.<sup>22</sup> An electrically driven plasma is generated and sustained by the following mechanism: Electrons from an applied electric field randomly collide with molecules. Once the energy of the electrons is high enough to dissociate gas molecules, the electron energy can be transferred to molecules by elastic collisions. The elastic collisions produce activated radicals, ions, and neutrals. The plasma is sustained as long as the electric field is supplied.<sup>22,23</sup>

Figure 5 shows a typical electrically driven plasma diagram in a parallel-plate electrode. Within the plasma, the electron density above the electrode is too small for appreciable emission of light.

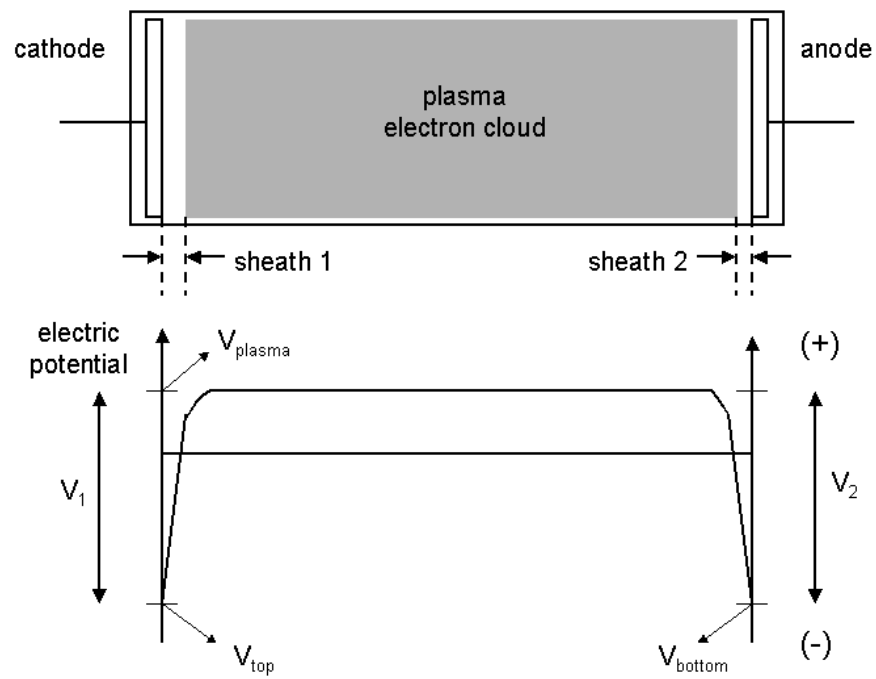


Figure 5. Physical model of plasma state and dc voltage profile as a function of position in rf plasma. (reference<sup>21,22</sup>)

The low light emission space is called a dark space or a sheath, as shown in Fig. 5.<sup>21,22</sup> Under dc plasma, ions in the plasma-phase strike the surface of the substrate, and it becomes charged. The charge accumulates on the surface until the dc plasma is extinguished. To solve this problem, the plasma can be driven by an ac signal.<sup>22</sup> At low frequencies, the plasma follows the excitation, and the width of the dark spaces above the electrodes pulses with the applied signal. Since the plasma is conductive, there is no significant potential drop across the plasma-phase. When the rate of excitation is greater than 10 kHz, the slow ions in the plasma cannot follow the voltage change. However, electrons are rapidly accelerated. During alternate half cycles, electrons strike the surface of each electrode, giving to both electrodes a net negative charge with respect to the plasma. It explains the mechanism of forming the sheath region in the vicinity of each electrode, as shown in Fig. 5.<sup>21-23</sup>

The simplest plasma reactor consists of two parallel-plate electrodes in a chamber that is maintained at a low pressure (under vacuum). The electrons, responding to an electric field produced by a radio frequency (rf) driving voltage, collide with molecules to generate reactive species. The reactive species exist in the central region where the plasma discharge produces lights of various wavelengths. The visible and UV light can be utilized for the analysis of the plasma state. In the central region, electron flux,  $n_e$ , is the same as ion flux,  $n_i$ , and there is no potential drop, so the region is considered a good conductor.

Near the electrodes, electrons diffuse quickly and are quickly recombined at the electrode, but ions do not. This makes  $n_i \gg n_e$  and creates an excess positive charge near

the electrodes. Since the region is a bad conductor, a positive potential drop with respect to the electrode exists. Due to the electron depletion, large dc voltage drops exist between the plasma and the electrodes, as expressed below:

$$V_1 = V_{plasma} - V_{top} \quad [6]$$

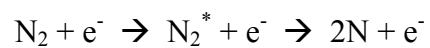
$$V_2 = V_{plasma} - V_{bottom} \quad [7]$$

These potential drops are responsible for the ion bombardment energy on the cathode electrode, since positive ions are accelerated through the sheath region.

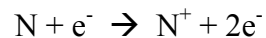
## 2.2. Plasma Phase Chemical Reactions

Several species (ions, electrons, radicals, and atoms) are produced in the plasma by collisions between electrons and molecules, or between molecules themselves. For example, in  $N_2$  plasma, the plasma species are produced through following reaction paths.<sup>21</sup>

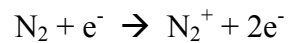
### 1) Dissociation



### 2) Atomic ionization



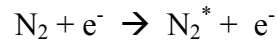
### 3) Molecular ionization



### 4) Atomic excitation



### 5) Molecular excitation



Here,  $\text{N}^*$  and  $\text{N}_2^*$  are the excited species. The species produced in  $\text{N}_2$  plasma are  $\text{N}$ ,  $\text{N}_2^*$ ,  $\text{N}_2$ ,  $\text{N}^+$ ,  $\text{N}^-$ , and  $\text{N}_2^+$ . The major neutral species are atomic  $\text{N}$  and  $\text{N}_2$ . The main ions are  $\text{N}^+$  and  $\text{N}_2^+$ .<sup>21,22</sup> The concentration of each species is dependent upon the plasma condition.<sup>22</sup> The above reaction kinetics are a function of electron temperature, which is determined by plasma parameters. The exact mechanism of the plasma-phase chemical reaction is very complex and is still not clear. The above example is a simplified reaction path model.

### 2.3. Plasma Enhanced Chemical Vapor Deposition

The mechanism of plasma deposition can be categorized into ionization of molecules, surface chemical reaction, and ion-assisted deposition.<sup>22</sup> In the surface chemical reaction mechanism, concrete reaction products are formed by the reaction of the reactant gas on the substrate material to facilitate the deposition of the film. The ion-assisted deposition mechanism can be related to a uniformity of solid film deposition.

Changing the electrode configuration in the plasma reactor can vary ion bombardment energy to the substrate since the potential drop near the electrode depends on the electrode area. For example, the potential drop at electrode 1,  $V_1$ , and at electrode 2,  $V_2$  can be related to the surface areas of electrode 1,  $A_1$ , and 2,  $A_2$ , as below:<sup>21,22</sup>

$$\left(\frac{V_1}{V_2}\right) = \left(\frac{A_2}{A_1}\right)^n \quad [8]$$

where  $n = 4$  for the ideal case. However, based on experimental results, typical values for  $n$  are between 1 and 2.<sup>22</sup> In any case, the larger potential drop appears at the smaller electrode.

#### 2.4. PECVD Thin Film

Silicon nitride film can be deposited by a low-pressure chemical vapor deposition (LPCVD) and plasma enhanced chemical vapor deposition (PECVD). Table II shows a comparison of silicon nitride's physical properties between two deposition methods. The PECVD silicon nitride ( $\text{SiN}_x$ ) is widely used in microelectronic devices because it is a good barrier of sodium and humidity. The process has been typically done using a conventional glass substrate at above  $250^\circ\text{C}$ . The PECVD  $\text{SiN}_x$  has a deposition temperature of  $275\text{-}325^\circ\text{C}$ , which is lower than that of the LPCVD  $\text{Si}_3\text{N}_4$  process of  $700\text{-}900^\circ\text{C}$ .<sup>22,24</sup> The high temperature ( $> 250^\circ\text{C}$ ) process is advantageous for two reasons: (i) the high temperature can cure many defects in the film because of the annealing mechanism, and (ii) for certain VLSI applications, a near stoichiometric nitride film with a low hydrogen content through the high temperature is required.<sup>25,26</sup> By methods other than the high temperature, many attempts have been done in PECVD  $\text{SiN}_x$  deposition to obtain low defects and low hydrogen contents. For example,  $\text{N}_2$  was adopted instead of  $\text{NH}_3$  as a nitrogen source.<sup>26-28</sup> Although the use of  $\text{N}_2$  rather than  $\text{NH}_3$  as the nitrogen source has decreased hydrogen content in the film, difficulty is still encountered with the strong N-N bond of a silicon-rich film because a nitrogen-rich silicon nitride is required for some applications.<sup>26</sup>

Table II. Material properties of SiN<sub>x</sub> film. (reference<sup>23</sup>)

Property	Deposition method	
	LPCVD	PECVD
Si/N ratio	0.75	0.8 – 1.0
Density (g/cm <sup>3</sup> )	2.8 – 3.1	2.5 – 2.8
Refractive Index	2.0 – 2.1	1.8 – 2.1
Dielectric constant	6 - 7	6 - 9
Dielectric strength (MV/cm)	10	6
Thermal expansion coefficient (°C <sup>-1</sup> )	$4 \times 10^{-6}$	$4 \sim 7 \times 10^{-6}$
Step coverage	Fair	Conformal
Stress at 23°C on silicon (dyn/cm <sup>2</sup> )	$1.2 \sim 1.8 \times 10^{10}$ (tensile)	$1.0 \sim 8.0 \times 10^9$ (tensile or compressive)



To break strong N-N bonds with plasma, higher power and higher temperatures are required. There have been several reports about PECVD SiN<sub>x</sub> at low temperatures, *e.g.*, below 150°C.<sup>25,26</sup> However, at a low temperature, *e.g.*, 100°C, PECVD SiN<sub>x</sub> was so unstable that it easily oxidized even at room temperature.<sup>25</sup> In order to improve the stability of the PECVD SiN<sub>x</sub> film, many modification methods have been used. For example, helium was introduced to the feed stream, or the high-density plasma source; *e.g.*, electron cyclotron resonance (ECR), was attached to the reactor.<sup>26</sup> However, these processes are not appropriate for large area substrates due to the low deposition rate or poor uniformity. Therefore, it is desirable to develop a proper PECVD SiN<sub>x</sub> process based on the conventional parallel-plate reactor.<sup>27,28</sup>

The chemical structures of SiN<sub>x</sub> films are often emphasized because they determine the performance of films in TFT applications. Atomic N and Si concentration ratios and N-H and Si-H bond ratios are frequently analyzed. The two chemical aspects of films can determine whether or not the SiN<sub>x</sub> film is stable and adoptable. From I-V characteristic testing of SiN<sub>x</sub>, the film can be proven applicable to a TFT device having a low leakage current at a high breakdown voltage.

PECVD is also used in depositing a-Si:H for the TFT application because of low temperature and large areas uniformity.<sup>28</sup> Conventionally, a-Si:H is deposited from SiH<sub>4</sub> with optional and additional gases such as H<sub>2</sub>, He, or Ar. The process parameters, such as temperature, power, and reactive gases, influence its bulk properties, such as hydrogen content, dangling bonds, photosensitivity, and mechanical strength. Table III shows basic physical properties of the a-Si:H.

---

 Table III. Physical properties of typical high quality a-Si:H. (reference<sup>16,18</sup>)

Property	a-Si:H
Activation energy of conduction at 300 K, $E_A$	0.7 – 0.8 eV
Dark conductivity, $\sigma_{\text{dark}}$	$10^{-9} - 10^{-8} \Omega^{-1}\text{M}^{-1}$
Defect density, $n_D$	$10^{22} \text{ m}^{-3}$
Electron mobility, $\mu_e$	1.0 $\text{cm}^2/\text{Vs}$
Hole mobility, $\mu_h$	0.02 $\text{cm}^2/\text{Vs}$
Hydrogen content	5 – 15 at. %
Optical gap, $E_{\text{Tauc}}$	1.75 – 1.85 eV
Photoconductivity, $\sigma_{\text{ph}}$	$10^{-3} - 10^{-2} \Omega^{-1}\text{M}^{-1}$
Photosensitivity	106
Refractive index, n	3.5 – 3.8
Urbach energy	50 –60 meV

---

Many a-Si:H properties are different from those of single-crystalline silicon in that the former is easier to oxidize at atmosphere than the latter. The effect of the a-Si:H deposition process on the TFT properties is often significant with respect to its power. Since the high power of the a-Si:H PECVD process damages the surface of the gate  $\text{SiN}_x$  by forming a rough interface and a fixed charge, a low power process is preferred.<sup>16,29</sup>

### 3. Thin Film Transistor

A thin film transistor (TFT) is a solid-state field-effect transistor (FET), which contains three electrodes, *i.e.*, source, drain, and gate. The differences in structures, materials, and fabrication processes make the device characteristics of a TFT very different from those of a MOS transistor. Most transistors, except the TFT, are operated based on single-crystal semiconductor material. However, TFTs have been successfully applied to the active matrix liquid crystal display (AMLCD) based on glass substrate.<sup>16</sup> The TFTs can have various types of structures based on the design of source, drain, and gate. Among the three basic types of TFT structures, *e.g.*, staggered, inverted staggered, and coplanar, the inverted staggered (bottom-gate) structure is the most popular one.<sup>16,18</sup>

To construct a channel region of TFT between the source and drain, amorphous silicon (a-Si:H) is widely used. One of the critical features of the a-Si:H TFT is its large on-off ratio, defined as the ratio of on-state to off-state channel conductance. Greater than six orders of magnitude in a-Si:H TFT have been required. Arrays of millions of TFTs could be fabricated on a large-area, low-temperature glass substrate. Therefore, the a-Si:H TFT is one of the most promising semiconductors satisfying the requirement of a

switching element. The a-Si:H TFT is the most popular active matrix addressing device for high quality large area LCDs.<sup>16-18</sup> In addition, a-Si:H TFTs have been applied to many new microelectronic, optoelectronic, and chemical products, such as 2D X-ray medical imagers, and radiation and chemical detectors. Recently, new applications such as thin-film retina, facsimile, digital copier image sensors, and bio-analytical sensors were introduced.<sup>17</sup> For the substrate of a-Si:H TFT, low sodium glass, *e.g.*, Corning 7059 glass, is widely used. Therefore, the development of the process at a low temperature is necessary. For the film deposition of TFT, PECVD is commonly used in depositing a-Si:H and SiN<sub>x</sub> due to a low temperature requirement.

PECVD is one of the non-equilibrium thermodynamic processes. In addition to conventional process parameters such as temperature, pressure, and feed gas, it has an extra control parameter, *i.e.*, the plasma power. Due to the complicated plasma reactions, many different types of SiN<sub>x</sub> and a-Si:H films can be deposited. SiN<sub>x</sub> films having the same refractive index (RI) can be prepared from totally different process conditions. The film can be characterized according to its chemical properties, such as Si/N ratio, and Si-H and N-H concentrations; or its physical and electrical characteristics, such as RI, dangling bond, and charge density. They all affect the transistor's threshold voltage, reliability, on-current ( $I_{on}$ ), and off-current ( $I_{off}$ ). In addition, its interfacial properties with the gate dielectric layer are critical to directly impact TFT characteristics.

Figure 6 shows a typical inverted staggered TFT with a tri-layer structure, *i.e.*, a top dielectric film protects the back channel region. In this structure, key films, such as gate dielectric, a-Si:H, channel passivation, and heavily phosphorus-doped n<sup>+</sup> a-Si:H

layers, can be deposited by the PECVD. Besides the low temperature, there are several more advantages in TFT fabrication with the PECVD: (i) clean film-film interfaces can be prepared with the one-pump-down process, and (ii) uniform thin films can be obtained over large area substrates.

The inverted staggered structure is more popular than the staggered structure.<sup>18</sup> Tri-layer structure has the top dielectric film, which functions as channel protection as well as an etch stop layer.<sup>16,18</sup> In addition, advantages of tri-layer over bi-layer include that tri-layer is less photosensitive.<sup>18</sup>

Typically, the field effect mobility of a-Si:H TFT is lower than or equal to  $1.0 \text{ cm}^2/\text{Vs}$ . The mobility affects the switching speed of the TFT. The most common method of increasing the mobility is by changing the morphology of silicon to microcrystalline or polycrystalline.<sup>16,18</sup> Microcrystalline silicon ( $\mu\text{c-Si}$ ) is composed of small silicon crystals, *i.e.*, in the range of less than 10 nm, embedded in a large amorphous silicon matrix. Polysilicon TFT usually has a high field effect mobility, which is up to  $200 \text{ cm}^2/\text{Vs}$ , and a large leakage current.<sup>25</sup> However, a high temperature, which is higher than  $600^\circ\text{C}$ , is required to directly deposit the polysilicon using a conventional CVD system. Many efforts of growing the polysilicon from the deposited amorphous silicon have been made, for example, laser crystallization, ion beam irradiation, rapid thermal annealing, etc.<sup>16,18</sup>

The interface between a-Si:H and  $\text{SiN}_x$  is critical to the performance of the a-Si:H TFT.<sup>16</sup> At the surface, if the content of hydrogen is low, there are more dangling bonds in the interface, which result in a high density.

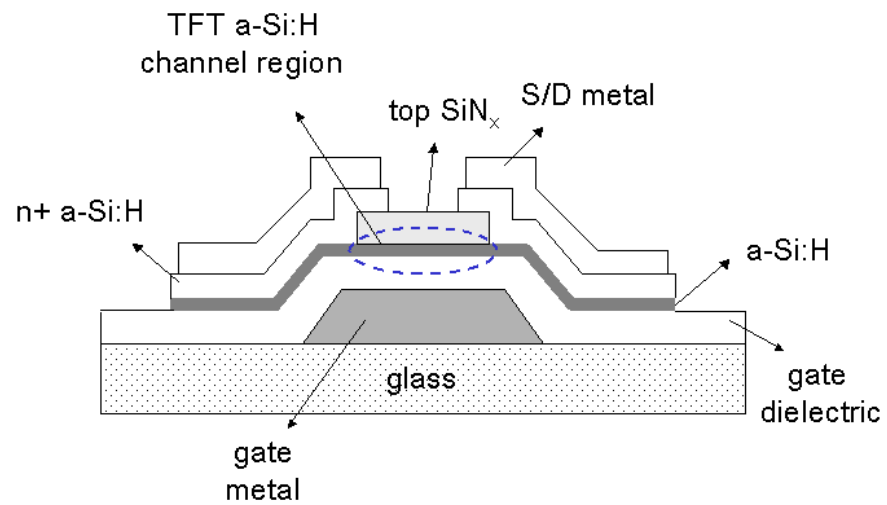


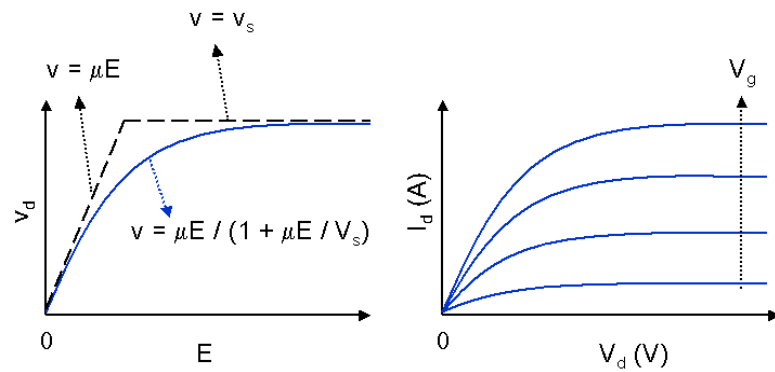
Figure 6. Cross-sectional view of an inverted staggered tri-layer a-Si:H TFT.  
(reference<sup>16</sup>)

The high defect eventually corresponds to low field effect mobility, high threshold voltage, large subthreshold slope, and high leakage current.<sup>17,18</sup> To enhance the content of hydrogen at the surface, an additional H<sub>2</sub> plasma can be used.<sup>29</sup> Hydrogen is a crucial element in TFTs. It exists in bulk film and at the interface of films. The main function of hydrogen is to passivate dangling bonds of Si and N that are a source of charge traps.

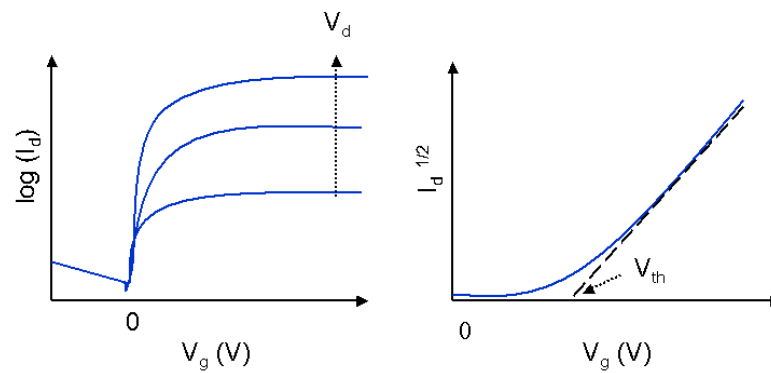
Figure 7 shows (a) typical output characteristic curves based on the linear approximation of the velocity-field, and (b) typical transfer characteristic curves of field effect transistor (FET).<sup>30</sup> Since the a-Si:H TFT is a field effect transistor (FET), the electrical properties have shown similar results to the typical FET.<sup>18,30</sup> Typically, I-V characteristics, depending upon the gate voltage and the source-drain voltage, commonly explain the performance of a FET or TFT.<sup>16,17</sup> For the output characteristics, the drain currents at the saturated velocity case are almost equally spaced, with increasing gate voltage. A simple stepwise-linear approximation to the velocity-field curves assumes constant mobility dependence up to some critical field,  $E_C$ , and constant saturation velocity,  $v_s$ , for a higher field. The relation can be expressed as below:

$$v_d = \frac{\mu E}{1 + \mu E / v_s} \quad [9]$$

where  $v_d$  is the drift velocity of the carrier,  $\mu$  is the low-field mobility, and  $E$  is the electric field.<sup>30</sup> The output characteristics of TFTs plot the drain current as a function of the drain voltage or bias with gate voltage as a parameter. On the other hand, the transfer characteristics plot the output drain current as a function of the input gate voltage for a fixed drain voltage.<sup>30</sup>



(a)



(b)

Figure 7. (a) Typical output characteristics curves based on the linear approximation of the velocity-field, and (b) typical transfer characteristic curves of field effect transistor (FET). (reference<sup>30</sup>)



The drain current,  $I_d$ , can be expressed as equation [10] at the saturation condition.

$$I_d = \frac{1}{2} \mu_{eff} \left( \frac{W}{L} \right) C (V_g - V_{th})^2 \quad [10]$$

where  $\mu_{eff}$  is the effective mobility of the a-Si:H channel,  $C$  is the capacitance of the gate dielectric,  $W$  is the width of the TFT channel, and  $L$  is the length of the TFT channel. Electrical properties, which critically represent the TFT performance, *i.e.*, the threshold voltage ( $V_{th}$ ) and the field effect mobility ( $\mu_{eff}$ ), were calculated from replotting the  $\sqrt{I_{ds}}$  vs.  $V_g$  ( $V_g = V_d$ ) curve based on the equation [10].

## CHAPTER III

### EXPERIMENTAL METHODS

#### 1. Thin Film Deposition Process

Silicon nitride ( $\text{SiN}_x$ ) and amorphous silicon (a-Si:H) films were deposited by plasma enhanced chemical vapor deposition (PECVD, Applied Materials, model AMP 3300 I, Santa Clara, CA). The film was deposited using the  $\text{SiH}_4/\text{NH}_3/\text{N}_2$  gas mixture at various powers, with a fixed pressure of 500 mTorr and a constant substrate temperature of 250°C. The PECVD system used in this study has a parallel-plate electrode configuration. The distance between the two electrodes is 6.25 cm, and the electrode radius is 32.5 cm wide. Figure 8 shows a schematic diagram of the PECVD reactor. The cathode is driven by a 50 kHz rf power supply (3200 AMT, ENI, Rochester, NY). The anode has a donut shape with the feed gas being introduced from the center and exhausted from the edge. For the hydrogenation process, the device was exposed to  $\text{H}_2$  plasma with  $\text{H}_2$  400 sccm at 850 mTorr, 300 W, and room temperature in the PECVD. The plasma-phase chemistry of the PECVD was monitored with an optical emission spectroscopy (OES, SC Technology, Fremont, CA).

The silicon oxide ( $\text{SiO}_x$ ) film for the silicon microchannel device was deposited by a magnetron sputtering system at 80 W, 3.3 mTorr using a 13.56 MHz rf generator with a  $\text{SiO}_2$  target (Angstrom Science, Duquesne, PA). The Cr (1000 Å) film for the microchannel device was also deposited by the sputtering at 100 W with a Cr target (Kurt J. Lesker, Clairton, PA).

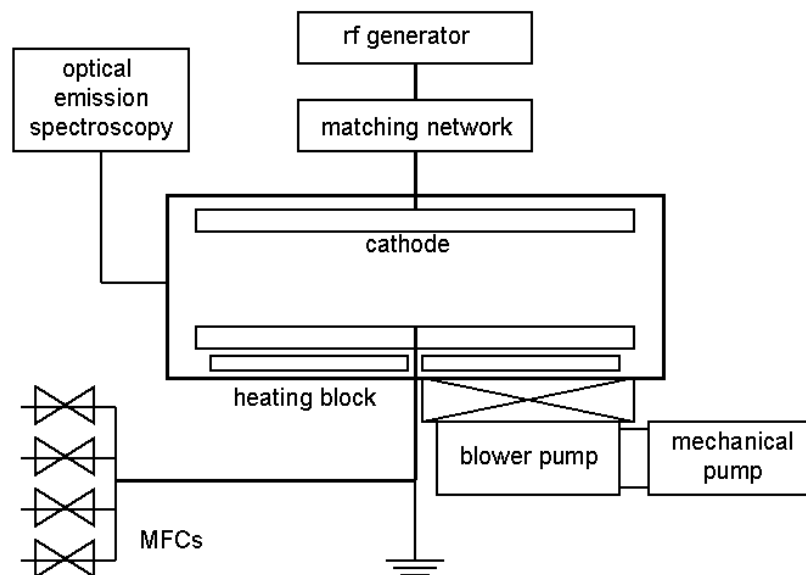


Figure 8. Schematic diagram of plasma enhanced chemical vapor deposition (PECVD) reactor.

## 2. Reactive Ion Etching

The reactive ion etching (RIE) process was done with a commercial reactor (model 700D, Plasma-Therm, St. Petersburg, FL), which has a conventional diode-type electrode configuration with the bottom electrode driven by a 13.56 MHz rf generator. The anode and cathode electrodes are the same size, with a diameter of 22.86 cm. The space between the two electrodes is 7.3 cm, and both electrodes have an anionized aluminum surface. For a  $n^+$  a-Si:H etching, a gas mixture of  $\text{Cl}_2/\text{CF}_4$  (8/2 sccm) at 100 mTorr, 300 W, and room temperature was used. For SU-8 surface modification or microchannel device modification, different  $\text{O}_2$  flow rate, pressure, and rf power were used depending upon the purpose of the modification.

## 3. Solid State Surface Analysis

Figure 9 shows a schematic diagram of the ellipsometer (model i1000, Rudolph Technology, Flanders, NJ). By a rotating polarizer, the laser light (6328 Å) is polarized into two waves: p(parallel)-wave and s(senkrecht)-wave. Here, a phase shift induced by the reflection,  $\Delta$ , is defined below:

$$\Delta = \delta_1 - \delta_2 \quad [11]$$

where  $\delta_1$  is a phase difference between the p-wave and s-wave before the reflection, and  $\delta_2$  is a phase difference between the p-wave and s-wave after the reflection. From the photosensitive detector of an ellipsometer, the reflection coefficient can be obtained and correlated with a variable,  $\psi$ , as shown below:

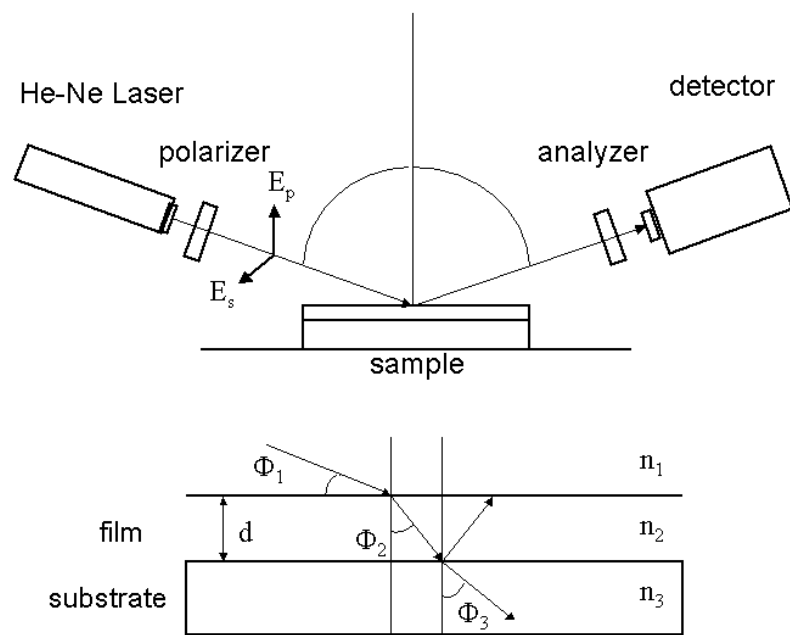


Figure 9. Schematic diagram of an ellipsometer and light reflection. (reference<sup>31</sup>)

$$\tan\psi = \frac{|R^p|}{|R^s|} \quad [12]$$

where  $R^p$  is a reflection coefficient of the p-wave, or the ratio of the outgoing p-wave amplitude to the incoming p-wave.<sup>31</sup>  $R^s$  is a reflection coefficient of the s-wave, or the ratio of the outgoing s-wave amplitude to the incoming s-wave. The relationship among  $\Delta$ ,  $\psi$ ,  $R^p$ , and  $R^s$  are related as shown below:

$$\rho = \frac{R^p}{R^s} = \tan\psi e^{i\Delta} \quad [13]$$

where  $\rho$  is the total reflection coefficient of the sample. The signal is minimized when the polarized p-wave and s-wave in the analyzer are in-phase. For a single layer film,  $R^p$  and  $R^s$  can be expressed by equations [14] and [15], respectively, with respect to a variable,  $\beta$ , which is the phase change that the wave experiences as it transverses the film between interfaces.<sup>31</sup>

$$R^p = \frac{r_{12}^p + r_{23}^p \exp(-i2\beta)}{1 + r_{12}^p r_{23}^p \exp(-i2\beta)} \quad [14]$$

$$R^s = \frac{r_{12}^s + r_{23}^s \exp(-i2\beta)}{1 + r_{12}^s r_{23}^s \exp(-i2\beta)} \quad [15]$$

The refractive indices  $n_2$  and incident angle  $\Phi$  in different media can be correlated by the relationship among  $\beta$  and film thickness,  $d$ , and film refractive index,  $n_2$ , can be obtained as below:

$$n_1 \sin \Phi_1 = n_2 \sin \Phi_2 = n_3 \sin \Phi_3 \quad [16]$$

$$\beta = \frac{4\pi n_2 d \cos \Phi_2}{\lambda} \quad [17]$$

From the relationships between the parameters from equation [11] to equation [17], the film's thickness,  $d$ , and the refractive index,  $n_2$ , can be calculated using equations [11] to [17] with numerical methods.<sup>31</sup> The calculated film thickness was confirmed with the measurement using a surface profilometer (Dektak3, Veeco Co., Woodbury, NY).

The Electron Spectroscopy for Chemical Analysis (ESCA, Axis Ultra, Kratos Analytical Inc. Chestnut Ridge, NY), where is in the Center for Integrated Microchemical System of the Chemistry Department at Texas A&M University, was used to characterize PECVD films, proteins, and DNA molecules. It used a monochromatic Al K $\alpha$  (1486.6 eV) X-ray source. Except for hydrogen and helium, all other elements in the periodic table can be analyzed by ESCA. Figure 10 shows the mechanism of the surface photoemission caused by X-ray irradiation.<sup>32,33</sup> When the surface is irradiated with photons with energy less than 50 eV, electrons are ejected from the valence band, which are ultraviolet photoelectron emissions. On the other hand, if the photo energy is high, such as X-rays, electrons in the deep core shell level of the atom can be ejected, which is known as X-ray photoemission spectroscopy (XPS).<sup>33</sup> Electrons can be emitted from all the levels as long as the photon energy is larger than the electron binding energy. It is the binding energy that constructs the chemical structure of the surface. An X-ray with 1-2 keV, *e.g.*, monochromatic Al L (1486.6 eV), is suitable for this purpose. The measured energy of the ejected electrons  $E_k$  is related to the binding energy  $E_b$  by equation [18]

$$E_k = h\nu - E_b - \Phi_a \quad [18]$$

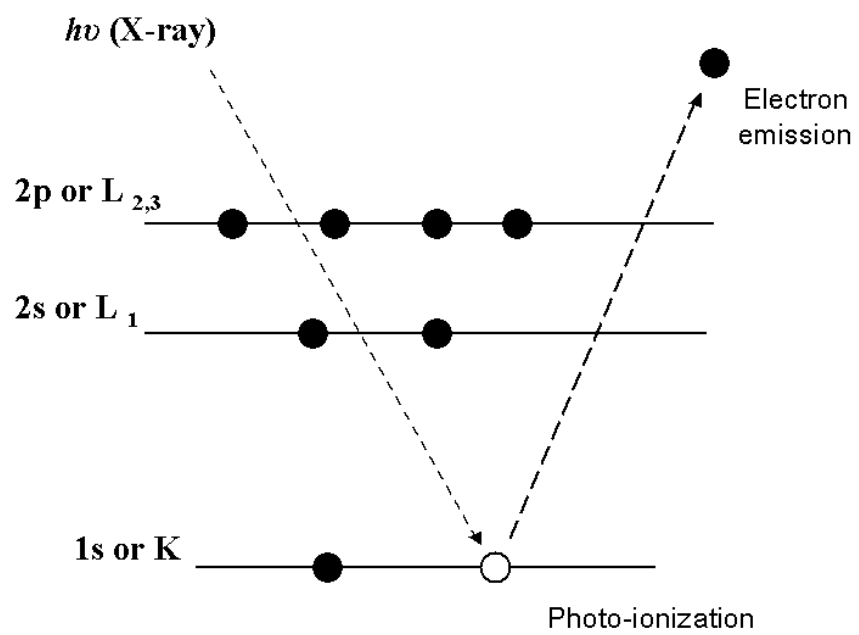


Figure 10. Schematic diagram of surface caused by X-ray photoemission. (reference<sup>32</sup>)



where  $h\nu$  is the incident X-ray energy and  $\Phi_a$  is the work function of the spectrometer (3-4 eV). By investigating the binding energy shift due to the change of chemical structure, the oxidation state of the atom can be identified. In addition, by integrating the area under the spectrum, a quantitative analysis of the chemical composition structures can be obtained.<sup>32</sup> With their sensitivity factors in survey mode, the atomic concentration of a specific element in the reaction product was calculated from the area of a major peak.  $C_{1s}$  emission at 284.6 eV was used as a reference to correct the charging effect of the surface.

The film's bond structure was analyzed with Fourier transformed infrared (FT-IR) spectroscopy (FTS 40, Bio-rad DigiLab, Cambridge, MA). Figure 11 shows the operational principle of FT-IR with a classical Michelson interferometer.<sup>34</sup> As shown in Fig. 11, the laser is a monochromatic radiation source having a wavenumber ( $\nu$ ). Since the moving mirror changes the optical path, a cosine signal can be obtained at the detector as a function of the wavenumber ( $\text{cm}^{-1}$ ),  $\nu$ , and the path difference,  $x$ , which is called retardation. The intensity  $I(x)$  can be converted into the spectrum as below:<sup>34</sup>

$$I(x) = I_o [1 + \cos(2\pi\nu x)] \quad [19]$$

Depending upon the change of retardation ( $x$ ) value, a broad range of spectra can be expressed as below:<sup>34</sup>

$$\nu_{\max} - \nu_{\min} = \frac{1}{2\Delta x} \quad [20]$$

where  $\nu_{\max}$  is a maximum wavenumber;  $\nu_{\min}$  is a minimum wavenumber, which can be sensed by the detector of FT-IR; and  $\Delta x$  is the distance between two retardation points.

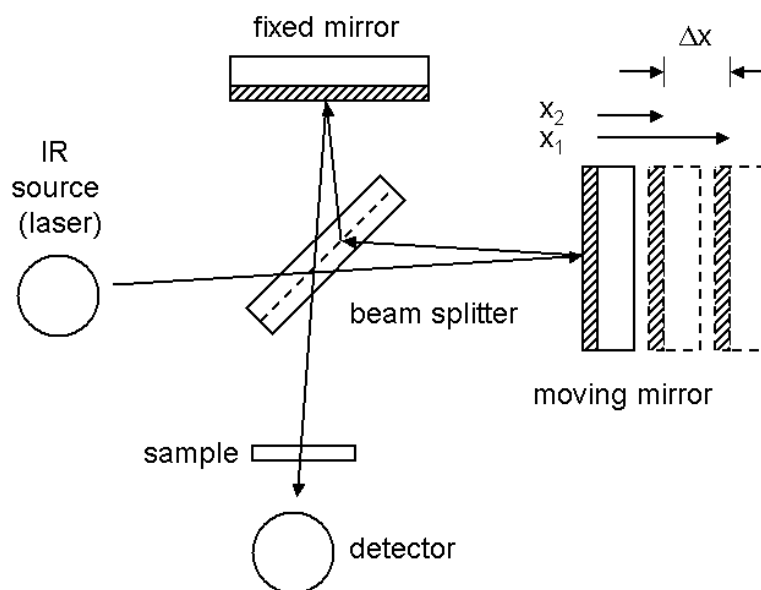


Figure 11. Schematic diagram of the operational principle of Fourier transformed infrared (FT-IR) spectroscopy. (reference<sup>34</sup>)

The scanning electron microscope (SEM) is a common technique used to examine the surface or the cross-section of a small geometry pattern. SEM utilizes an electron beam to create a magnified image of the sample.<sup>33</sup> The SEM unit consists of three parts: (i) an electron gun that produces the electron beam, (ii) magnetic coil lenses that focus the beam onto the sample, and (iii) the Evehart-Thornely (ET) detector, which detects secondary electrons of backscattered electrons emitted from the sample surface. The image is obtained by scanning a focused electron beam over the sample and detecting the secondary electrons emitted, or backscattered electrons. Practically, it is important to reduce the surface charging effect when electrons land on the surface. Surface charging can be reduced with a thin surface conductive layer coating, such as gold (Au) or gold-palladium (AuPd), because Au and AuPd provide an oxide-free surface.<sup>33</sup>

#### 4. Anisotropic Etching of Silicon Wafer

Figure 12 shows a schematic diagram of the experimental setup of potassium hydroxide (KOH) anisotropic etching of a silicon wafer. A p-type (100) silicon (10-80  $\Omega$ -cm) wafer (MEMC Electronic Materials, St. Peters, MO) was used as the Si substrate. Silicon nitride ( $\text{SiN}_x$ ) was deposited on a Si substrate by PECVD at 700 W,  $\text{SiH}_4/\text{NH}_3/\text{N}_2$  40/120/700 sccm, 500 mTorr and 250°C. The substrate was patterned with a mask using the AZ 1512 positive photoresist (PR) by a spin-coater (KW4A, Chemat Co., Northridge, CA), and the  $\text{SiN}_x$  layer was etched with a buffered oxide etchant (BOE, 10% HF and 40%  $\text{NH}_3\text{F}$ ).

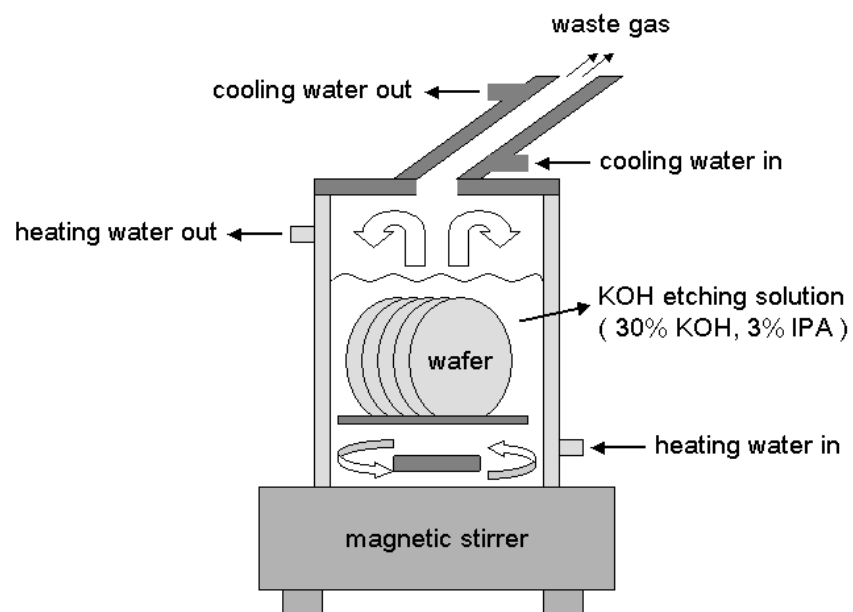


Figure 12. Schematic diagram of an experimental setup of potassium hydroxide (KOH) anisotropic Si etching.

The Si wafer was then etched with a KOH/isopropyl alcohol (IPA) mixture, *i.e.*, 300 g KOH plus 30 ml IPA diluted to 1000 ml with deionized water (DI water). This method was used to prepare the channel region and the two reservoirs of a microchannel device. In order to protect the backside of the silicon wafer from KOH etching, a SiN<sub>x</sub> layer was deposited there. To keep this layer during BOE etching, the PR was also coated on the backside of the wafer. The frontside PR was exposed to the UV light of the aligner, developed with an AZ300 MIF developer for two minutes, and hard-baked at 130°C for one minute using a hot plate. Before KOH etching, the PR was completely removed by acetone and cleaned with DI water. After KOH etching, the mask nitride, which prevents the front side, was removed by diluted HF (1:10 HF/H<sub>2</sub>O).

## 5. Biomolecule Sample Preparation and Assay

Three proteins, *i.e.*, ovalbumin (45 kDa), carbonic anhydrase (29 kDa) and  $\alpha$ -lactalbumin (14.2 kDa), were purchased as lyophilized powders (Sigma Chemicals, St. Louis, MO). The protein was dissolved in a 0.5× TBE solution (0.045 M tris-borate, and 0.001 M EDTA, at pH 8.2) containing 0.2% SDS. Before electrophoresis, the solution was heated to 98°C for three minutes to denature the protein. The total protein concentrations were 650, 1300, and 1950  $\mu\text{g/ml}$  for the one-, two-, and three-protein solutions separately. A buffered 0.5× TBE solution (20  $\mu\text{l}$ ) was loaded into both the feed and the detection reservoirs. Protein solution (2-4  $\mu\text{l}$ ) was added into the feed reservoir before the electrophoresis. In order to confirm the existence of proteins on the detection electrodes, the electrode surface was stained and destained. By dissolving 1.0 g of

Coomassie Brilliant Blue R250 in 360 ml of methanol/DDW (1:1) and 40 ml of acetic acid, a staining solution was prepared. The microchip was immersed in the staining solution more than five times and placed on a slowly rotating platform for one hour at room temperature to confirm a complete staining. The microchip was destained by soaking it for two hours in the methanol/acetic acid solution without dye on a slowly rotating platform to confirm enough destaining, changing the destaining solution three or four times. The more thoroughly the gel was destained, the smaller the amount of stained protein could be identified. A DNA sample,  $\lambda$ -EcoR I digested, was purchased from Sigma Chemicals Co. The  $\lambda$ -EcoR I digested DNA had six different-sized fragments. The DNA was dissolved in a TBE buffer at a concentration of 300  $\mu\text{g}/\text{ml}$ . The  $\lambda$ -EcoR I digested DNA sample had six different sizes (3.5, 4.9, 5.6, 5.8, 7.4, and 21.2 kbp) of fragments. The DNA sample, which was loaded on the surface of the channel, could be stained with 0.7  $\mu\text{g}/\text{ml}$  ethidium bromide. The DNA fluorescent spot could be observed under a 254 nm wavelength UV exposure (365  $\text{mW}/\text{cm}^2$ ).

## 6. Fabrication of Microchannel for Protein Analysis

Figure 13 shows (a) a flow diagram of the procedure for the fabrication of a microchannel on a Si wafer for protein electrophoresis tests, and (b) the photograph of a completed device. After the Si was anisotropically etched with the KOH solution, the mask  $\text{SiN}_x$  layer was removed by BOE. A layer of  $\text{SiO}_x$  (400 Å) was deposited by rf sputtering on the substrate surface. Chromium (Cr) was subsequently deposited in the same chamber.

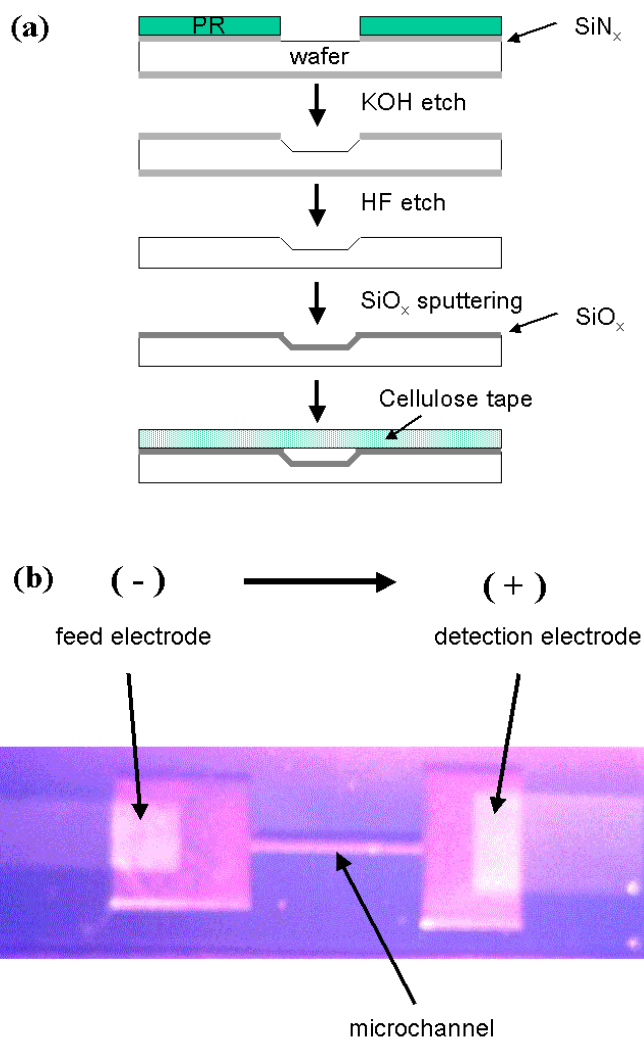


Figure 13. (a) Flow chart diagram of a Si microchannel device fabrication process, and (b) photograph of a completed Si microchannel electrophoresis device.

The Cr film is known to be chemically resistant to the attack of the protein solution. The feed and detection electrodes were patterned with the second mask, and the exposed Cr film was etched with a solution (HCl/H<sub>2</sub>O 3:1 volume). Four different sizes of detection electrodes, *i.e.*, 1.125 mm<sup>2</sup>, 2.1 mm<sup>2</sup>, 3.375 mm<sup>2</sup>, and 4.5 mm<sup>2</sup>, were prepared using different photomasks. In order to remove any possible contaminants left on the device, the patterned substrate was thoroughly cleaned with a HCl solution (5 ml of 37% HCl diluted with 95 ml of DI), 0.1 M KOH solution, DI water, and acetone for two or three times. A cellulose tape was attached above the channel region to form the enclosed microchannel structure.

#### 7. Affinity Experiment of Protein and DNA on Substrates

In order to examine the adsorption of protein and DNA, bare silicon, SiN<sub>x</sub>, SiO<sub>2</sub>, plain slide glass, SU-8, O<sub>2</sub> plasma-treated substrates, H<sub>2</sub> plasma-treated substrates, Cr, cellulose tape, and solution-oxidized substrates were prepared and examined. The bare silicon was prepared by removing the native oxide by BOE. The microscope slide glass (12-550A, Fisher Scientific, Pittsburgh, PA) was used as the glass substrate. The SiN<sub>x</sub> was deposited on the top of the glass by PECVD. It had a thickness of 3200 Å and refractive index of 1.912 measured from an ellipsometer. The SiO<sub>2</sub> film (1400 Å) was prepared by the sputtering method.

The negative photoresist (SU-8, Microchem Co. Newton, MA) was coated at 1000 rpm and followed by baking at 100°C. An adhesion promoter, 10.0% dimethyldisilazane (HMDS, Arch Chemicals, Norwalk, CT) in 1-methoxy-2-propanol



acetate was spin-coated before the SU-8 coating. To solidify the SU-8 without defining any pattern, the exposure of UV light with an intensity of  $365 \text{ mW/cm}^2$  for cross-linking followed. The  $1600 \text{ \AA}$  Cr film was also deposited by sputtering at 100 W with a 2-inch Cr target. The cellulose tape was obtained from 3M, Minneapolis, MN.

For the simple protein adsorption experiment,  $4.0 \text{ }\mu\text{l}$  of protein solution which contains  $2000 \text{ }\mu\text{g/ml}$  of proteins composed of ovalbumin, carbonic anhydrase, and  $\alpha$ -lactalbumin in a  $0.5\times$  TBE buffer, was added to the substrate surface by micropipette and incubated at room temperature for one hour. After incubation, the droplets were washed twice by  $10.0 \text{ }\mu\text{l}$  of buffer solution and washed once by  $10.0 \text{ }\mu\text{l}$  of DI water with a micropipette. The remaining liquid was removed with a nitrogen gun. The surface of the SU-8 polymer was examined with ESCA to detect the protein residue. The ESCA  $\text{N}_{1s}$  and  $\text{S}_{2p}$  peaks were used to identify the proteins. For the DNA affinity experiment,  $0.7 \text{ }\mu\text{l}$  of DI water, buffer solution, or DNA solution was dropped on the surface of the samples. The droplets were pictured and their contact angles were measured. For the contact angle measurements, a microscopic CCD camera system (QX3 player, Intel, Santa Clara, CA) was constructed.

To prepare oxidized surfaces of Si, PECVD  $\text{SiN}_x$ , glass, SU-8, and Cr surface, solution oxidation by  $\text{H}_2\text{O}/\text{H}_2\text{O}_2/\text{H}_2\text{SO}_4$  (1:1:3 v/v/v) was used for 40 min at  $90^\circ\text{C}$ . To prepare hydrogen plasma-treated Si, glass, and SU-8, the hydrogenation process was done by PECVD with  $\text{H}_2$  400 sccm at 850 mTorr, 300 W, and room temperature. The  $\text{O}_2$  plasma-treated SU-8 was prepared by RIE with  $\text{O}_2$  5 sccm at 100 mTorr, 100 W, and room temperature.

## 8. Surface Modification of Microchannel

The surface of the microchannel was exposed to an oxygen ( $O_2$ ) plasma, hydrogen ( $H_2$ ) plasma, and oxidation solution. For the plasma oxidation process, the RIE reactor was used with  $O_2$  15 sccm at 200 W, 200 mTorr, and room temperature. For the plasma hydrogenation process, the PECVD reactor was used with  $H_2$  400 sccm at 300 W, 850 mTorr, and room temperature. The solution oxidation was done in a solution of  $H_2O_2/H_2O/H_2SO_4$  (1:1:3 v/v/v) for 40 min at  $90^\circ C$ .

## 9. Microchannel Electrophoresis Preparation for Protein Analysis

A small amount of polyacrylamide gel solution was injected into the channel with a micropipette. The solution was polymerized at room temperature within five minutes without UV exposure. The gel solution was composed of 15.0% acrylamide/bisacrylamide (29:1), 0.75% ammonium persulfate, 0.2% SDS and 0.3% tetramethylethylenediamine (TEMED) in  $0.5\times$  TBE solution. The gel solution contained higher concentrations of initiator (ammonium sulfate) and catalyst (TEMED) than those used in a conventional electrophoresis gel.<sup>10,11</sup>

The acrylamid, a 40.0% acrylamide (Acrylamide/Bis-acrylamide (29:1)) solution, was purchased from Sigma Chemicals Co. The electrophoresis was carried out by applying 10 V DC to the detection electrode using a function generator (FG-7200C, EZ digital Co. Ltd., Korea). The current was measured with a digital multimeter (DMM196, Keithley Instruments Inc., Cleveland, OH). The current vs. time (I-t) curve was recorded via a GPIB interface card (PCI-GPIB, National Instruments, Austin, TX)

installed on a personal computer. The Savitsky-Golay method, with an order of 3 and 15 data, was used to smooth the  $dI/dt-t$  curve.<sup>35</sup> In order to calculate the smoothed  $dI/dt$  with an order of 3 (degree,  $n$ ) and 9 or 15 ( $2m+1$ ,  $m = 7$ ) data, a set of 9 or 15 consecutive values were calculated with the coefficient  $b_k$  ( $k=0,1,2,3$ ), which satisfies the relationship as shown below:

$$\frac{\partial}{\partial b_k} \left( \sum_{i=-m}^{i=m} (f_i - Y_i)^2 \right) = 0 \quad [21]$$

where  $Y_i$  is the measured data and  $f_i$  is expressed as below:

$$f_i = \sum_{k=0}^{k=n} b_k i^k \quad [22]$$

where  $i$  is an integer variable between  $-m$  and  $m$ . The resulting smooth derivative values can be numerically calculated as below:

$$Y_j^* = \frac{\sum_{i=-m}^{i=m} b_k Y_i}{N} \quad [23]$$

where  $Y_j$  is the smooth derivative value for plotting and  $N$  is a norm, which is a sum of  $b_k$ . Table IV shows a table for the numerical calculation of the Savitsky-Golay method for order 3 and the first derivative data.<sup>35</sup>

## 10. Microchannel Surface Electrophoresis Preparation for DNA Analysis

Figure 14 shows (a) the procedure of fabrication of the microchannel surface electrophoresis device, and (b) the photograph of a completed device. First, a layer of Cr is deposited on a glass or a Si substrate by rf sputtering. For the Si substrate, a PECVD  $\text{SiN}_x$  is deposited before Cr sputtering to avoid any current leakage through the substrate.

Table IV. Numerical table for modified least square method (Savitsky-Golay) with order 3. (reference<sup>35</sup>)

Data point	5 (m = 2)	7 (m = 3)	9 (m = 4)	11 (m = 5)	13 (m = 6)	15 (m = 7)
Y-7						12922
Y-6					1133	-4121
Y-5				300	-660	-14150
Y-4			86	-294	-1578	-18334
Y-3		22	-142	-532	-1796	-17842
Y-2	1	-67	-193	-503	-1489	-13843
Y-1	-8	-58	-126	-296	-832	-7506
Y0	0	0	0	0	0	0
Y+1	8	58	126	296	832	7506
Y+2	-1	67	193	503	1489	13843
Y+3		-22	142	532	1796	17842
Y+4			-86	294	1578	18334
Y+5				-300	660	-14150
Y+6					-1133	4121
Y+7						-12922
Norm	12	252	1188	5148	24024	334152

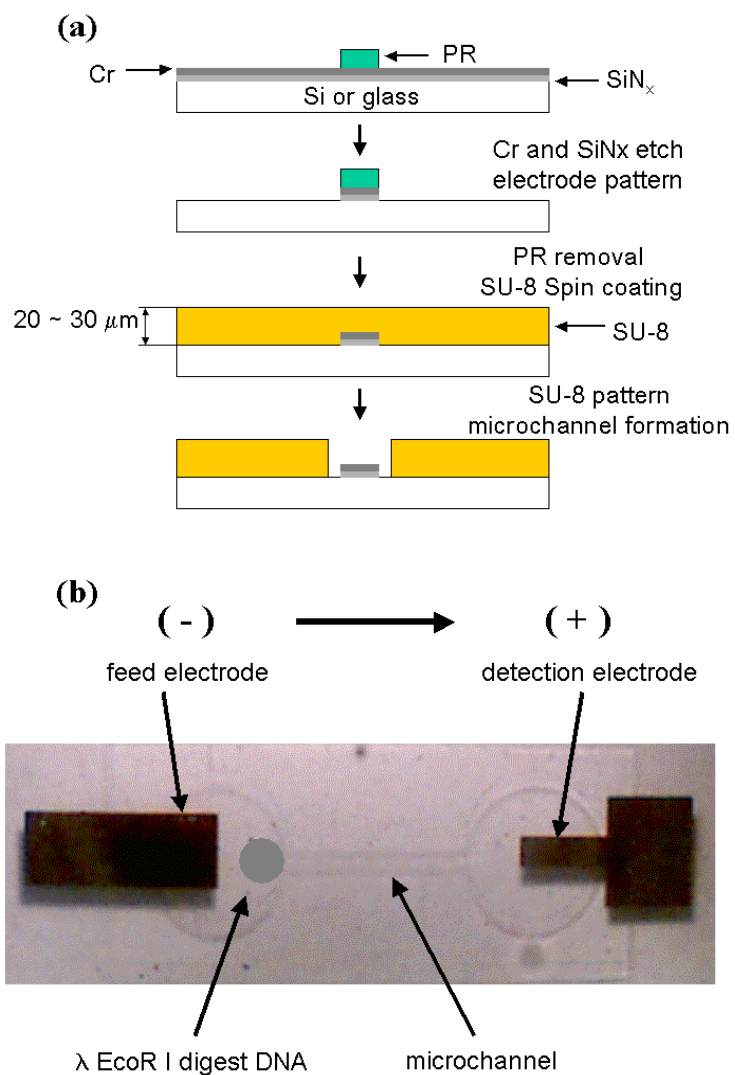


Figure 14. (a) Flow chart diagram of the SU-8 microchannel device fabrication, and (b) photograph of the completed SU-8 microchannel on glass.

The feed and detection electrodes are patterned with the first photomask process, and the Cr is etched with a solution of HCl/H<sub>2</sub>O (3:1 vol/vol). The area size of the detection electrode is 1.125 mm<sup>2</sup>, and that of the feed electrode is 2.1 mm<sup>2</sup>. In order to construct the three-dimensional channel structures, a special negative photoresist, SU-8, is used. It is exposed to a UV light through the second mask. The channel is 485 μm wide, 35 μm deep, and 0.5 cm long. The surface of the completely fabricated device was treated with an oxidation by the solution described before.

The 0.2 μl DNA sample (λ-EcoR I digest with six different sized fragments) was loaded at the entrance of the channel region. Totally, 1.4 μl of DNA sample was loaded, *i.e.*, by repeatedly dropping 0.2 μl of solution on the surface and waiting for at least ten minutes for air-drying the solution. In order to check the ionic strength effect of the solution, the buffer concentration was varied between 0.01× and 5.0× TBE. A relatively high concentration of the buffer was required to obtain a current high enough to migrate the DNA fragments on the bottom channel surface. In this experiment, 0.5× TBE was used unless specified otherwise. An electric field of 11.4 V/cm was applied through the channel region. To find characteristics of DNA adsorption, the N<sub>1s</sub> peak and P<sub>2p</sub> peak were intensively identified. The current reading from electrophoresis was monitored by LabVIEW 6i, and the time derivatives of the current were obtained by the Savitsky-Golay method.<sup>35</sup>

## 11. TFT Fabrication

Three lithographic masks were designed to fabricate the TFT and the microchannel. The integrated circuit (IC) mask design tool, L-Edit Pro (Ver 9.2, Tanner EDA Inc., Pasadena, CA), was used for the layout. The TFT channel length (L) was designed for 33, 34, 35, 40, 45, or 50  $\mu\text{m}$ . The channel width (W) was 30, 90, 180, or 300  $\mu\text{m}$ . The microchannel length was fixed at 0.5 cm, and the channel width was 500  $\mu\text{m}$ . The detection electrode was connected to the TFT electrode. The TFT has an inverted staggered tri-layer structure, which was fabricated on Corning 7059 glass. Two photomasks and self-aligned back exposure steps were used to construct the TFT.

Figure 15 shows a flow chart of the TFT fabrication process. The gate metal was composed of 1200  $\text{\AA}$  molybdenum. The tri-layer was composed of a gate dielectric  $\text{SiN}_x$  (3000  $\text{\AA}$ ), a-Si:H (500  $\text{\AA}$ ), and top  $\text{SiN}_x$  (2500  $\text{\AA}$ ), which was deposited in a PECVD system without breaking the vacuum. The source/drain layer was composed of 500  $\text{\AA}$  heavily phosphorus-doped PECVD a-Si:H, *i.e.*,  $\text{n}^+$ , and 1500  $\text{\AA}$  Cr. The a-Si:H active island and the  $\text{n}^+$  source/drain area were reactive ion etched using  $\text{Cl}_2/\text{CF}_4$  at 100 mTorr, 300 W. Other etching steps were carried out using wet processes.

After the  $\text{n}^+$  etch step, the photoresist was stripped and transistors were annealed in air for one hour at 230°C to remove plasma damage.<sup>28</sup> All PECVD films were deposited at 250°C. Gate  $\text{SiN}_x$  films were deposited with various gas flow rate of  $\text{SiH}_4/\text{NH}_3/\text{N}_2$  at a fixed pressure of 500 mTorr. The flow rate of each gas and power were varied in different experiments.

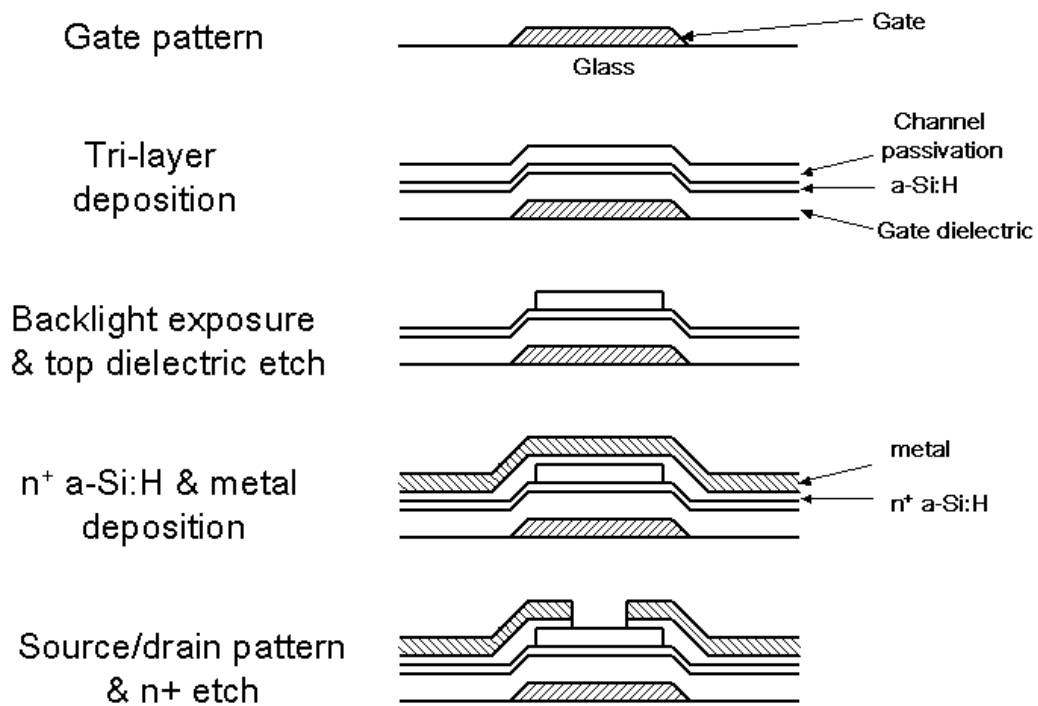


Figure 15. Flow chart diagram for the fabrication of an inverted staggered tri-layer a-Si:H TFT. (reference<sup>16</sup>)



Detailed relations between process parameters, such as power and gas composition, and material characteristics, such as the deposition rate, the refractive index, the stress, and the N-H/Si-H ratio, as well as the role of hydrogen plasma, were studied. The deposition rate increased and the refractive index decreased with the increase of power. The a-Si:H layer was deposited from SiH<sub>4</sub> 50 sccm at 250 mTorr and 250 W. In this study, the tri-layer was deposited at 250°C without breaking the vacuum, and the SiN<sub>x</sub> films were deposited at 500 mTorr, 700 W and a-Si:H at 250 mTorr, 250 W, unless specified otherwise.

## 12. Electrical Characterization of a-Si:H TFT

The electrical properties of the SiN<sub>x</sub> with I-V characteristics were obtained with a MIS (Metal Insulator Silicon) structure with an aluminum electrode. The LabVIEW 6i program-interfaced Agilent 4140B pA meter was used for the I-V measurement. For a-Si:H TFT, the output and transfer characteristics were measured by an Agilent 4155C.

Figure 16 shows a brief diagram of the electrical characterization setup for MIS or TFT. To ensure a complete dark environment for measurement, a light-proof black box was used to contain the MIS and TFT sample. The electrical characterization of the microchannel device connected to the a-Si:H TFT was also performed in the setup. The field effect mobility  $\mu_{\text{eff}}$  and the threshold voltage  $V_{\text{th}}$  were calculated from the saturation range of the transfer characteristics. The on-current  $I_{\text{on}}$  was the drain current measured  $I_{\text{d}}$  at  $V_{\text{g}} = 20$  V and  $V_{\text{d}} = 10$  V. The off-current  $I_{\text{off}}$  was the minimum drain current at  $V_{\text{d}} = 10$  V and  $V_{\text{g}}$  between  $-5$  and  $0$  V.

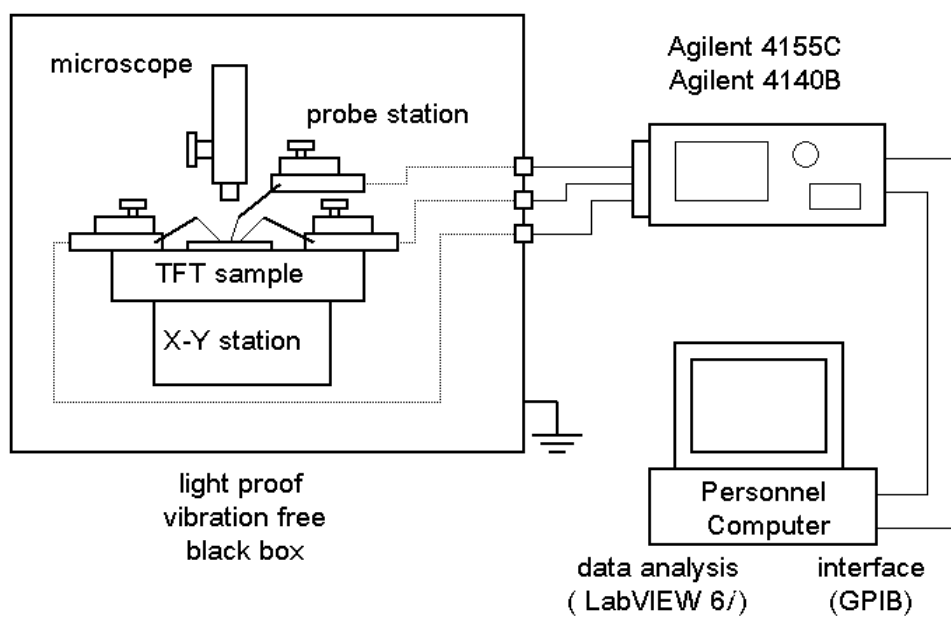


Figure 16. Electrical characterization setup of a-Si:H TFT and microchannel device connected to a-Si:H TFT.

The threshold voltage,  $V_{th}$ , and the field effect mobility,  $\mu_{eff}$ , were calculated from the  $\sqrt{I_{ds}}$  vs.  $V_g$  ( $V_g = V_d$ ) curve.

### 13. TFT-Microchannel Electrophoresis

In order to form the microchannel and reservoir structures on the same substrate as the TFT, a thick layer (30  $\mu\text{m}$ ) of negative photoresist, SU-8, was spin-coated and patterned. The microchannel and reservoir areas were defined with a third mask. There was no SU-8 adhesion problem on the top surface of the substrate, which contains the  $\text{SiN}_x$  and Cr. The top of the channel region was covered with a cellulose tape. A small amount of 15.0% polyacrylamide gel (PAGel) solution was fed at the feed reservoir, which automatically filled the channel due to the capillary phenomenon. The gel was polymerized at room temperature within five minutes. The gel solution was composed of 15.0% acrylamide/bis-acrylamide (29:1), 0.75% ammonium persulfate, 0.2% SDS, and 0.3% tetramethyl-ethylenediamine (TEMED) in 0.045M tris-borate and 0.001M EDTA solution at pH 8.2. In this study, the detection electrode (2.8  $\text{mm}^2$ ) was connected to the source electrode of a TFT. The electrical field at the microchannel region was 10 V/cm when the electrophoresis process was carried out between the drain electrode of the TFT and the feed electrode of the microchannel electrophoresis device. A protein mixture containing ovalbumin (45 kDa), carbonic anhydrase (29 kDa), and  $\alpha$ -lactalbumin (14.2 kDa), was prepared by dissolving their lyophilized powders. They were dissolved in a 0.5 $\times$  TBE solution containing 0.2% SDS. The solution was heated to 98 $^\circ\text{C}$  for three minutes to denature the protein. The 0.5 $\times$  TBE solutions (20  $\mu\text{l}$ ) were loaded into both

the feed and the detection reservoirs before electrophoresis.

The electrophoresis was performed by loading 1  $\mu\text{l}$  of protein (1000  $\mu\text{g}/\text{ml}$ ) into the feed reservoir. The current *vs.* time (I-t) was measured with the Agilent 4155C parameter analyzer. The Savitsky-Golay method was used to calculate the  $dI/dt-t$  curve with an order of 3 and 9 data points. To improve PAGel affinity to SU-8 channel surface, the microchannel device was treated with  $\text{O}_2$  plasma, *i.e.*, 5 sccm, at 100 mTorr, 100 W for 30 seconds. By the  $\text{O}_2$  plasma treatment, no interfacial bubble was formed between the PAGel and the SU-8 microchannel sidewall, which means good affinity between these two materials. Electrical properties of the TFTs, such as the output and transfer characteristics, were not influenced by the  $\text{O}_2$  plasma exposure process. The TFT (channel width(W)/channel length(L) ratio of 88/40  $\mu\text{m}$ ) has a field effect mobility of 0.127  $\text{cm}^2/\text{Vs}$ , a threshold voltage of 5.944 V, and a leakage current ( $I_{\text{off}}$ ) below  $10^{-12}$  Amp.

## CHAPTER IV

### SURFACE MODIFICATION OF MICROCHANNEL

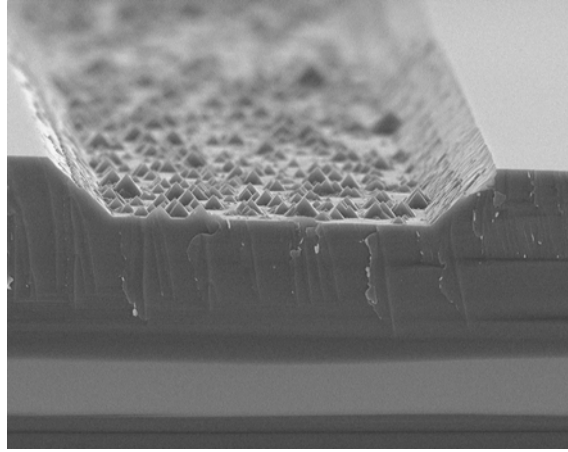
#### 1. Si Microchannel Fabrication

There are two basic methods of fabricating a microelectronic and micromechanic system (MEMS) device. The design can be built on top of the silicon wafer, surface micromachining, or the design can be etched into the wafer using a method called bulk micromachining.<sup>36</sup> For bulk micromachining of Si, a KOH solution is widely used. The main reason for using the KOH to etch Si is its ease and anisotropic pattern.<sup>36,37</sup> Since the etch rate is fast in the  $\langle 100 \rangle$  direction and slow in the  $\langle 111 \rangle$  direction of crystalline Si, a precise three-dimensional structure can be created by KOH etch. For the KOH silicon etchings, the 25–45% at 70–80°C condition is widely used.<sup>36</sup> Since the photoresist (PR) layer will be stripped off with the KOH solution, the non-photoresist mask should be used. Typically,  $\text{SiN}_x$  is widely used as the mask because of the extremely low etch rate in the KOH solution. The addition of surfactant into the KOH solution improves the surface roughness. The principal purpose of surfactant addition is to avoid the formation of bubbles at the surface of the silicon during KOH etching.<sup>37</sup> Therefore, an optimized condition for a smooth surface is determined by concentration of the KOH, etching temperature, and concentration of the additive. Because of successful bulk micromachining with KOH, remarkable developments of microchips could be accomplished, especially in the area of micro-fluidic devices.<sup>36</sup> Figure 17 shows the SEM view of the KOH-etched Si-based microchannels after the removal of

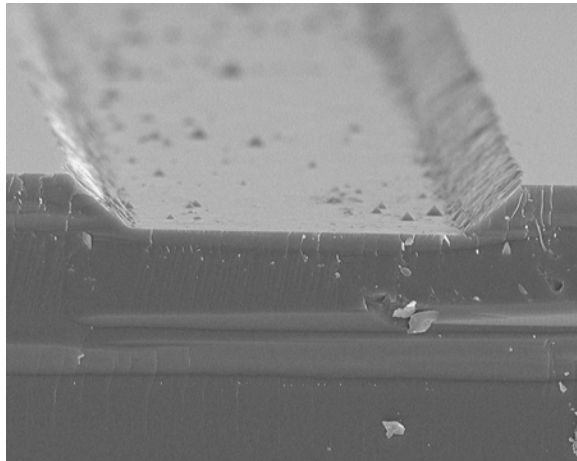
the SiN<sub>x</sub> masking layer with a BOE solution. It has a trapezoidal shape with a bottom angle of 54.74°, which is typical for the KOH-etched Si <100>.<sup>36</sup> As the etch time increases, the top width and depth increase linearly, while the bottom width remains the same as the original mask width. The microchannel of Fig. 17(a) shows much pyramid-shaped roughness at the surface. The microchannel of Fig. 17(b) shows the effect of the addition of 3.0% isopropyl alcohol (IPA) in the KOH solution, *i.e.*, few pyramids were left on the Si surface. The pyramids were formed by the difference of the etching rate in the <100> direction and the <111> direction. The <100> direction has a higher etching rate than the <111> direction. Therefore, the best condition for the smooth surface is to etch <100> and <111> at the same rate. Here, the 30.0% KOH at 70°C supplies equal etch rates at <100> and <111> directions. At a high temperature such as 80°C, the etched line pattern shows cracks and dents on the Si surface. In addition to temperature, the concentration of the KOH is important in the surface roughness or the damage of line patterns. Through an investigation with different temperatures (50°C, 60°C, 70°C, and 80°C) and different KOH concentrations (25.0%, 30.0%, 35.0%, and 40.0%), the 30.0% KOH at 70°C condition gave the smoothly-etched surface, which is consistent with literature report that the 25.0% KOH solution is most popular for this purpose.<sup>37</sup>

## 2. Surface Modification and Protein Affinity

A new microchannel-based SDS-PAGE system, which has *in situ* protein determination without fluorescent driven protein labeling, was fabricated by Si KOH etching.



(a)



(b)

Figure 17. SEM of cross-section view of KOH Si-etched microchannel: (a) with 30.0% KOH solution at 70°C, (b) with 30.0% KOH including 3.0% IPA at 70°C.

The device could be prepared with both silicon substrate and glass substrate. For the glass substrate, SU-8 is a good material for the three-dimensional structure because a high aspect ratio can be formed, and it is easy to process. Proteins were easily separated and identified with this device. Some improved performances of the new device were discussed by preparing devices of various channel cross-sectional configurations and detection electrode sizes. However, protein loss during electrophoresis and initial fluctuation of detection signals are yet to be solved.

For the case of the glass or polymer substrate, many modification methods have been applied. For example, O<sub>2</sub> plasma has been used to add an active surface to polymer. The O<sub>2</sub> plasma adds functional groups, etches polymer, and degrades polymer into low molecular units. To improve the compatibility of the SU-8 surface to polyacrylamide gel, it was treated with the O<sub>2</sub> plasma.

## 2.1. Substrate Surface Structure Influence

Figure 18 shows the chemical structure of cross-linked polyacrylamide. It contains carbonyl (C=O) and amine (-NH<sub>2</sub>) functional groups that are relatively hydrophilic. Therefore, the gel has a high affinity to a hydrophilic substrate. The chemical structure of the acrylamide gel is similar to that of a protein molecule, which contains amide (-CONH-) bonds between amino acid monomers. The polyacrylamide gel is typically used in the hydrated form with a high water content.<sup>2,3</sup> Therefore, the substrate surface should have a function similar to that of a protein in order to have a high polyacrylamide affinity.



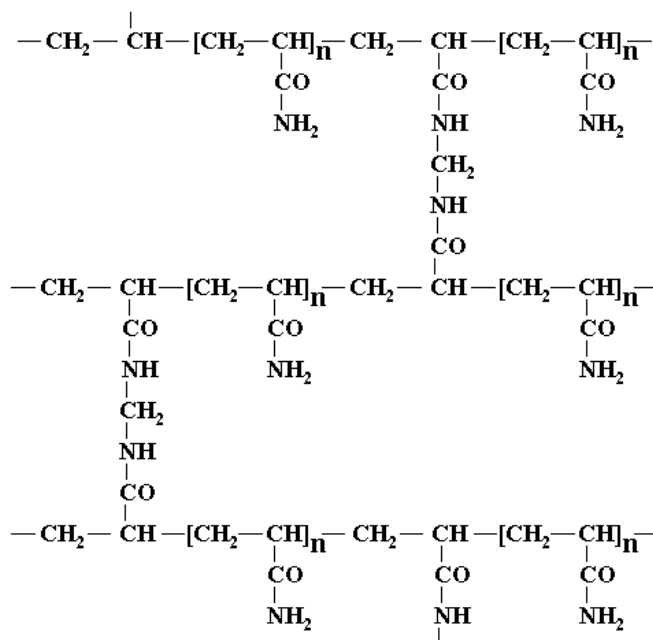


Figure 18. Chemical structure of cross-linked polyacrylamide gel.

Figure 19 illustrates the chemical structure of SU-8.<sup>38</sup> SU-8 can be cross-linked by reacting with an epoxide bond. However, the SU-8 polymer has a rather hydrophobic characteristic because it contains relatively hydrophobic functional groups such as aliphatic hydrocarbon and an aromatic benzene ring. These functional groups cannot form strong hydrogen bonds with carbonyl and amine groups in the polyacrylamide gel. Therefore, the poor affinity of SU-8 to the protein molecule or polyacrylamide gel is expected.

Figure 20 shows microscopic pictures of SU-8-based microchannels (a) without surface treatment and (b) with O<sub>2</sub> plasma treatment. The microchannels are filled with 15.0% polyacrylamide gel stained with 0.01% blue dye (Bromophenol Blue). The blue dye was used to enhance the visual observation of the gel in the channel. Figure 20(a) shows a severe problem of compatibility between the SU-8-based channel and polyacrylamide gel because the surface of SU-8 is rather hydrophobic, while the property of gel is relatively hydrophilic. In polymer technology, the surface modification is often given a strong advantage to minimize such a compatibility problem.<sup>15,38,39</sup> As shown in Fig. 20(b), a dramatic improvement of compatibility between the SU-8 channel surface and the gel is obtained when the SU-8 surface is treated with the O<sub>2</sub> plasma.

The plasma surface treatments involve very complicated mechanisms, which are dependent upon the plasma type, material, atmosphere, and operational conditions, as described in Chapter III. Usually the plasma treatment affects only the top surface layer with a thickness of a few nanometers.<sup>39</sup> Short-time plasma exposure is often used for surface modification.

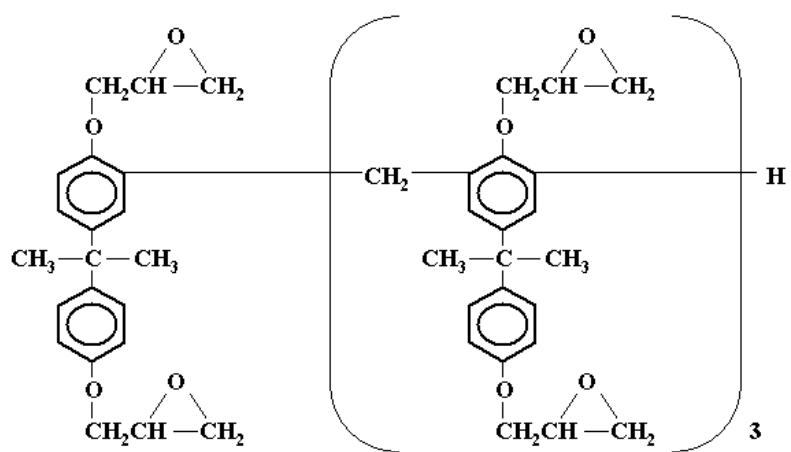


Figure 19. Chemical structure of negative photoresist SU-8. (reference<sup>38</sup>)

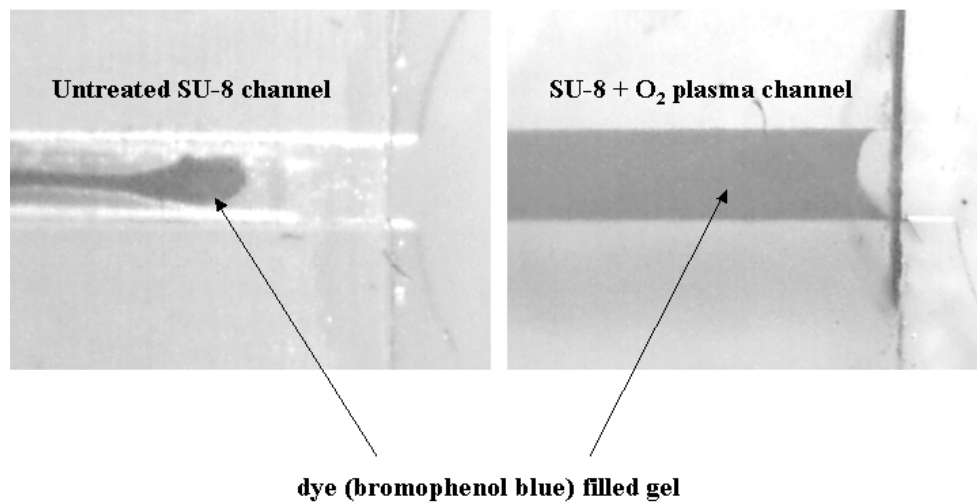


Figure 20. Photograph of gel shrinkage, microscopic pictures of compatibility between SU-8 channel and polyacrylamide gel: (a) with untreated microchannel and (b) with O<sub>2</sub> plasma-treated (one minute) microchannel.

The long-time exposure is not desired because the surface can be seriously damaged. The conditions were chosen to avoid significant surface roughening from the plasma process. No noticeable CO or CO<sub>2</sub>+ emissions representing surface etching were detected during the process by monitoring of optical emission spectroscopy (OES).<sup>40</sup> The carbon oxidations from the O<sub>2</sub> plasma have been frequently reported with common polymer substrate such as PE (Poly Ethylene), PC (Poly Carbonate), and PS (Poly Styrene).<sup>39,40</sup> The stability of O<sub>2</sub> plasma-treated SU-8 was so excellent that the modified surface remains stable after IPA (Iso Propyl Alcohol) washing. Figure 21 shows the C<sub>1s</sub> peaks of the SU-8 surfaces: (a) untreated, (b) O<sub>2</sub> plasma-treated for one minute, and (c) O<sub>2</sub> plasma-treated for five minutes. With reactive species of oxygen radicals, carbons from hydrocarbons and ether bonds are oxidized to form ketone (C=O), carboxylic, and carbonate carbon, which means that O<sub>2</sub> plasma adds new functionalities to the surface.<sup>39</sup> The plasma treatment can change the polymer surface, such as ablation (etching), degradation, cross-linking (branching), and introduction of new functionalities.<sup>39-42</sup> The untreated SU-8 surface contains various hydrophobic groups, such as aromatic rings and epoxy.<sup>41</sup> After the H<sub>2</sub>O/H<sub>2</sub>O<sub>2</sub>/H<sub>2</sub>SO<sub>4</sub> solution oxidation, the SU-8 surface contains more oxygen-containing groups, such as ether and ketone. All of the C<sub>1s</sub> peaks contain SiC peaks at 282.5 eV, which is diffused into SU-8 during baking from the HMDS adhesion promoter. The untreated SU-8 in Fig. 21(a) shows two C<sub>1s</sub> peaks: hydrocarbon (-CH<sub>2</sub>- at 284.6 eV) and ether (-C-O-C- at 286.5 eV). The H<sub>2</sub>O/H<sub>2</sub>O<sub>2</sub>/H<sub>2</sub>SO<sub>4</sub> solution oxidation process introduces more oxidized carbon groups, such as ketone (-C=O at 287.6 eV) and carboxylic (-(C=O)-O- at 288.8 eV), as shown in Fig. 21(b).

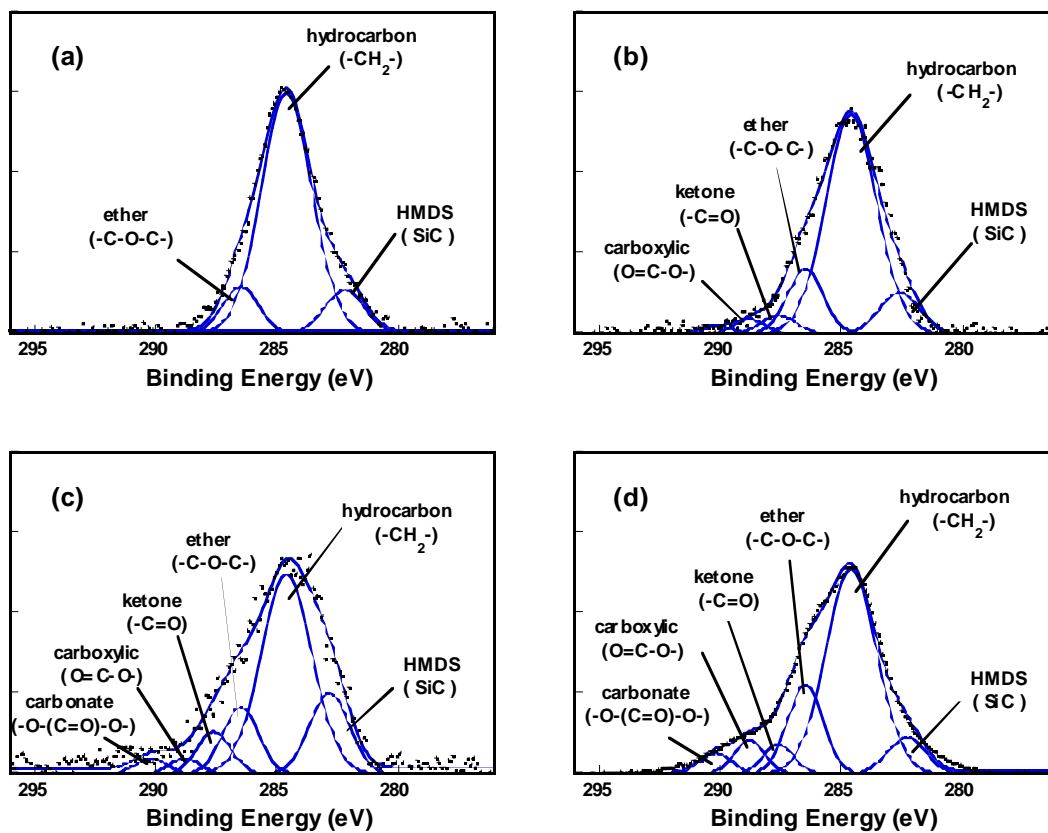


Figure 21. ESCA spectra of  $C_{1s}$ : (a) untreated SU-8, (b)  $H_2O/H_2O_2/H_2SO_4$  oxidized SU-8, (c)  $H_2$  plasma-treated SU-8, (d)  $O_2$  plasma-treated SU-8.

The solution oxidation process added very small proportions of ketone and carboxylic groups. The contact angle of the DNA solution increases only slightly after the oxidation process. The additional oxygen does not show a major impact on the solution affinity. However, as shown in Fig. 21(c) and (d), both H<sub>2</sub> and O<sub>2</sub> plasma treatments add a large amount of oxidized carbon groups such as carbonate (-O-(C=O)-O- at 290.2 eV) to the surface. The H<sub>2</sub> plasma treatment usually adds hydrophobic groups, such as CH or CH<sub>2</sub>, to the SU-8 surface. On the other hand, the H<sub>2</sub> plasma can etch some surface groups and create unsaturated dangling bonds. These bonds are easily oxidized in air to form more hydrophilic groups, such as a hydroxyl bond, which can increase its hydrophilicity.<sup>42,43</sup> Table V shows that concentrations of carbon functional groups on SU-8 surfaces are dependent upon the O<sub>2</sub> plasma exposure time, which is calculated from the fitted C<sub>1s</sub> peaks. With the O<sub>2</sub> plasma treatment, the carbon oxidation content calculated from fitted C<sub>1s</sub> peaks of ketone (-C=O at 287.6 eV), carboxylic -(C=O)-O- at 288.8 eV), and carbonate (-O-(C=O)-O- at 290.2 eV) increases from 10.5% to 29.0% and 32.1%, respectively with the plasma treatment time.

## 2.2. Substrates Effects on Protein Affinity

During microchannel electrophoresis, a significant loss of protein on the channel wall has been reported due to physical and chemical properties of the wall material.<sup>7,11</sup> Surfaces of various materials were tested for the protein adsorption. ESCA was used to detect the possible small amounts of protein remained on the surface.

Table V. Percentage of carbon functional groups in untreated and O<sub>2</sub> plasma-treated SU-8 surface.

Chemical proportion in C <sub>1s</sub> (%)	untreated SU-8	SU-8 + O <sub>2</sub> plasma (one minute)	SU-8 + O <sub>2</sub> plasma (five minutes)
carbonate (-O-(C=O)-O-)	0.0	2.6	3.6
carboxylic ((C=O)-O-)	0.0	6.3	5.9
ketone (-C=O)	0.1	5.5	5.0
ether (-O-C-O-)	10.4	14.6	17.6
hydrocarbon (-CH <sub>2</sub> -)	78.4	62.9	60.1
HMDS	10.8	8.1	7.8



Figure 22 shows the ESCA spectra of (a) the O<sub>2</sub> plasma modified SU-8 for one minute and (b) plain glass substrate which was dropped with a protein solution containing 113 µg/ml ovalbumin (45 kDa) after protein solution incubation and removal. The two substrates showed different results. For example, with the modified SU-8 substrate, no nitrogen or sulfur from protein was detected, as shown in Fig. 22(a). As shown in Fig. 22(b), small amounts of nitrogen and sulfur elements were detected on the glass substrate. They are protein molecules, *i.e.*, S<sub>2p</sub> (165.4 eV) and N<sub>1s</sub> (401.9 eV) peaks. The former is contributed by the thiol (SH) and sulfide (SCH<sub>3</sub>) bonds. The latter is contributed by nitrogen containing rings (indole, imidazole) and amides (CONH). Therefore, the affinity of the protein molecule is the highest on the glass surface. Glass is not a suitable substrate for low protein adsorption. Otherwise, it will contribute to the loss of protein to the channel structure. If the glass must be used to build this kind of device, it should be coated with a SiO<sub>2</sub> or SiN<sub>x</sub> film, which does not adsorb proteins.

### 2.3. Substrate Effects on Solution Affinity

Contact angle measurement can be used to determine the wettability of the substrate surface with the protein solution, which often influences the performance of the microchannel device.<sup>41,42</sup> The contact angle of a liquid drop is determined by the balance of three kinds of energies, *i.e.*, surface-gas ( $\gamma_{sg}$ ), surface-liquid ( $\gamma_{sl}$ ), and gas-liquid ( $\gamma_{gl}$ ), which is shown below:

$$\gamma_{sg} = \gamma_{sl} + \gamma_{gl} \cos \theta \quad [24]$$

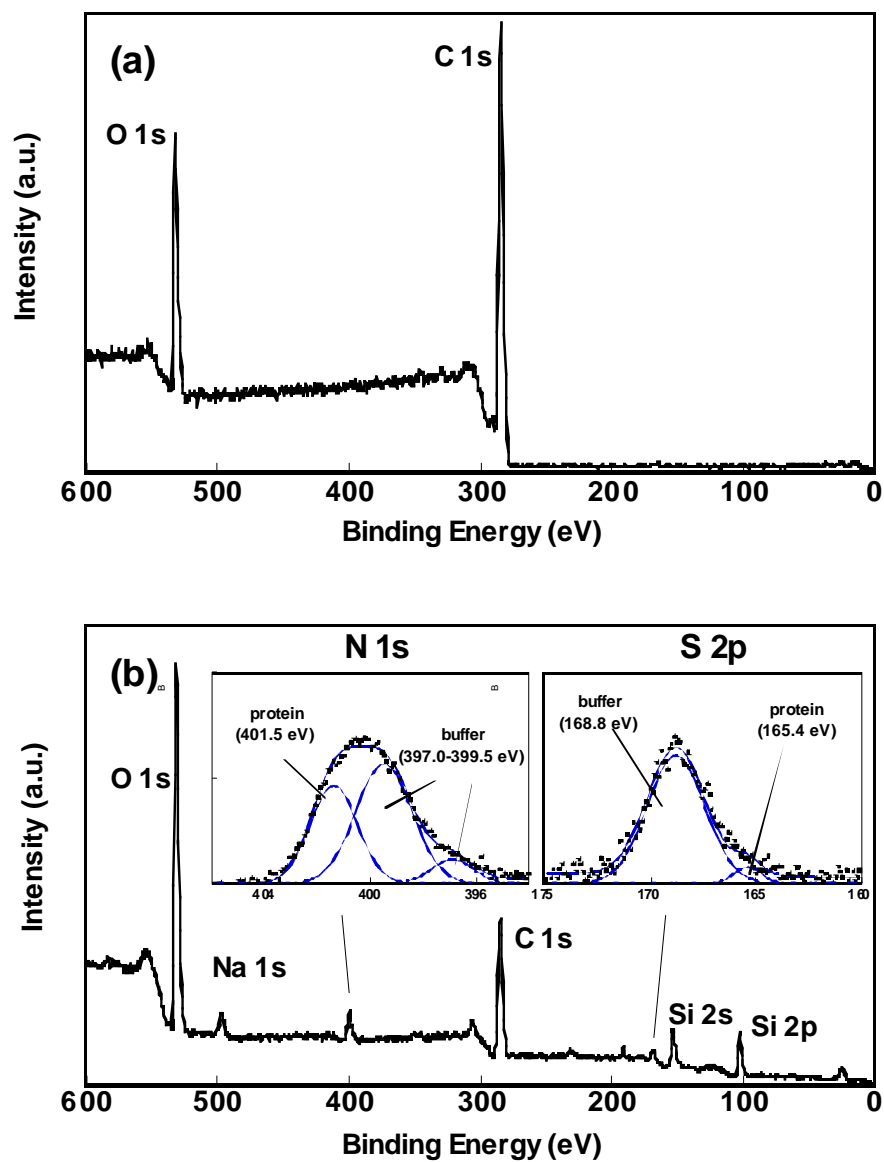
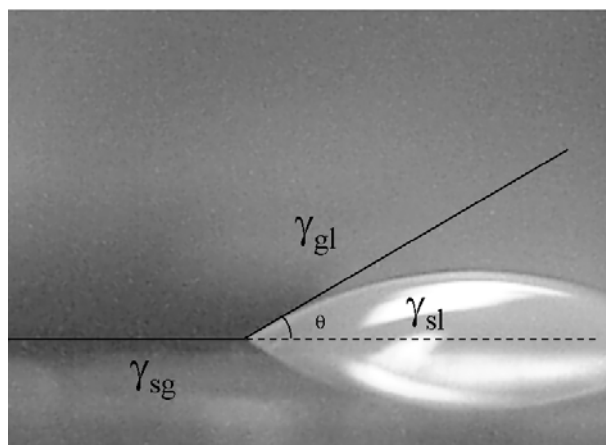


Figure 22. ESCA spectra for remaining protein after affinity examinations on (a) the modified SU-8 (one minute) and (b) plain glass substrate.

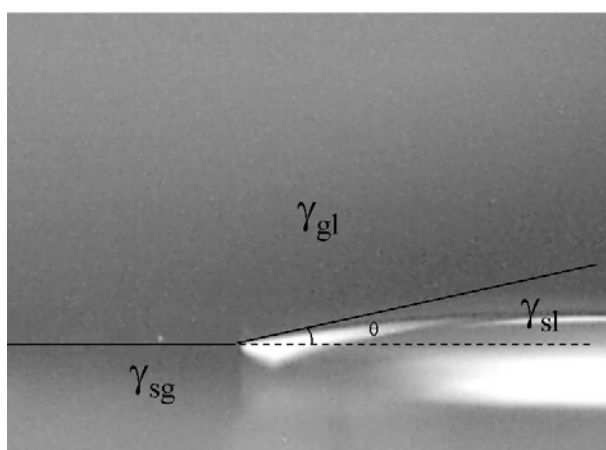
where  $\theta$  is the contact angle between the surface and the liquid. For the same solution,  $\gamma_{sg}$  and  $\gamma_{gl}$  are independent of the substrate surface structure. However,  $\gamma_{sl}$  is a function of the solution component and the surface structure. A large  $\gamma_{sl}$  means a low contact angle, which corresponds to a high solution affinity to the substrate surface.

Figure 23 shows contact angles (a) between the sputtered SiO<sub>2</sub> surface and DI water, and (b) between the glass surface and a 0.5× TBE buffer solution containing 0.2% SDS. The adhesive force between the glass and the buffer solution is lower than that between SiO<sub>2</sub> and DI water because the contact angle in Fig 23(b) is lower than the contact angle in Fig 23(a).

Table VI shows the result of the contact angle measurement of ten different substrates in contact with four different kinds of solutions. The contact angles of DI water on various substrates are different from those of buffer solutions. The buffer solution is a mixture of 0.045 M tris-borate, 0.001 M EDTA, and 0.2% SDS at pH 8.2. The protein solution contains 2000 μg/ml of ovalbumin (45 kDa), carbonic anhydrase (29 kDa), and α-lactalbumin (14.2 kDa) proteins dissolved in the TBE buffer. The polyacrylamide solution contains acrylamide/bisacrylamide (29:1) gel components in 0.5× TBE buffer. The polyacrylamide solution has a higher contact angle value than the other three solutions, except for the cellulose tape surface or the O<sub>2</sub> plasma-treated cellulose substrates. SDS (Sodium Dodecyl Sulfate) in the buffer, polyacrylamide, and protein solutions is a surfactant, which reduces the surface tension of the droplet and lowers the contact angle. Therefore, the contact angle of the DI water is higher than those of the other three SDS containing solutions on the same substrate surface.



(a)



(b)

Figure 23. (a) Contact angle of DI water on the sputtered SiO<sub>2</sub>, and (b) contact angle of 0.5x TBE buffer with 0.2% SDS on the glass.

Table VI. Contact angles of various solutions on various substrates.

Substrates	DI water (°)	Buffer solution (°)	Protein solution (°)	15% acrylamide solution (°)
Bare silicon	77.8	35.4	36.7	52.0
PECVD SiN <sub>x</sub>	46.8	9.9	13.6	12.3
Sputtered SiO <sub>2</sub>	22.4	12.8	15.9	23.5
Glass	24.6	10.6	12.5	18.4
Untreated SU-8	76.7	42.1	43.7	57.7
SU-8 + O <sub>2</sub> plasma ( 1 min. )	33.8	9.5	17.1	18.6
SU-8 + O <sub>2</sub> plasma ( 5 min. )	33.4	8.9	12.5	16.4
Cr	35.1	15.1	19.8	18.7
Cellulose	45.5	65.9	77.7	84.0
Cellulose + O <sub>2</sub> plasma ( 1 min. )	16.1	18.7	55.9	59.0

In Table VI, the contact angle of DI water on the O<sub>2</sub> plasma-treated SU-8s is around 33°, which is larger than that of DI water or other O<sub>2</sub> plasma-treated polymer surfaces, such as SAN (Styrene Acrylonitrile copolymer), PS, and PC.<sup>41,42</sup> However, the SAN, PS, and PC polymer surfaces needed higher O<sub>2</sub> plasma power (> 200 W), or higher feeding O<sub>2</sub> flow rate (> 15 sccm) than the SU-8. When two contact angles of DI water or protein solution on one minute and five minutes O<sub>2</sub> plasma-treated SU-8 surfaces are compared, they are little different. Therefore, in order to prepare a relatively hydrophilic surface, plasma parameters such as power and O<sub>2</sub> flow rate are more important than the plasma treatment time.

For all substrates, the buffer solution has a smaller contact angle than those of the polyacrylamide solution and protein solution, although they contain the same kind of buffer component. This indicates that protein and polyacrylamide molecules counter the effect of the surfactant. For the cellulose or modified cellulose tape, the existence of surfactant does not affect the contact angle. The contact angle seems to be dependent solely on the total concentration of the solute in the solution. The polyacrylamide solution has 23.9% of solute, the protein solution has 9.1% of solute, the buffer solution has 8.9% of solute, and the DI water has 0.0% of solute. The contact angle of the solution on the unmodified or modified cellulose tape is in the order of polyacrylamide solution > protein solution > buffer solution > DI water. The solute concentration effect is due to the change of the viscosity. The concentration vs. contact angle relationship also holds for the other substrates. Therefore, except for SiN<sub>x</sub> and Cr, we can conclude that the solution's contact angle increases with the increase of solute concentration.

For solutions containing the surfactant, SiN<sub>x</sub>, Cr, and modified SU-8 surfaces' contact angle of the protein solution and the polyacrylamide solution are almost the same over a large range (23.9% vs. 9.1%) of solute concentration. Therefore, the protein molecule affects the solution's physical and chemical properties, which influences the contact angle result. No apparent protein adsorptions were detected with these SiN<sub>x</sub>, Cr, and modified SU-8 substrates, judged from ESCA result. The surface modification effects were also shown in the contact angle data with the SU-8. For all solutions, the contact angle decreases when the surface O<sub>2</sub> plasma treatment time is increased. Therefore, surface modification of SU-8 is desirable if it is used to fabricate the microchannel structure. The cellulose and the modified cellulose are very sensitive to viscosity of the solution.

The SiN<sub>x</sub>, SiO<sub>2</sub>, Cr, and plasma-treated SU-8 surfaces show more hydrophilic behaviors with DI water, while they show high affinity to the solution containing the surfactant. Therefore, for these substrates, the SDS surfactant is important to the affinity between the substrate surface and the solution. However, the contact angle difference between the substrate surface and the solution. However, the contact angle difference between the buffer solution and protein solution (or polyacrylamide solution) is relatively small on the SiN<sub>x</sub> and glass substrates. It is much larger on other substrates. It is possible that the protein may have a strong adsorption, which explains protein losses during electrophoresis with the glass device in Liu *et al.*'s report.<sup>7</sup> The small contact angle on the glass substrate is consistent with the ESCA result protein adsorption. Therefore, the direct contact between the glass surface and the protein solution must be avoided in the fabrication of the microchannel device.

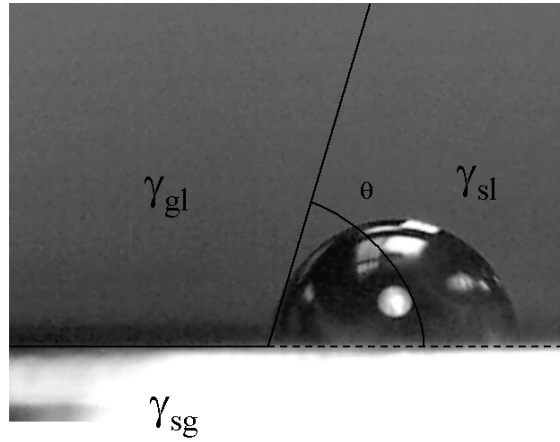
### 3. Substrate Surface Influence on DNA Affinity

Contact angle is a reference of the DNA solution affinity to the substrate surface. The contact angle is dependent upon the substrate surface structure and solution composition, such as the DNA content or the ionic strength of a solution.

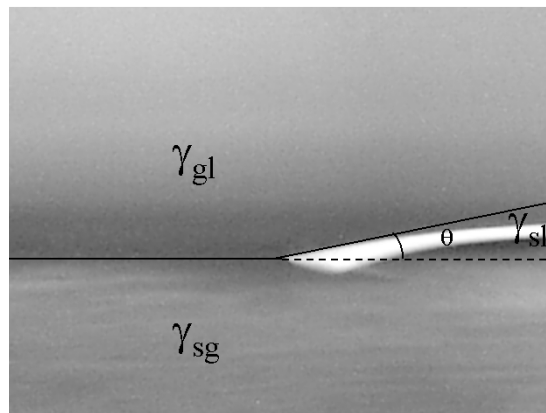
Figure 24 shows the contact angle of DNA solution on (a) untreated and (b) solution-oxidized glass. The contact angle of the solution-oxidized glass is much lower than that of the untreated glass. Table VII shows the contact angles of DI water and DNA solution on various surfaces. For bare Si, PECVD SiN<sub>x</sub>, and glass, the contact angles of the DNA solution are slightly lower than those of the DI water, *e.g.*, by 0.8° to 2.3°. However, on the SiO<sub>2</sub> and SU-8, the contact angles of the DNA solution are much lower than those of the DI water. A SiO<sub>2</sub> surface, which has a surface chemical structure similar to a silica, has Si-O, Si-O<sub>2</sub>, and a small number of Si-OH groups when it is under an aqueous solution.<sup>3,20,45</sup> These groups show hydrophilic properties. Since the backbone of a DNA strand carries relatively hydrophilic phosphate groups (PO<sub>4</sub><sup>2-</sup>), the hydrophilic interaction between the ionized oxide groups and the backbone of a DNA molecule increases the affinity.

This is also clearly shown in the contact angle difference of the DNA solution on the bare Si (75.6°) and on the SiO<sub>2</sub> (11.4°). Therefore, the bare Si surface can be easily modified to change its affinity to DNA molecules. In addition, a long chain DNA molecule is also known to have a rather hydrophobic interaction with a polymer surface.<sup>44</sup> In Table VII, the contact angle between the SU-8 and the DNA solution is significantly lower than that between the SU-8 and DI water, *i.e.*, 48.8° vs. 76.7°.





(a)



(b)

Figure 24. Contact angle of DNA solution on (a) glass substrate and (b) solution-oxidized glass.

---

Table VII. Contact angle of DNA solution on various substrates.

Substrate	Contact angle (°)	
	DI water	EcoR I $\lambda$ DNA solution
Bare Si	77.8	75.6
PECVD SiN <sub>x</sub>	46.8	44.5
Glass	24.6	23.8
SiO <sub>2</sub>	22.4	11.4
SU-8	76.7	48.8
Cr	35.1	58.9

---

The contact angle on a Cr surface is different from those on the other substrates, *i.e.*, bare Si, PECVD SiN<sub>x</sub>, glass, SiO<sub>2</sub>, and SU-8 surfaces. The contact angle of the DNA solution on the Cr surface is higher than that of the DI water, *i.e.*, 58.9° vs. 23.8°. The DNA solution, which contains 30.0% of solute, is more viscous and has a higher surface tension than the DI water. Since there is a lack of a strong attraction between the DNA solution and the Cr, the bulk solution property probably controls the contact angle. Although bare Si, PECVD SiN<sub>x</sub>, and glass surfaces all contain silicon atoms on the surface, there are noticeable differences in contact angles between the DNA solution and DI water. Therefore, silicon alone does not explain the contact angle change. For those film surfaces, functional groups such as Si-O, Si-N, Si-OH, and Si-ON are critical to the surface affinity of DNA or water molecules.

Table VIII shows the contact angles of the DNA solution on various substrates with or without being oxidized with the H<sub>2</sub>O/H<sub>2</sub>O<sub>2</sub>/H<sub>2</sub>SO<sub>4</sub> solution, or hydrogenated with H<sub>2</sub> plasma. Except for SU-8, most substrates show the decrease of the contact angle after surface oxidization. For Si, the decrease of the contact angle is drastic, *i.e.*, changing from 75.6° to 7.5°. For SiN<sub>x</sub>, glass, and Cr, a large drop in contact angle was also observed. The Si, PECVD SiN<sub>x</sub>, and glass surfaces contain many Si atoms on the surface. The silicon atoms are known to be oxidized into the Si-OH rich oxide layer by the H<sub>2</sub>O/H<sub>2</sub>O<sub>2</sub>/H<sub>2</sub>SO<sub>4</sub> solution treatment.<sup>20</sup>

Figure 25 shows ESCA spectra of Si<sub>2p</sub> on various Si and glass surfaces. Fig. 25(a) and (d) show Si<sub>2p</sub> peaks from the untreated Si and glass surfaces: Fig. 25(b) and (e) are the solution-oxidized Si and glass surfaces:

---

Table VIII. Contact angle of DNA solution on various modified substrates.

Original substrate	Contact angle (°)		
	No treatment	After solution (H <sub>2</sub> O/H <sub>2</sub> O <sub>2</sub> /H <sub>2</sub> SO <sub>4</sub> ) oxidation	After H <sub>2</sub> plasma oxidation
Bare Si	75.6	7.5	66.4
PECVD SiN <sub>x</sub>	44.5	19.1	57.8
Glass	23.8	10.6	24.2
SU-8	48.8	49.2	44.1
Cr	58.9	23.6	60.5

---

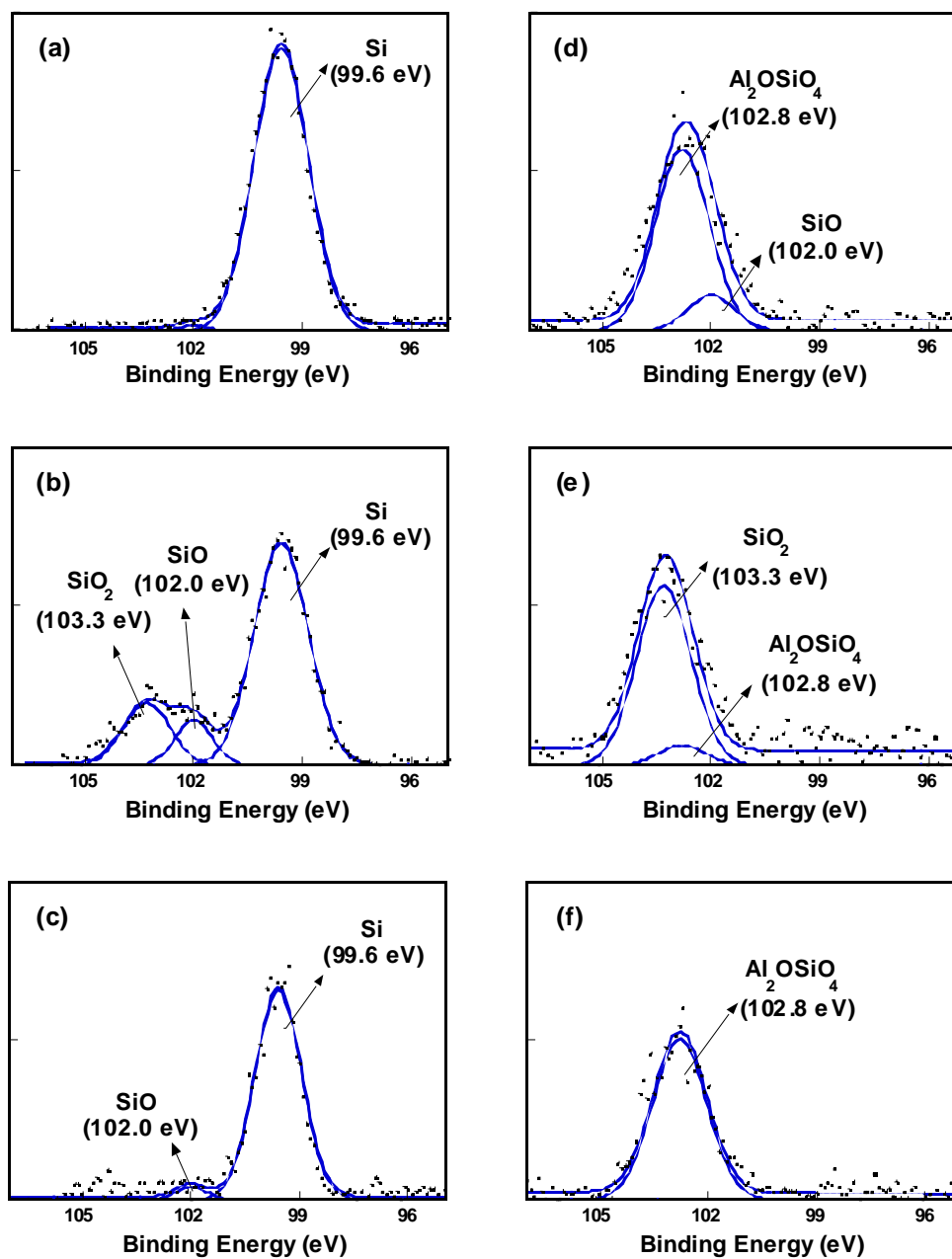


Figure 25. ESCA spectra of  $\text{Si}_{2p}$ : (a) bare Si, (b)  $\text{H}_2\text{O}/\text{H}_2\text{O}_2/\text{H}_2\text{SO}_4$  oxidized Si, (c)  $\text{H}_2$  plasma-treated Si, (d) glass, (e)  $\text{H}_2\text{O}/\text{H}_2\text{O}_2/\text{H}_2\text{SO}_4$  oxidized glass, and (f)  $\text{H}_2$  plasma-treated glass.

Fig. 25(c) and (f) are the plasma-hydrogenated Si and glass surfaces. The bare Si, with the native oxide removed, shows a Si-Si bond at 99.6 eV. However, the oxidized Si contains two additional Si<sub>2p</sub> peaks corresponding to Si-O at 102.0 eV and Si-O<sub>2</sub> at 103.3 eV. The glass surfaces show a characteristic Si<sub>2p</sub> peak at 102.8 eV, which is contributed by its component of aluminum oxide silicate (Al<sub>2</sub>O<sub>3</sub>SiO<sub>4</sub>). However, after oxidation, the glass surface contains a strong peak corresponding to Si-O<sub>2</sub> at 103.3 eV, as shown in Fig 25(e). The formation of Si-O and Si-O<sub>2</sub> bonds explains the results of the decreasing contact angle of the oxidized Si and glass surface.

The H<sub>2</sub> plasma-treated Si, as shown in Fig. 25(c), shows a small Si-O peak at 102.0 eV. The H<sub>2</sub> plasma probably created dangling bonds on Si surfaces, which were oxidized in the air before ESCA analysis. The small amount of Si-O bond makes the surface slightly more hydrophilic than the untreated surface, which is consistent with the contact angle change.

The H<sub>2</sub> plasma treatment removes the Si-O Si<sub>2p</sub> peak at 102.0 eV from the glass surface, as shown in Fig. 25(e). This indicates that the plasma hydrogenation can reduce the oxygen concentration on the glass surface, which makes this surface slightly more hydrophobic than that of the untreated glass. This is consistent with the result in Table VIII.

The contact angle of PECVD SiN<sub>x</sub> increases after the H<sub>2</sub> plasma from 44.5° to 57.8°. The H<sub>2</sub> plasma can attack PECVD SiN<sub>x</sub> etching off Si- or N-containing groups to form dangling bonds.<sup>29</sup> These dangling bonds are easily oxidized to form various oxygen-containing groups, which are rather hydrophilic. At the same time, hydrogen can

passivate the dangling bonds. The hydrogenated surface is usually relatively hydrophobic, which is responsible for the high contact angle. Therefore, for a surface that contains Si atoms, the chemical states of the Si atoms are critical to the surface affinity of the solution.

The H<sub>2</sub> plasma-treated SU-8 contains more ketone and carboxylic groups than the solution-oxidized surface, as already shown in Fig. 21. The H<sub>2</sub> plasma treatment usually adds relatively hydrophobic groups or generates dangling bonds on carbon atoms at the surface, which are easily oxidized to be rather hydrophilic when exposed to air.<sup>42</sup> The result in Table VIII shows that the H<sub>2</sub> plasma makes the SU-8 surface more hydrophilic. Therefore, plasma hydrogenation can make the SU-8 surface more hydrophilic or hydrophobic, depending upon the final surface structure and the solution component.

The DNA solution contains a large amount of ions and DNA fragments, both of which can lower the surface tension of the drop and decrease the contact angle. The contact angle of the DNA solution on SU-8 is lower than that of DI, as shown in Table VII. However, the contact angle of the DNA solution changes a little after oxidation or hydrogenation, as shown in Table VIII. The solution's surface tension, which is a function of the content of ions and DNA fragments, is probably more critical than the SU-8's surface functional groups in determining the contact angle.

## CHAPTER V

### MICROCHANNEL ELECTROPHORESIS OF PROTEIN AND DNA\*

#### 1. Microchannel Electrophoresis for Protein Analysis

A microchannel device for protein electrophoresis was fabricated on silicon substrate. Due to the small size of a protein molecule, a high-density gel is required as an effective sieving material for the protein electrophoresis. Therefore, a high concentration, *e.g.*, 15.0% polyacrylamide gel, was applied to the microchannel device for the protein analysis. Devices with different sizes of microchannel configurations and detection electrode areas were fabricated and investigated. An optimized fabrication condition for an enhanced detection signal could be obtained. In addition, the amount of each protein on the detection electrode could be quantified by the device's current and time (I-t) curve. The detected protein amount could be compared with the actual amount loaded in the feed solution before the beginning of the electrophoresis.

##### 1.1. Adsorption of Protein on Electrode

Adsorption of proteins onto a metal electrode surface is a well-known problem in the electrochemical analysis of clinical samples. The adsorption of protein on a metal electrode is usually an irreversible process.<sup>12</sup>

---

\* Part of this chapter is reprinted with permission from "Microchannel Electrophoresis Device for Separation and *in situ* Detection of Proteins" by Y. Kuo and H.H. Lee, 2001, *Electrochemical and Solid-State Letters*, 4[10], H23-H25, 2004 by the Electrochemical Society.



In the report of Guo *et al.*,<sup>12</sup> platinum, gold, and glassy carbon of the electrode with HSA (Human Serum Albumin) were used for protein adsorption tests. By the method of the quartz-crystal microbalance (QCM) technique, the amount of protein adsorbed on the metal surface can be roughly estimated.<sup>12</sup> However, accurate estimation of mass loading on the quartz resonator is very difficult because the resonant frequency is sensitive not only to mass loading but also to viscosity, elasticity, surface roughness.<sup>12,13</sup> Recently, Cabilio *et al.* investigated adsorption behavior of various kinds of proteins onto a metal electrode.<sup>13,14</sup> Using a cyclo-voltammetry method, they were successful in quantifying the amount of adsorbed proteins onto metal electrodes. Therefore, under the influence of a properly applied electric field, protein molecules will be adsorbed onto the surface of a metallic electrode, and the amount of adsorbed proteins can be estimated by delicate electrochemical methods.<sup>12</sup>

## 1.2. Detection Electrode Contact Resistance vs. Device Configurations

Figure 26 shows the cross-sectional view of a microchannel device and the schematic of a corresponding circuit. The total resistance between the two electrodes,  $R_{total}$ , is composed of five resistors connected in a series as shown below:

$$R_{total} = \sum_{i=1}^5 R_i \quad [25]$$

where  $R_1$  is the contact resistance between the feed electrode and the solution in the reservoir;  $R_2$  is the resistance of the solution in the feed reservoir, which is a function of the buffer solution component and protein concentration;  $R_3$  is the channel resistance,

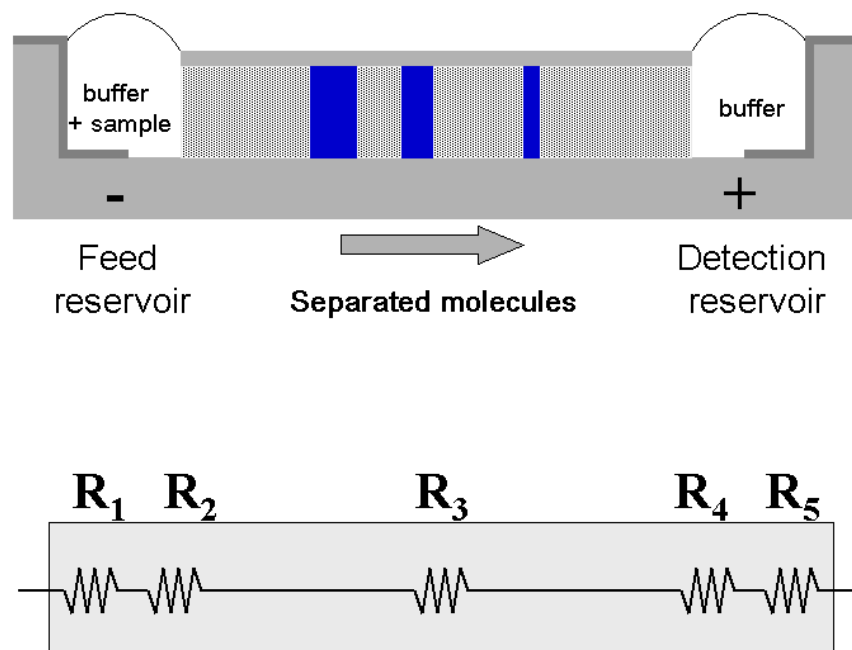


Figure 26. Cross-sectional view of a microchannel device and the schematic resistance model of a corresponding circuit.

which is a function of parameters such as the gel concentration, channel length, and channel cross-sectional area;  $R_4$  is the resistance of the solution in the detection reservoir, which depends upon the buffer solution composition; and  $R_5$  is the contact resistance between the detection electrode and the solution in the reservoir. When a protein is adsorbed on the detection electrode surface,  $R_{\text{total}}$  increases instantaneously due to the drastic increase of  $R_5$ . During a typical operation, the compositions of the gel and the buffer solution are fixed. The two resistances  $R_2$  and  $R_4$  are usually negligible compared with other resistances, because they are composed of highly conductive ions and electrolytes. The  $R_1$  can be taken as a constant because the SDS-coated proteins are driven away from the feed electrode.

Figure 27 shows the measured  $R_{\text{total}}$  as a function of the cross-sectional area of the channel. The resistances were measured with the entire system filled with the buffer solution, *i.e.*, no gel or protein existence. Measurement of the  $R_{\text{total}}$  with four kinds of channel cross-sectional size (8.0, 17.5, 20.3, and 30.2  $\mu\text{m}$  deep, 440  $\mu\text{m}$  wide at bottom and 500-530  $\mu\text{m}$  wide at top) and four different detection electrode areas (0.75 $\times$ 1.5  $\text{mm}^2$ , 1.4 $\times$ 1.5  $\text{mm}^2$ , 2.25 $\times$ 1.5  $\text{mm}^2$ , and 3.0 $\times$ 1.5  $\text{mm}^2$ ) were performed. The  $R_{\text{total}}$  was calculated by dividing the voltage with the current measured over a period of 30 seconds. The size of the feed electrode was kept constant at 2.0 $\times$ 2.0  $\text{mm}^2$ . Figure 27 shows that the resistance  $R_{\text{total}}$  increases with the decrease of the channel cross-sectional area or the detection electrode size. If the channel region is taken as a conductor, such as a wire, the  $R_3$  should be inversely proportional to the cross-sectional area size as shown below:

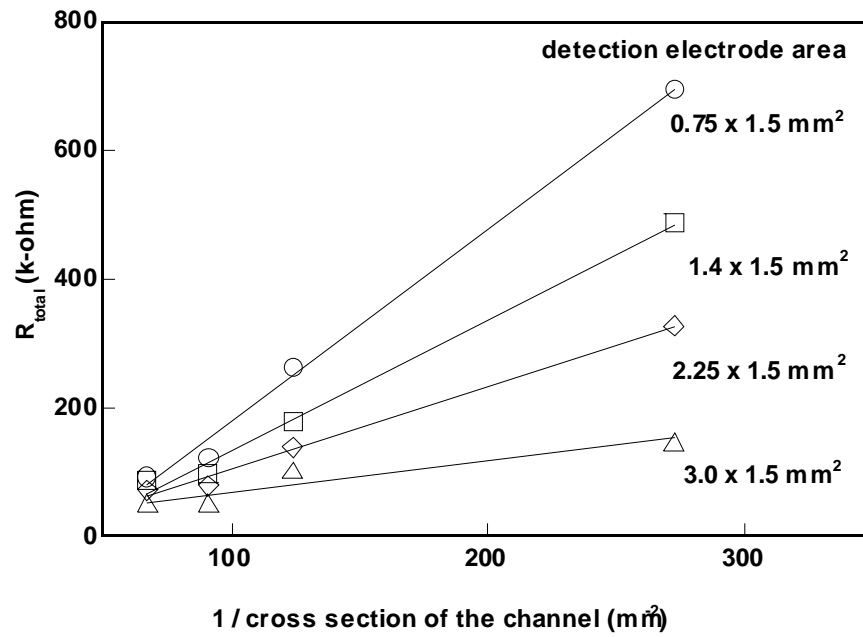


Figure 27. The  $R_{total}$  with combination of four kinds of channel cross-section sizes and four kinds of detection electrodes.

$$R_3 = \rho \frac{l}{A} \quad [26]$$

where  $\rho$  is the resistivity,  $A$  is the cross-sectional area, and  $l$  is the length of the channel. The resistivity,  $\rho$ , is dependent upon the property of the channel such as the composition of the solution in the channel. Therefore, the Fig. 27 result is qualitatively consistent with equation [26]. The decrease of  $R_{\text{total}}$  with the increase of the detection electrode area shows that the resistance is an important factor in the circuit. For the practical application, the  $R_{\text{total}}$  value should be as low as possible. At the same time, the current drop during the adsorption of proteins on the detection electrode should be as large as possible. The  $R_{\text{total}}$  in Fig. 27 is very high, *e.g.*,  $> 100 \text{ k}\Omega$ , when the channel's cross-sectional area is small or the detection electrode area is small. The former is contributed by the large  $R_3$  from the narrow channel cross-sectional area. The latter is due to the very large  $R_5$ . The high  $R_3$  could cause the undesirable overheating of the solution during the operation. In order to avoid this effect, the channel's cross-sectional area should be large. On the other hand, in order to maximize the detection signal, the detection electrode area should be small. Therefore, these two parameters need to be optimized for practical applications.

Figure 28 shows influences of gel and protein to the total resistance in the device with various sizes of detection electrodes.  $R_A$  is the total resistance without gel or protein,  $R_B$  is the total resistance with 15.0% polyacrylamide gel but no protein, and  $R_C$  is the total resistance with the channel filled with 15.0% polyacrylamide gel and the feed solution containing a protein (2.5  $\mu\text{g}$  of  $\alpha$ -lactalbumin).

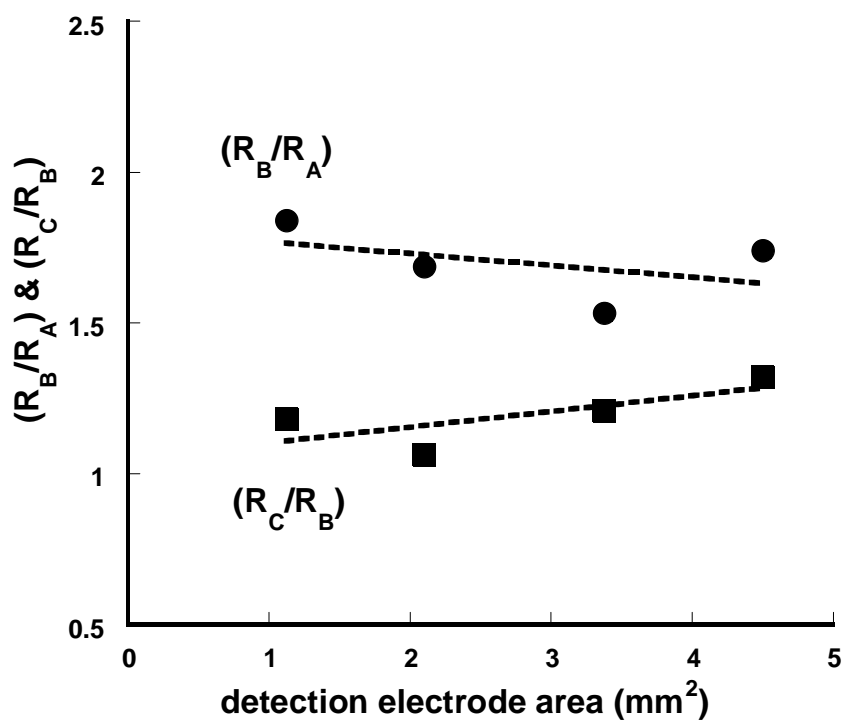


Figure 28. Measurement of the total resistance ( $R_{\text{total}}$ ) with or without gel in microchannel and protein loading at feed reservoir.

Under all channel conditions, the  $R_{\text{total}}$  decreased with the increase of the electrode area, which is similar to the result in Fig. 27.

Four conclusions can be summarized from Fig. 28: (i) the total resistance of the device increases more than 50.0% when the channel is filled with the gel compared with the buffer solution only, (ii) the difference in (i) increases slightly with the decrease of the detection electrode, (iii) the total resistance of the device increases slightly when the protein solution is introduced into the gel-filled device, and (iv) the difference in (iii) decreases very slightly with the decrease of the detection electrode area. These results indicate that, in the actual protein separation process, the channel resistance  $R_3$  is an important portion of the total resistance  $R_{\text{total}}$ . The existence of protein in the feed solution has a limited effect on  $R_{\text{total}}$ . Since, for the separation of proteins, it is necessary to fill the channel with the gel, the change of the detection electrode contact resistance  $R_5$  needs to be high when a protein is adsorbed.

### 1.3. Separation of Multiple Proteins in a Fluid Solution

Figure 29 shows the Coomassie Brilliant Blue R250-stained electrodes after the microchannel device was operated for 900 seconds. The original feed solution contained one type of protein ( $\alpha$ -lactalbumin) with a concentration of 112  $\mu\text{g/ml}$ . The detection electrode shows a blue spot, which indicates the existence of protein. The same figure also shows that the protein was adsorbed at the nearest region from the channel outlet. The similar result was obtained with other types of proteins adsorbed on the electrode after electrophoresis.<sup>6,7</sup>

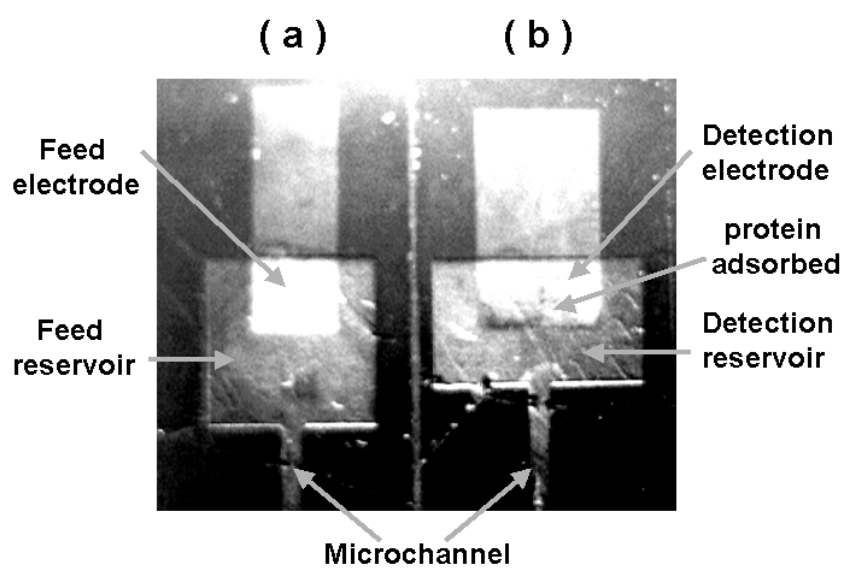


Figure 29. Coomassie Brilliant Blue R250-stained protein profile on detection electrode.



After the electrophoresis experiment, the surface of the detection electrode was analyzed with ESCA to further verify the existence of protein. Binding energies of  $N_{1s}$  and  $S_{2p}$  were examined because most proteins contain these two elements in functional groups.

Figure 30 shows the  $N_{1s}$  and  $S_{2p}$  ESCA peaks of the adsorbed protein on the detection electrode surface (a) with and (b) without ovalbumin in the  $0.5\times$  TBE solution (containing 0.2% SDS). The  $N_{1s}$  (399.0 eV) comes from the amine group of tris-borate and EDTA in the buffer solution. However, the  $N_{1s}$  (402.0 eV) peak comes from the nitrogen containing rings (indole, imidazole) and amides (CONH) in the protein structure. The  $S_{2p}$  (169.4 eV) peak in Fig. 29(b) comes from sulfates of SDS in the buffer solution. The  $S_{2p}$  (163.2 eV) peak in Fig. 29(a) is probably contributed by the thiols (SH) and sulfides ( $SCH_3$ ) of the protein. In addition, the intensity of total nitrogen peaks with the existence of protein is much larger than those without the existence of protein. During the protein separation process, the  $R_{total}$  varies little with respect to time. However, upon arriving at the detection reservoir, proteins are quickly transported to the anode and are strongly absorbed on the electrode surface. Since the anode area is small in the microchannel device, the adsorbed protein molecules easily block its surface.<sup>12</sup> The increase of the contact resistance  $R_5$  is determined by the percentage of the electrode surface being blocked. In general, the  $R_{total}$  increases with the number of the proteins adsorbed on the anode.

Figure 31(a) shows the current-time (I-t) diagram of a microchannel device of which the feed solution contains two types of proteins, *i.e.*, carbonic anhydrase (29 kDa) and ovalbumin (45 kDa), with concentration of 325  $\mu\text{g/ml}$  in the  $0.5\times$  TBE solution.

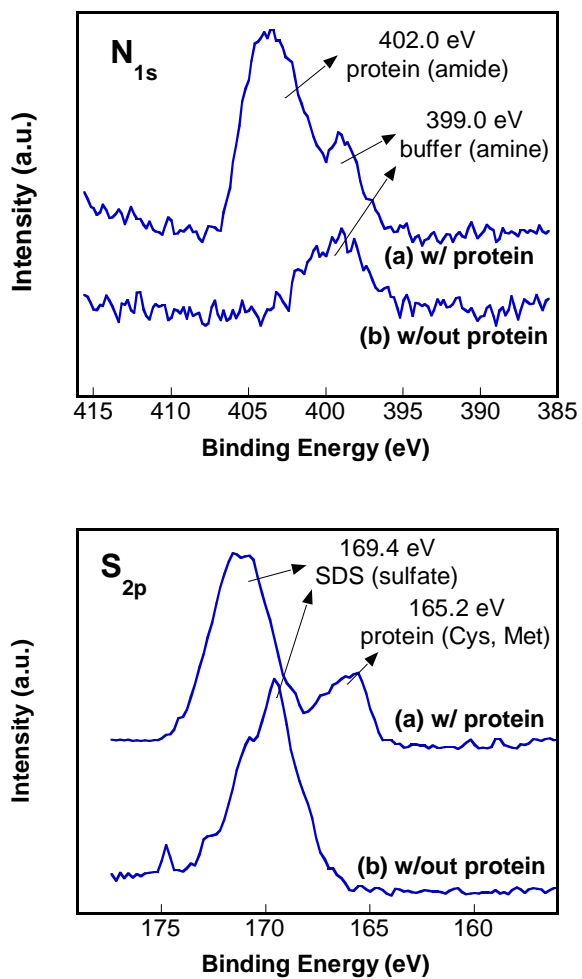


Figure 30. ESCA  $N_{1s}$  and  $S_{2p}$  spectra of the detection electrode surface: (a) with protein, and (b) without protein.

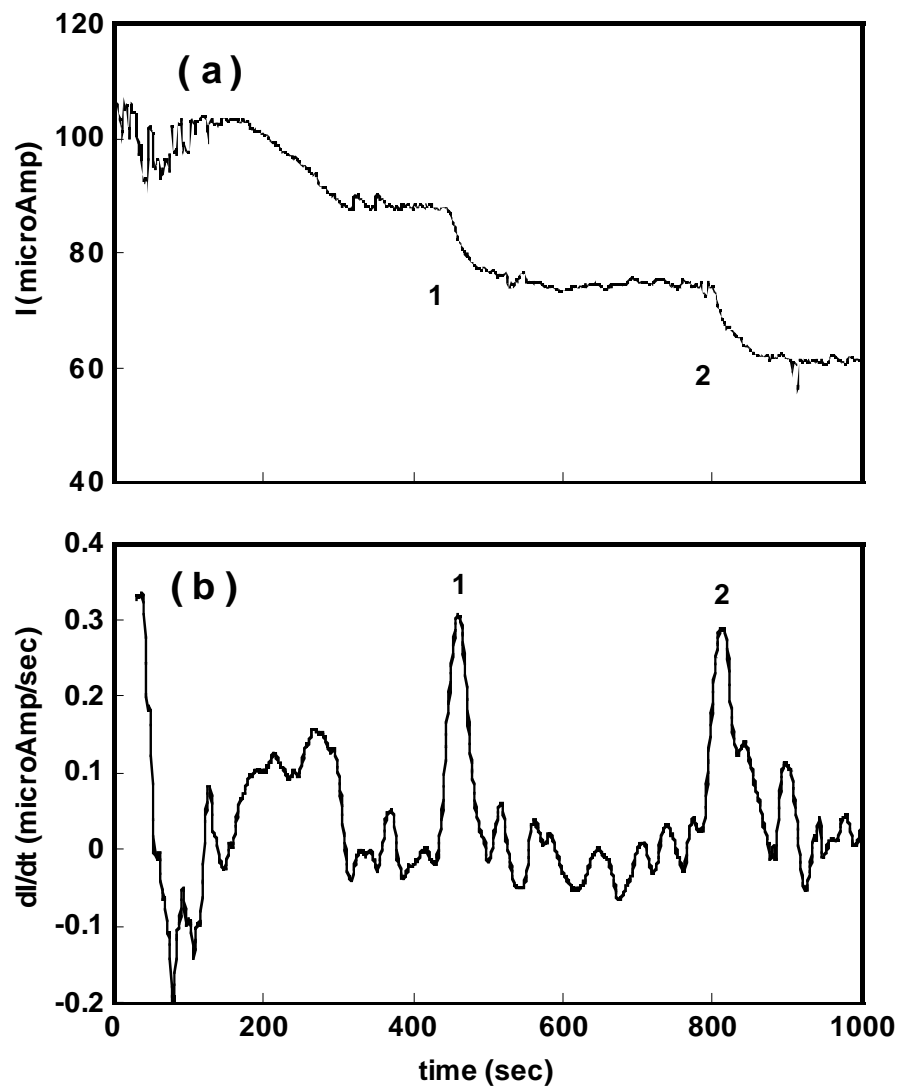


Figure 31. The microchannel's (a) current vs. time ( $I$ - $t$ ), and (b) ( $dI/dt$ ) vs.  $t$  curves replotted of current change with time ( $dI/dt$ - $t$ ) at different protein samples. The channel size has a depth of  $30.2\ \mu\text{m}$ , and a width of  $440\ \mu\text{m}$  at the bottom and  $530\ \mu\text{m}$  at the top. The channel is made of Si with sputtered  $\text{SiO}_x$  surface.

The electrical potential across the channel region was 11.8 V/cm, and 15.0% polyacrylamide gel was introduced into the channel. The solution (4  $\mu$ l) of carbonic anhydrase (29 kDa) and ovalbumin (45 kDa) were loaded in a sample reservoir at the concentrations of 325  $\mu$ g/ml, respectively. Figure 30(b) is the graph of the derivative of Fig. 30(a) curve with respect to time (t). The peak 1 represents the arrival of carbonic anhydrase (29 kDa) to the detection electrode, and the peak 2 represents the arrival of ovalbumin (45 kDa) to the detection electrode. At the beginning of the operation, *e.g.*,  $t < 150$  sec, the derivative of the current fluctuated severely. The same phenomenon was also observed in separate experiments. There are many possible causes of the fluctuations. For example, the system was not steady when the voltage was initially applied. There might be evaporation of the solution due to the sudden rise in temperature when the current was applied. The curve becomes smooth afterwards. There are two apparent current drops in the Fig. 30(a) curve, which correspond to the arrival times of the two separated proteins to the detection electrode.

The peak time of carbonic anhydrase was 459 seconds after electrophoresis, and that of ovalbumin was 811 seconds. Separately, we observed that the peak time of the same protein remains the same in spite of the absence of other proteins. Therefore, the mobility of a protein in this kind of device is constant, which indicates the effectiveness of the channel gel in separation of proteins. The effective migration speed (channel length divided by the peak time) of a protein decreases with the increase of its molecular weight. This is consistent with the result of the conventional slab-type or capillary

electrophoresis.<sup>2,3</sup> Therefore, the protein detection method of this device is as effective as the conventional optical detection method.<sup>9</sup>

Figure 32 shows the  $dI/dt-t$  curves measured from two different devices containing the same three proteins in the feed solution. Each protein ( $\alpha$ -lactalbumin (14.2 kDa), carbonic anhydrase (29 kDa), and ovalbumin (45 kDa)) has the same concentration of 325  $\mu\text{g/ml}$ . The device in Fig. 32(a) has a channel depth of 20.3  $\mu\text{m}$ , a width of 440  $\mu\text{m}$  at the bottom and 500  $\mu\text{m}$  at the top, and a length of 0.5 cm. The detection electrode area is  $3.0 \times 1.5 \text{ mm}^2$ . The device in Fig. 32(b) has a channel depth of 30.2  $\mu\text{m}$ , a width of 440  $\mu\text{m}$  at the bottom and 530  $\mu\text{m}$  at the top, and a length of 0.5 cm. The detection electrode area is  $1.4 \times 1.5 \text{ mm}^2$ .

The two devices have different channel cross-sectional areas and detection electrode areas. Fig 32(a) device has a channel depth of 20.3  $\mu\text{m}$  and detection electrode area of  $3.0 \times 1.5 \text{ mm}^2$ . Fig 32(b) device has a channel depth of 30.2  $\mu\text{m}$  and detection electrode area of  $1.4 \times 1.5 \text{ mm}^2$ . Obviously, the latter contains more distinct peaks than the former, *e.g.*, 0.3  $\mu\text{A/sec}$  *vs.* 0.05  $\mu\text{A/sec}$ . This is due to the shrinkage of the detection electrode size. The devices were made of Si substrate, whose channels were made by KOH etching. The surface of the Si-based device is sputtered  $\text{SiO}_x$ . The peak time ( $t_i$ ) of the same protein also differs in these two figures. This is due to factor such as the variation of the retention time in different channels.<sup>5-7</sup> Migration speeds of  $\alpha$ -lactalbumin (14.2 kDa), carbonic anhydrase (29 kDa), and ovalbumin (45 kDa) are estimated to be 5.8, 4.5, and 2.86 cm/hour, separately, in Fig. 32(a) and 5.4, 3.85, and 2.22 cm/hour, separately, in Fig. 32(b).

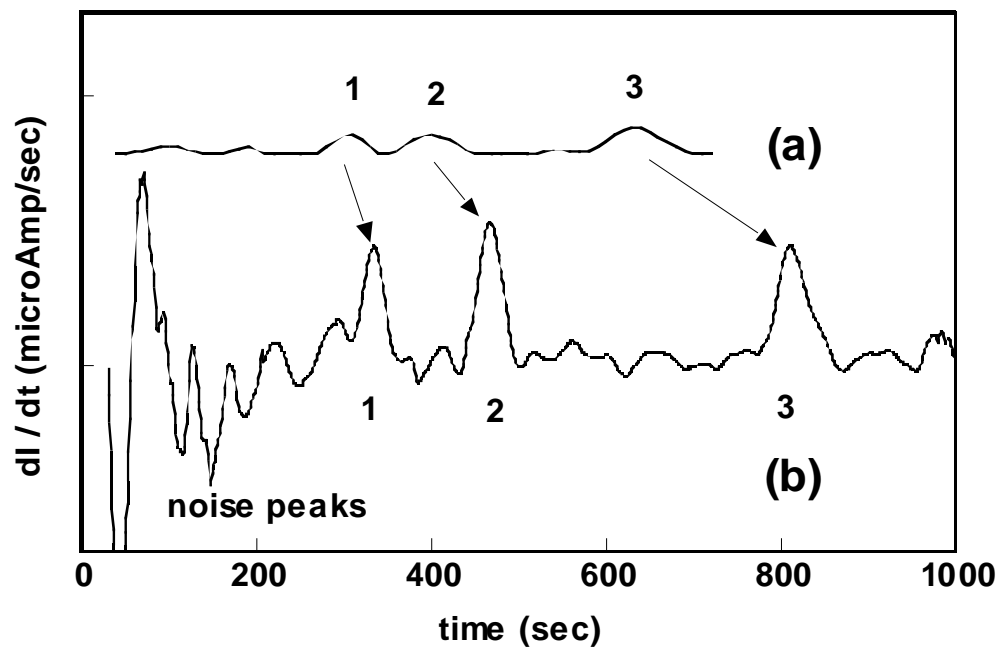


Figure 32. The  $dI/dt$  vs. run time ( $dI/dt-t$ ): (a) device with a channel depth of  $20.3 \mu\text{m}$  and detection electrode area of  $3.0 \times 1.5 \text{ mm}^2$ , (b) device with a channel depth of  $30.2 \mu\text{m}$  and detection electrode area of  $1.4 \times 1.5 \text{ mm}^2$ .

Figure 33 shows mobilities of proteins reported in a conventional slab-type SDS-PAGE<sup>1</sup> and measured from the two different microchannel devices described in Fig. 32. The protein mobility in the conventional slab-type were obtained from ref. 1; the mobilities of device (a) and device (b) were obtained from equations [2] and [3] in Chapter II. The migration of the protein in the microchannel device follows the linear relationship of  $\log(\text{mobility})$  vs. molecular weight. Mobilities of proteins in the microchannel device are higher than those in a typical slab-type electrophoresis.<sup>10</sup> The discrepancy may be due to factors such as the channel cross-sectional area, channel wall, materials. In spite of the same channel length (0.5 cm) in devices (a) and (b), device (b) has a larger cross-sectional area and a delayed peak time for the proteins. A similar result was reported for the separation of DNAs in a cross-junction type of device that contains hydroxyethyl cellulose (HEC) in the separation channel as sieving material.<sup>7</sup> In that case, the increase of the separation channel width from 30  $\mu\text{m}$  to 70  $\mu\text{m}$ , and the feed channel width from 30  $\mu\text{m}$  to 120  $\mu\text{m}$  resulted in doubling the separation time, but with almost 10 times improvement of detection sensitivity.<sup>7</sup> The increase of sensitivity and the delayed peak were due to the increase of DNA loading by the increase of feed channel width from 30  $\mu\text{m}$  to 120  $\mu\text{m}$ , and the dilution of the ionic strength in the large cross-sectional separation channel (width 70  $\mu\text{m}$ ). The dilution of the ionic strength in the separation channel comes from the lower ionic strength in the feed channel or reservoir.<sup>7,8</sup> The result of Fig. 33 shows that protein detection efficiency was improved by 6 times with the combining of two device configuration factors, *i.e.*, channel cross-sectional area and detection electrode area.<sup>6</sup>

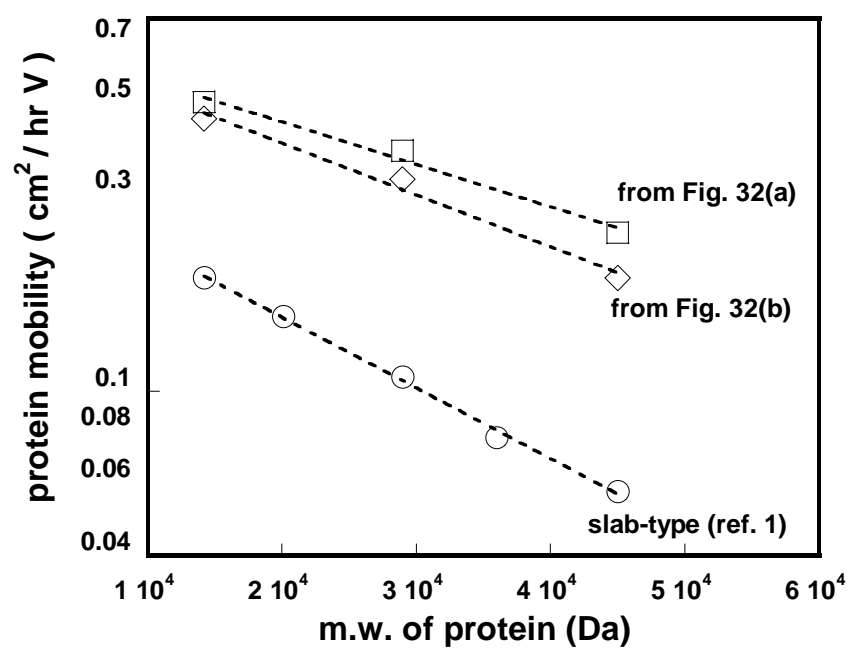


Figure 33. The protein mobility vs. the molecular weight of protein obtained from a conventional slab-type SDS-PAGE equipment (reference<sup>1</sup>), and from Fig. 32(a) and (b).



According to the literatures, the efficiency can be improved further with the same method, *i.e.*, changing the configurations of the microchannel.<sup>6,7</sup>

The gel composition or concentration in the microchannel region is critical for the separation efficiency. Low concentration (< 15.0%) of the gel could not achieve good separation or resolution. The theoretical number of plates ( $N$ ) and the resolutions ( $R$ ) for separation of  $\alpha$ -lactalbumin (14.2 kDa) from ovalbumin (45 kDa) were calculated from equations [27] and [28]. The result is shown in Table IX. All data were obtained with 15.0% polyacrylamide gel in the microchannel region.

$$N = 5.54 \times \left( \frac{t_i}{\Delta t_{1/2,i}} \right)^2 \quad [27]$$

$$R = 2 \times \frac{(t_1 - t_2)}{(\Delta t_{1/2,1} + \Delta t_{1/2,2})} \quad [28]$$

where  $t_i$  is the peak time of protein  $i$ , and  $\Delta t_{1/2}$  is the full width at the peak's half maximum.<sup>5</sup> For a good separator, both  $N$  and  $R$  numbers have to be large. The  $N$  values of device (b) are more than twice those of device (a). This indicates the improvement of device performance by changing the channel cross-sectional area and the detection electrode area. However, these numbers are still lower than those reported using a different type of microchannel device.<sup>5</sup> The low  $N$  is probably due to the band broadening, *i.e.*, the band curving in the polyacrylamide gel-filled microchannel.<sup>3</sup> The band curving is a very serious problem in the separation of DNA molecules in the polyacrylamide gel-filled channel.<sup>3</sup> However, in this study, the SDS was supposed to reduce the band curving due to the surfactant. The  $R$  values of device (b) are larger than those of device (a). They are larger than those of the conventional slab-type system.<sup>4,7</sup>

Table IX. Analysis of electrophoresis performance of device (a) and device (b) by theoretical plate (N) and resolution (R).

Device	Peak 1 (14.2 kDa)	Peak 2 (29 kDa)	Peak 3 (45 kDa)	Resolution ( R )		
	N ( $\times 10^3$ )	N ( $\times 10^3$ )	N ( $\times 10^3$ )	Peak 1,2	Peak 2,3	Peak 1,3
(a)	0.39	0.36	0.25	1.09	1.61	2.50
(b)	1.08	0.99	0.98	2.24	3.58	5.60

#### 1.4. Estimation of Adsorbed Proteins

Figure 34 shows I-t curves of the same device: (a) the feed solution containing no protein, (b) the feed solution containing three proteins, and (c) subtraction of (b) from (a). Three proteins ( $\alpha$ -lactalbumin, carbonic anhydrase, and ovalbumin) have the same concentration of 325  $\mu\text{g/ml}$ . The device has a channel depth of 30.2  $\mu\text{m}$ , width of 440  $\mu\text{m}$  at the bottom and 530  $\mu\text{m}$  at the top, and length of 0.5 cm. The detection electrode area is  $1.4 \times 1.5 \text{ mm}^2$ . The area of the three drastic current drops in Fig. 34(c) could be calculated by integrating the current (I) with respect to time (t, sec). The value could be used to estimate the charge density of adsorbed protein ( $Q_{ads}$ ) on the detection electrode.

From Fig. 34, it was calculated that  $Q_{ads}$  value is 474.5  $\mu\text{C}$  for  $\alpha$ -lactalbumin, 793.2  $\mu\text{C}$  for carbonic anhydrase, and 2554.9  $\mu\text{C}$  for ovalbumin. The electrode size is  $1.4 \times 1.5 \text{ mm}^2$  ( $0.021 \text{ cm}^2$ ). The surface protein concentration  $\Gamma$  can be calculated as below:

$$\Gamma = \frac{MQ_{ads}}{nF} \quad [29]$$

where  $M$  is the molecular weight,  $n$  is the total number of electrons transferred per protein molecule, and  $F$  is the Faraday constant.<sup>13,14</sup> Since each protein molecule carries a specific number of charges, the amount of protein adsorbed on the electrode surface could be calculated. It is generally recognized that, for 1.0 g of protein, 1.4 g of SDS can be adsorbed, and one SDS molecule carries two electrons from its sulfate group.<sup>2-4</sup> In recent studies, it was found that each carboxyl group in a protein molecule transfers two electrons to the metal surface.<sup>13,14</sup>

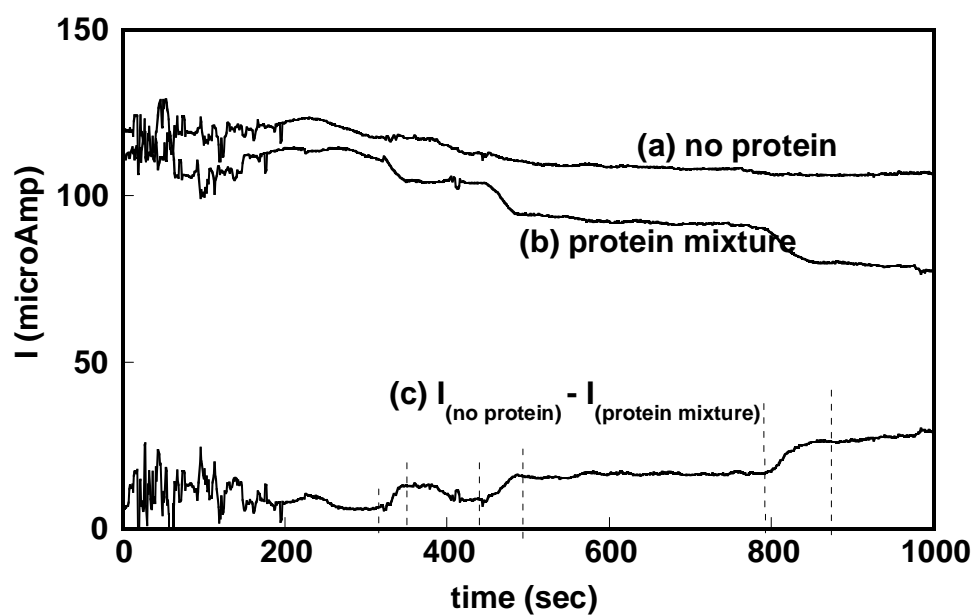


Figure 34. Current vs. gel run time (I-t): (a) the feed solution containing no protein, (b) the feed solution containing three proteins, (c) subtraction of (b) from (a).

If we assume that the above two factors determine the surface charge of the protein molecule in this study, equation [29] can be used for quantitative analysis. For an  $\alpha$ -lactalbumin molecule, there are 21 carboxyl groups<sup>13</sup> and 75 SDS molecules attached; for a carbonic anhydrase molecule, there are 27 carboxyl groups and 153 SDS molecules attached; for an ovalbumin molecule, there are 47 carboxyl groups and 238 SDS molecules attached.<sup>3</sup> From equation [29], 0.364  $\mu\text{g}$  of  $\alpha$ -lactalbumin was adsorbed on the electrode surface; 0.662  $\mu\text{g}$  of carbonic anhydrase was adsorbed; and 2.09  $\mu\text{g}$  of ovalbumin was adsorbed. For every experiment, 4  $\mu\text{l}$  of protein solution (325  $\mu\text{g}/\text{ml}$  for each protein concentration) was introduced into the feed reservoir. It corresponded to 1.3  $\mu\text{g}$  of each of the three proteins. Therefore, there are discrepancies between the calculated amounts and the actually loaded amounts. Since the calculation was based on many assumptions, as described previously, the deviation is not avoidable.

For  $\alpha$ -lactalbumin and carbonic anhydrase, the calculated amount was less than the actual amount. This is probably due to the loss of the protein in the electrophoresis process. Liu *et al.* reported the loss of protein in the microchannel electrophoresis experiment.<sup>7</sup> It was suggested that a high ionic strength buffer solution could be used to solve the problem. However, for the interpretation of our data, there are different considerations. In our device, there are other factors contributing to the loss of protein. For example, the channel wall of our device contains two types of materials, *i.e.*,  $\text{SiO}_x$  and cellulose tape. Due to the electrostatic interaction, protein adsorption on these materials could be very serious.<sup>7</sup>

The  $\alpha$ -lactalbumin, carbonic anhydrase, and ovalbumin were loaded in 4  $\mu$ l sample reservoir at the concentrations of 325  $\mu$ g/ml, respectively. The protein-free buffer solution was used separately in a control experiment. In this experiment, a very low electric field was applied, *i.e.*, 11.8 V/cm, while other microchannel devices reported in the literature often operated at a high field, *e.g.*, 600 V/cm.<sup>5</sup> The charge of the channel wall can increase with increase of the field strength. The charged channel wall usually forms a undesirable electro-osmotic flow.<sup>3,7,8</sup> The electro-osmotic flow has a flow direction counter to the direction of electrophoresis flow, which reduces the efficiency of the electrophoresis.

## 2. Microchannel Surface Electrophoresis for DNA Analysis

For large-sized DNA separation, the conventional gel electrophoresis system is not applicable due to the size restriction of DNA molecules.<sup>19</sup> Surface electrophoresis will be a good substitute for the gel-filled microchannel electrophoresis. The surface electrophoresis device has the same configuration as the microchannel device used to separate proteins, except there is no gel in the bottom channel surface region.

If a change of the detection electrode contact resistance is detected upon the arrival of the separated DNA fragment, the mobility can be calculated. Since the DNA fragment migrates along the bottom surface of the channel, we could influence the separation efficiency by modifying it.

## 2.1. DNA Electrophoresis on Solid Surface

Most literature reports of surface electrophoresis experiments were performed on the unpatterned silicon wafer without a defined channel area for DNA migration.<sup>12,13</sup> However, if the surface electrophoresis is carried out in a three-dimensional microchannel structure, the current flow and the transport of the DNA fragments can be forced into a confined region.

Figure 35 shows (a) a schematic setup of electrophoresis on a completed microchannel device, and (b) a photograph of UV-lighted  $\lambda$ -EcoR I digest DNA sample attached with the ethidium bromide fluorescent agent. The air-dried DNA sample in the feed reservoir could stay on the bottom surface for a long time after the application of the buffer solution to the system. For example, the DNA fluorescent spot in Fig. 35(b) lasted for more than five minutes before an electric field was applied.

Figure 36 shows the binding energies of  $N_{1s}$  and  $P_{2p}$  for two detection electrode surfaces after electrophoresis in  $0.5\times$  TBE with or without DNA component. The lower curve of Fig. 36(a) contains a  $N_{1s}$  peak at 399.6 eV that corresponds to the amine ( $-NH_2$ ) group contributed by the tris-borate and EDTA components in the buffer solution. The upper curve of Fig. 36(a) contains an additional  $N_{1s}$  peak at 401.0 eV that corresponds to the purine and pyrimidine groups of DNA nucleotides, such as adenine, guanine, cytosine, and thymine. Separately, the lower curve of Fig. 36(b) does not show a phosphate peak. However, the upper curve of Fig. 36(b) contains two  $P_{2p}$  peaks at 132.4 eV and 133.1 eV, which correspond to the phosphate group in the DNA backbone. These additional N and P groups are common in DNA molecules.

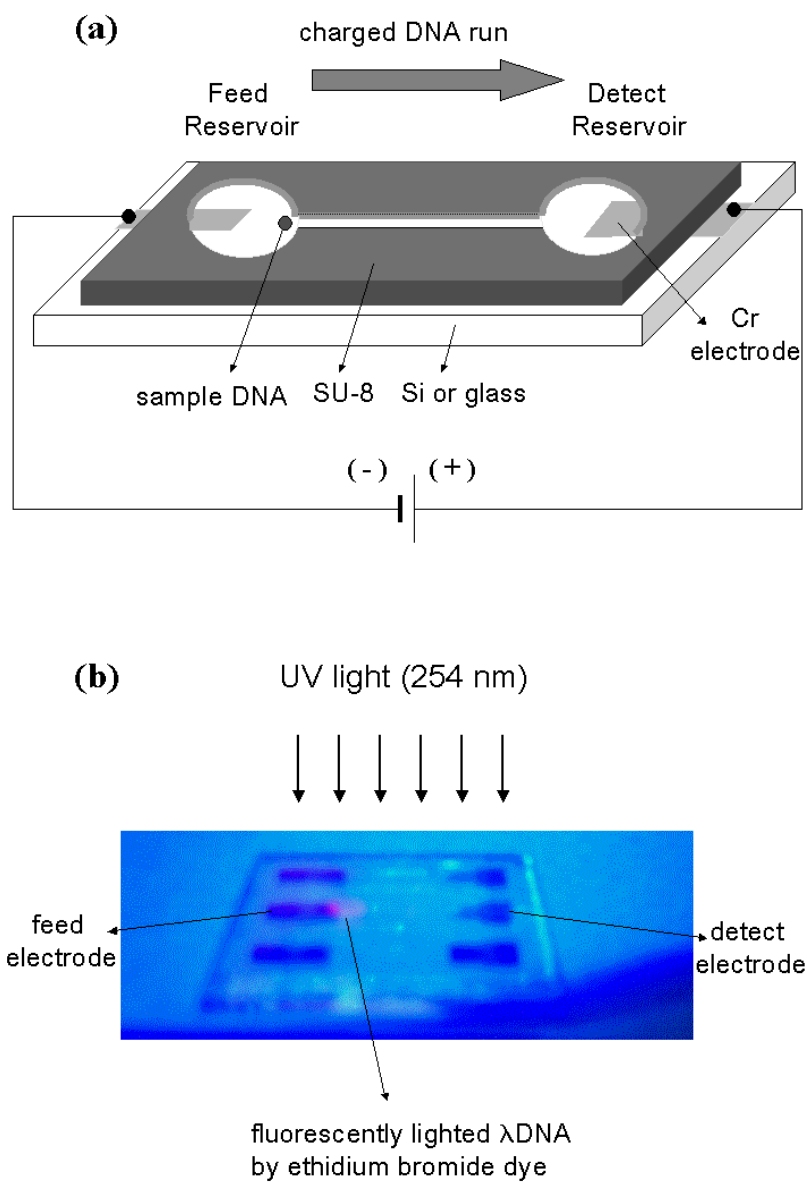


Figure 35. (a) Schematic setup of electrophoresis on a completed microchannel device, and (b) photograph of UV exposed  $\lambda$ -EcoR I digest DNA sample attached with the ethidium bromide fluorescent agent.



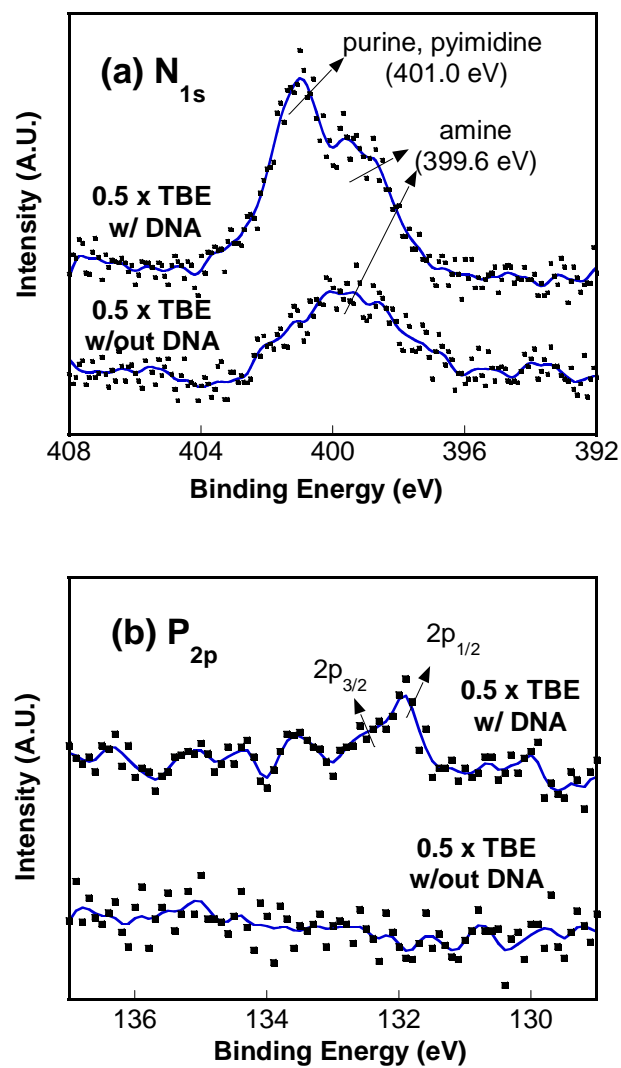


Figure 36. ESCA spectra of the detection electrode surface: (a)  $N_{1s}$  and (b)  $P_{2p}$ .

Therefore, it is clear that DNA was transported from the feed reservoir to the detection electrode surface by the electrophoresis process. This result is similar to the previous reports of protein separation by a polyacrylamide gel-filled electrophoresis device.<sup>10,11</sup> In the latter cases, the N<sub>1s</sub> peak of the amide bond (-NHCO-) and S<sub>2p</sub> peak of the thiol group (-SH) of the protein molecules were presented.

Figure 37 shows curves of the current change rate *vs.* time (dI/dt-t) of two microchannel surface electrophoresis devices with different channel bottom surfaces. The channel was made of a SU-8 sidewall and glass or Si bottom surface with a depth of 35 μm, width of 485 μm, and length of 0.5 cm, as previously shown in Fig. 14 of Chapter III. The six fragments of the λDNA (3.5, 4.9, 5.6, 5.8, 7.4, and 21.2 kbp) correspond to six individual peaks in the graph. The mobility for each DNA fragment can be calculated as described in equation [3] of Chapter II. At the early stage of the electrophoresis, the current fluctuation was observed. This is caused by the fast arrival of the DNA not adsorbed to the bottom surface of the channel, which was reported in Seo, *et al.*<sup>19</sup>

When the two graphs in Fig. 36 are compared, signals from the oxidized Si channel are stronger than those from the oxidized glass channel. In addition, DNA fragments moved more quickly on an oxidized glass surface than on an oxidized Si surface. This result is consistent with the contact angle measurement, *i.e.*, the DNA solution has a lower contact angle on the oxidized Si than on the oxidized glass, as discussed in Chapter IV. The mobility of the DNA fragment is determined by its affinity to the channel's bottom surface.

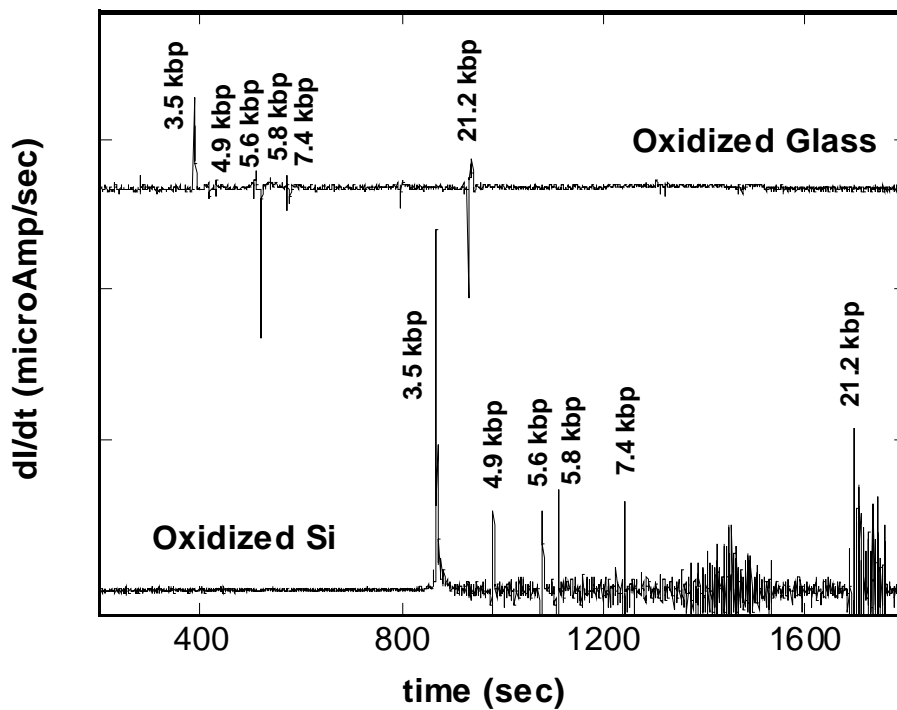


Figure 37. The  $dI/dt-t$  for electrophoresis of  $\lambda$ -EcoR I digest DNA fragments on glass and Si microchannels. The channel was made of SU-8 sidewall and glass or Si bottom surface with depth of  $35\ \mu\text{m}$ , width of  $485\ \mu\text{m}$ , and length of  $0.5\ \text{cm}$ .

If the large fragment contains more surface-affinity groups than the small fragment, it will be adsorbed much more strongly, and will arrive at the detection electrode in a lower rate. In addition, the mobility of the same fragment on the strongly adsorbed surface, *i.e.*, oxidized Si, is smaller than that on the weakly adsorbed surface, *i.e.*, oxidized glass.

Figure 38 shows the relationship between the number of base pairs ( $N$ , bp) in the DNA fragment and the mobility ( $\mu$ ). It is in the log-log scale. The relationship between the mobility and the size of the fragment ( $N$ ) can be expressed as below:

$$\mu = \mu_o N^{-\alpha} \quad [30]$$

where  $\mu_o$  is the mobility at  $N=1$  and  $\alpha$  is the dispersion value. The value of  $\alpha$  is influenced by the solution property, such as ionic strength, the electric field strength, and the structure of the channel's bottom surface. For the oxidized Si channel,  $\alpha$  is 0.37 as shown in Fig. 38(a) data, which is close to the literature report of 0.25.<sup>19,20</sup> For the oxidized glass channel,  $\alpha$  is 0.49 as shown in Fig. 38(b). In a slab-agarose gel electrophoresis system,  $\alpha$  is 0.87.<sup>2</sup> Therefore, the dispersion of mobility in Fig. 38 devices is much less than that of a slab-agarose gel electrophoresis, which indicates the resolutions of the slab-agarose gel among the different sized DNA fragments are better than those of the oxidized glass and Si microchannel devices. However, the two microchannel devices in Fig. 38 can separate very large sized DNA fragments. Because of its low mobility, the conventional agarose gel electrophoresis cannot be used to pass the large DNA fragment, *i.e.*, 21.2 kbp in the EcoR I-digested  $\lambda$ DNA, through the entire microchannel.<sup>2,19</sup>

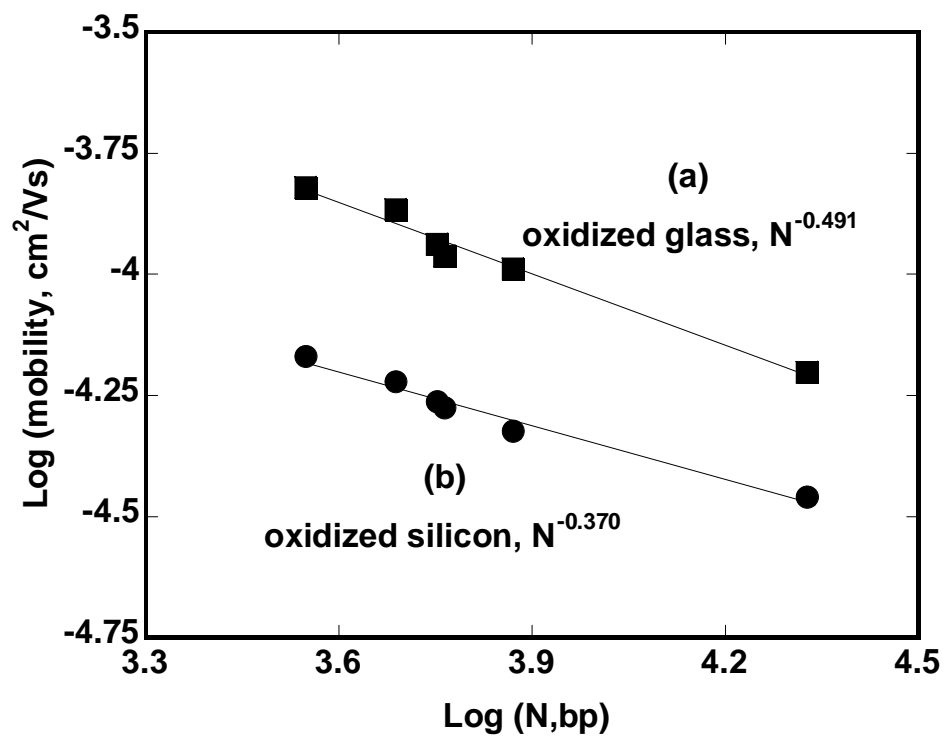


Figure 38. Log scale of mobility vs. log scale of No. basepair of  $\lambda$ -EcoR I digest DNA fragments on (a) oxidized glass surface, and (b) oxidized Si surface microchannel.

## 2.2. Substrate and Buffer Effects on DNA Mobility

Figure 39 shows the surface chemical property of the characteristics of the electrophoresis device. These entire devices were untreated,  $\text{H}_2\text{O}/\text{H}_2\text{O}_2/\text{H}_2\text{SO}_4$  solution-oxidized, and  $\text{H}_2$  plasma-treated. The channel was made of a SU-8 sidewall and Si bottom surface with a depth of 35  $\mu\text{m}$ , width of 485  $\mu\text{m}$ , and length of 0.5 cm. The data was obtained using a buffer solution without DNA. The electrical current of the device with the oxidized Si bottom surface is larger than that with the untreated Si surface, which is further larger than that with the hydrogenated Si surface. Since the entire microchannel device contains three different materials, *i.e.*, bottom channel surface, SU-8 sidewall, and Cr electrodes, all of them can influence the overall current passing through the device. It is difficult to differentiate the contribution of individual factors. However, the influence of the channel bottom surface to the current is obvious from the data in Fig. 39. For example, the oxidized group, *e.g.*, SiO (with the Si-O binding energy of 102.0 eV) and  $\text{SiO}_2$  (with the Si-O binding energy of 103.3 eV) shown in Chapter IV, enhances the electrical conductivity along the surface.<sup>44,45</sup>

Since the hydrogenation process lowers the hydrophilicity of the Si or glass surface, the SU-8 surface became an important current path in the device. On the other hand, if the SU-8 surface is very hydrophobic, it cannot be a major current path in the device. The surface structure of a polymer, such as a SU-8, can be very complicated. Even though the hydrogenated SU-8 channel sidewall is loaded with rather hydrophilic groups, the proportion of electrical current through the solution and the SU-8 interface appears to be small, as shown in Fig. 39.

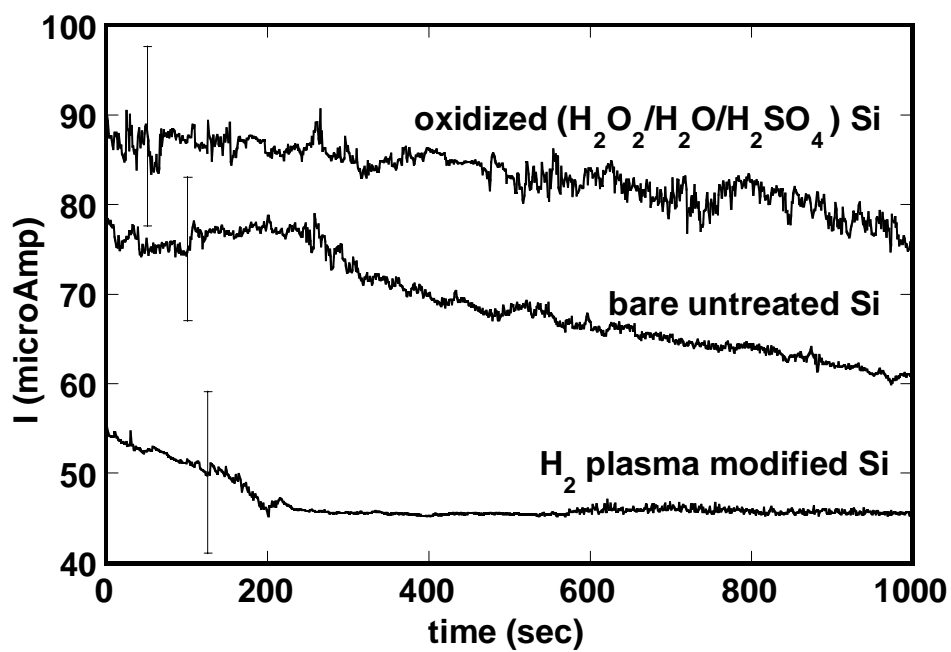


Figure 39. Current vs. time (I-t) with the buffer solution not loaded with DNA. The channels were made of SU-8 sidewall and Si bottom surface with a depth of 35  $\mu\text{m}$ , width of 485  $\mu\text{m}$ , and length of 0.5 cm as untreated,  $H_2O/H_2O_2/H_2SO_4$  oxidized, and  $H_2$  plasma-treated.

According to Doherty *et al.*'s report, polymeric wall coating is often used in an electrophoresis system.<sup>44</sup> The polymer is coated as a thin film layer on a rather hydrophilic glass or silica to eliminate electro-osmotic flow, or to remove shear from the charged surface under an electric field.<sup>44,46</sup> In addition, the H<sub>2</sub>O/H<sub>2</sub>O<sub>2</sub>/H<sub>2</sub>SO<sub>4</sub> oxidized SU-8 surface does not show significant chemical structure change as shown in C<sub>1s</sub> ESCA spectra of Fig. 21(b) of Chapter IV. The resistance to current flow through the interface of the oxidized SU-8 and the solution is a little different from that of the interface of hydrogenated SU-8. Therefore, for the SU-8-formed channel, the structure of the bottom channel surface is critical to the total current through the device. In addition, when the polymer surface becomes somewhat hydrophilic, it is reported that the polymer surface adversely inhibits the current flow by mechanism such as charge trapping flow.<sup>44,46</sup>

Figure 40 shows the current vs. time (I-t) curves of DNA surface electrophoresis with different buffer concentrations (0.1×, 0.5×, 1.0×, 2.0×, and 5.0× TBE). The channel was made of a SU-8 sidewall and Si bottom surface. The entire device was (a) H<sub>2</sub>O/H<sub>2</sub>O<sub>2</sub>/H<sub>2</sub>SO<sub>4</sub> solution-oxidized or (b) H<sub>2</sub> plasma-treated. Fig. 40(a) shows that the 2.0× or 5.0× TBE buffer solutions do not have drastic current drops, which shows that no DNA separation occurs in the high buffer concentration using the oxidized device. In Fig. 40(b), the H<sub>2</sub> plasma-treated devices have only one drastic current drop for each buffer concentration, which indicates that it is impossible to separate DNA fragments larger than 3.5 kbp using the H<sub>2</sub> plasma-treated device. The time of the drastic current drop for each buffer concentration increases with the increase of buffer concentration on the H<sub>2</sub> plasma-treated device.



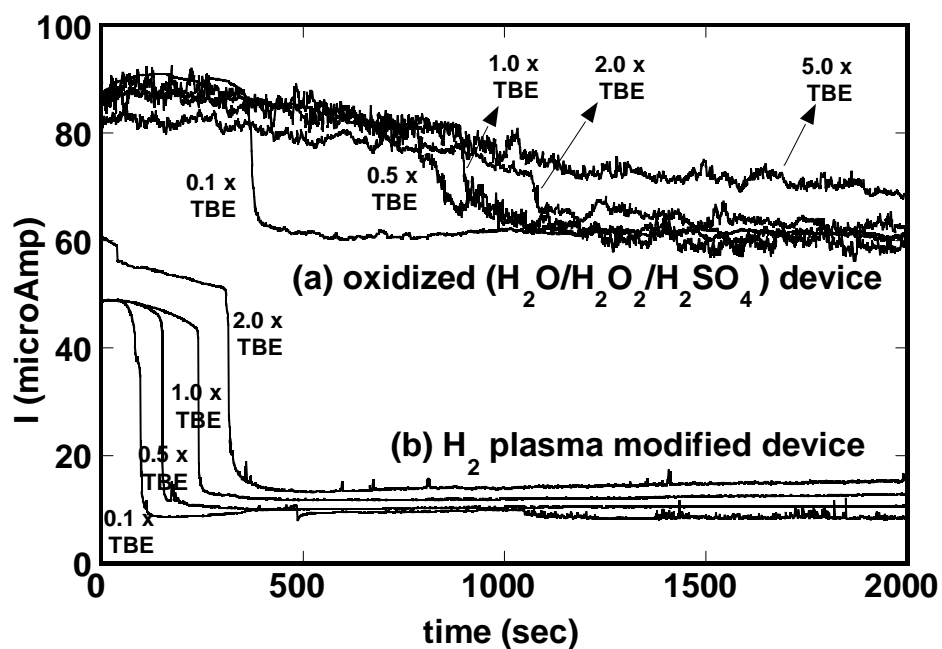


Figure 40. The current vs. time (I-t) curves of DNA surface electrophoresis with different buffer concentration (0.1 $\times$ , 0.5 $\times$ , 1.0 $\times$ , 2.0 $\times$ , and 5.0 $\times$  TBE). The channel was made of a SU-8 sidewall and Si bottom surface with a depth of 35  $\mu$ m, width of 485  $\mu$ m, and length of 0.5 cm. The entire Si wafer devices were (a)  $H_2O/H_2O_2/H_2SO_4$  solution-oxidized or (b)  $H_2$  plasma-treated.

Figure 41 shows the graphs of the derivative of Fig. 40 with respect to time ( $t$ ). The peaks corresponding to the 3.5 kbp DNA fragment were labeled. Other peaks for 4.9, 5.6, 5.8, 7.4, and 21.2 kbp DNA fragments were not labeled. The channel was either (a) solution-oxidized or (b) H<sub>2</sub> plasma-treated. The migration of the 3.5 kbp on the oxidized surface is slower than that on the hydrogenated surface. This is consistent with the result in Fig. 39, although the latter does not contain DNA. Fig. 41 shows that the migration speed of the 3.5 kbp fragment decreases with the decrease of the buffer concentration.

Figure 42 shows the mobility of the shortest DNA fragment (3.5 kbp) obtained from Fig. 41 vs. concentration of the buffer solution. For both curves in Fig. 42, the DNA mobility decreases with the increase of the buffer concentration. It was reported that under the high buffer concentration condition, the DNA fragments are surrounded with an ionic layer, which helps their adhesion to the solid surface.<sup>20</sup> However, when the buffer concentration was too high, *e.g.*, 2.0× and 5.0× TBE in this study, there was no obvious  $dI/dt$  peak in the operation curve. This is probably due to the formation of a layer surrounding the detection electrode, which reduced the sensitivity of the detection electrode. Therefore, for the optimal performance of this kind of microchannel device, the 0.5× or 1.0× TBE buffer solution is suitable.

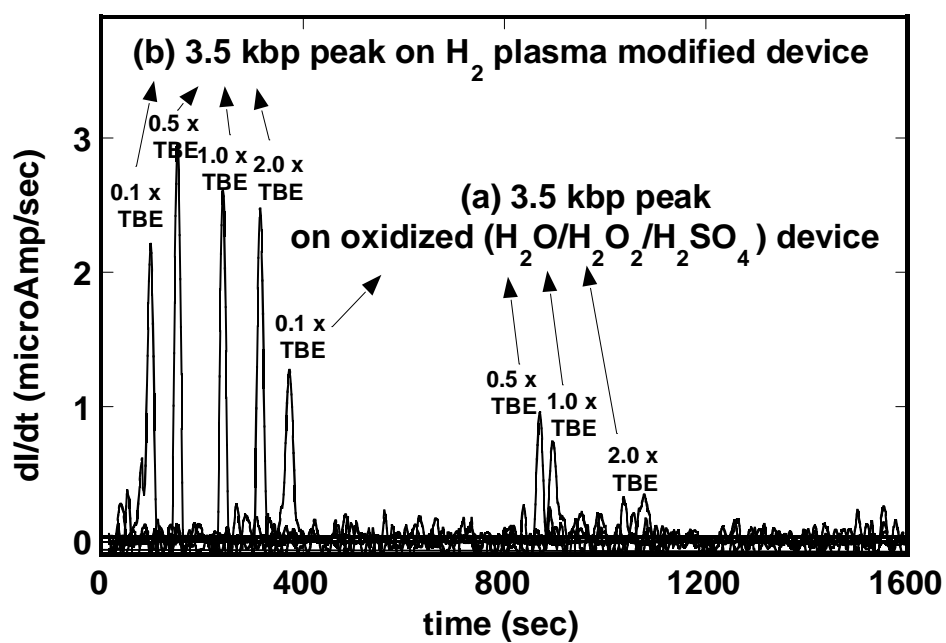


Figure 41. The  $dI/dt$ - $t$  curves of a microchannel surface electrophoresis on (a) oxidized and (b) H<sub>2</sub> plasma-treated microchannels with SU-8 sidewall and Si bottom surface in 0.1 $\times$ , 0.5 $\times$ , 1.0 $\times$  and 2.0 $\times$  TBE buffer.

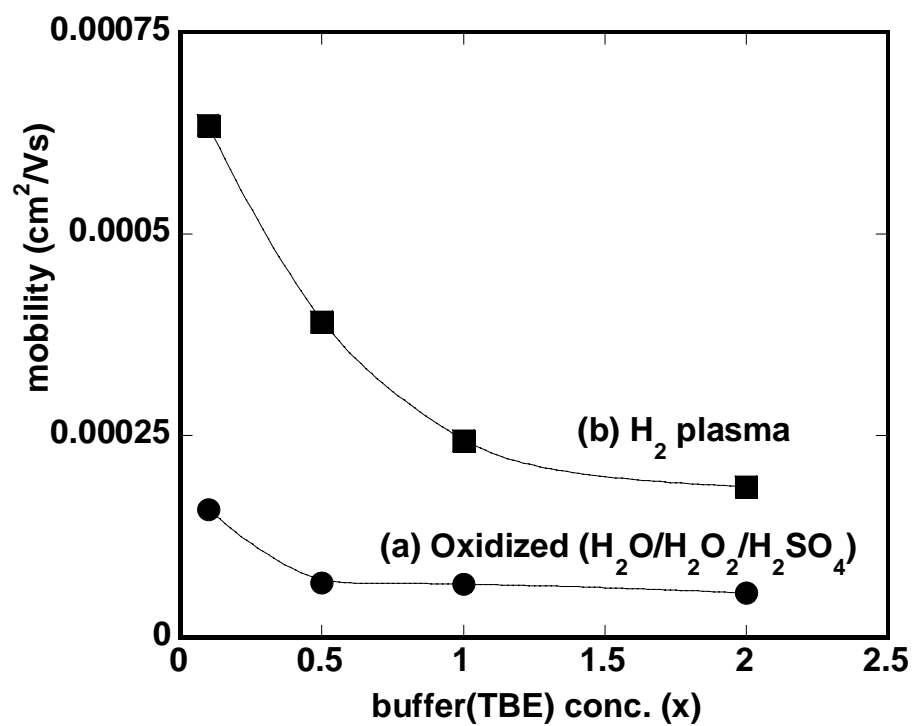


Figure 42. Mobility of 3.5 kbp fragment of  $\lambda$ -EcoR I digest DNA vs. buffer concentration on (a) oxidized and (b)  $\text{H}_2$  plasma-treated microchannels.

## CHAPTER VI

## THIN FILM TRANSISTOR DRIVEN ELECTROPHORESIS\*

1. Characteristics of PECVD SiN<sub>x</sub>

Deposition rate of PECVD SiN<sub>x</sub> is a function of substrate temperature and plasma power. The deposition rate is known to increase or decrease with the plasma power at a fixed substrate temperature.<sup>24</sup> The temperature and plasma power also influence refractive index (RI) of the deposited film. At a fixed power, the RI increases with the increase of the substrate temperature. The increase of the RI with the temperature comes from the change of the chemical structure or film densification.<sup>28,29</sup> When the temperature is fixed, the RI decreases with the increase of the plasma power.

Figure 43 shows the deposition rate of SiN<sub>x</sub> as a function of the substrate temperature at different plasma powers. All experiments were performed with the same feed gases (SiH<sub>4</sub>/NH<sub>3</sub>/N<sub>2</sub> 40/120/720 sccm) and pressure (500 mTorr). Two conclusions can be drawn from the figure: (i) the deposition rate decreases with the substrate temperature, and (ii) the deposition rate increases with power. Since plasma phase chemistry is independent of the substrate temperature, the change of the deposition rate (under the same plasma power) must be due to the surface reaction. At a high temperature, reactive species such as radicals migrate easily at the substrate surface.

---

\* Part of this chapter is reprinted with permission from “Plasma-Enhanced Chemical Vapor Deposition of Silicon Nitride below 250°C” by Y. Kuo and H.H. Lee, 2002, *Vacuum*, 4, 299-303, 2004 by Elsevier LTD.

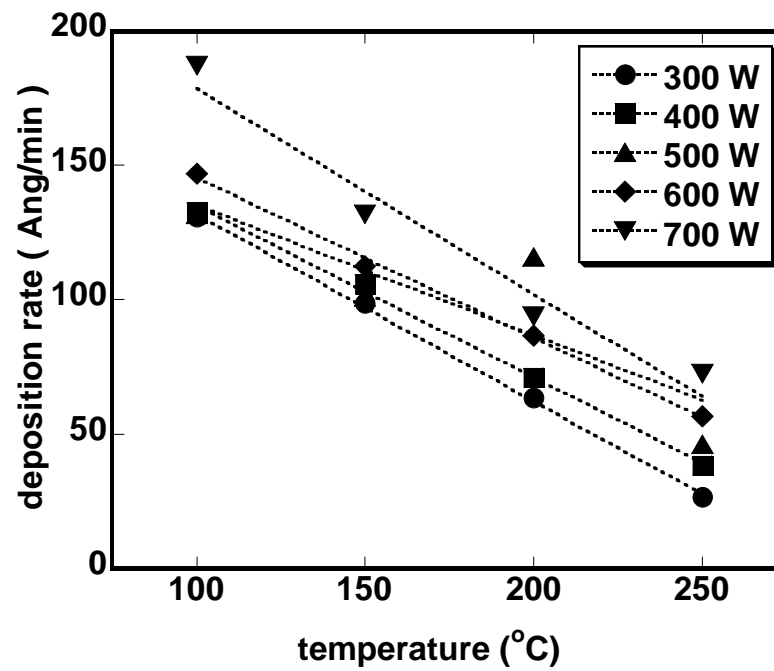


Figure 43. PECVD SiN<sub>x</sub> deposition rate as a function of temperature at various plasma powers.

At a low surface temperature, the reactive species do not have enough energy to migrate. In the PECVD process, free radicals generated in the plasma-phase are transported and adsorbed on the substrate surface. These radicals form the film through mechanisms of migration, reaction, and side-product desorption. Surface reactions are complicated. For example, new bonds can be formed and remain on the surface, which favors the deposition rate. Surface groups can be etched off by hydrogen radicals, which decrease the deposition rate. These reactions are far from stoichiometric. The formed film contains many defects. As the substrate temperature is increased, the film is densified, which also lowers the film's deposition rate. This explains why the deposition rate of low temperature is higher than that of high temperature.<sup>24</sup>

Figure 44 shows the substrate temperature and plasma power influences on the RI of the deposited  $\text{SiN}_x$  film. At a fixed power, the RI increases with the increase of the substrate temperature. When the temperature is fixed, the film's RI decreases with the increase of the plasma power. The change of the RI with temperature can be from the change of chemical structure of the film, which can be verified by surface analysis.

Fourier Transformed Infrared (FT-IR) spectroscopy is often used to analyze chemical bonding information of solid-state films. Figure 45(a) shows FT-IR spectra of  $\text{SiN}_x$  films deposited at different temperatures with the plasma power fixed at 700 W. Four major peaks, *i.e.*, N-H stretch ( $\sim 3350 \text{ cm}^{-1}$ ), Si-H stretch ( $\sim 2190 \text{ cm}^{-1}$ ), N-H bend ( $\sim 1170 \text{ cm}^{-1}$ ), and Si-N stretch ( $\sim 840 \text{ cm}^{-1}$ ), are clearly detected in each film. Two conclusions can be drawn: (i) the N-H stretching and bending peaks decrease with the increase of the temperature, and (ii) the Si-H stretch peak follows the opposite trend.

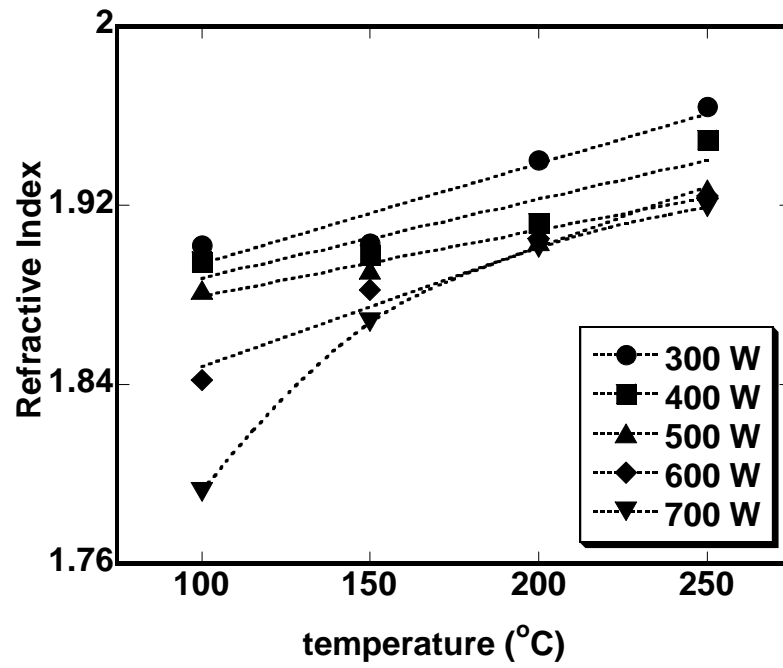


Figure 44. PECVD SiN<sub>x</sub> refractive indices as a function of temperature at various plasma powers.



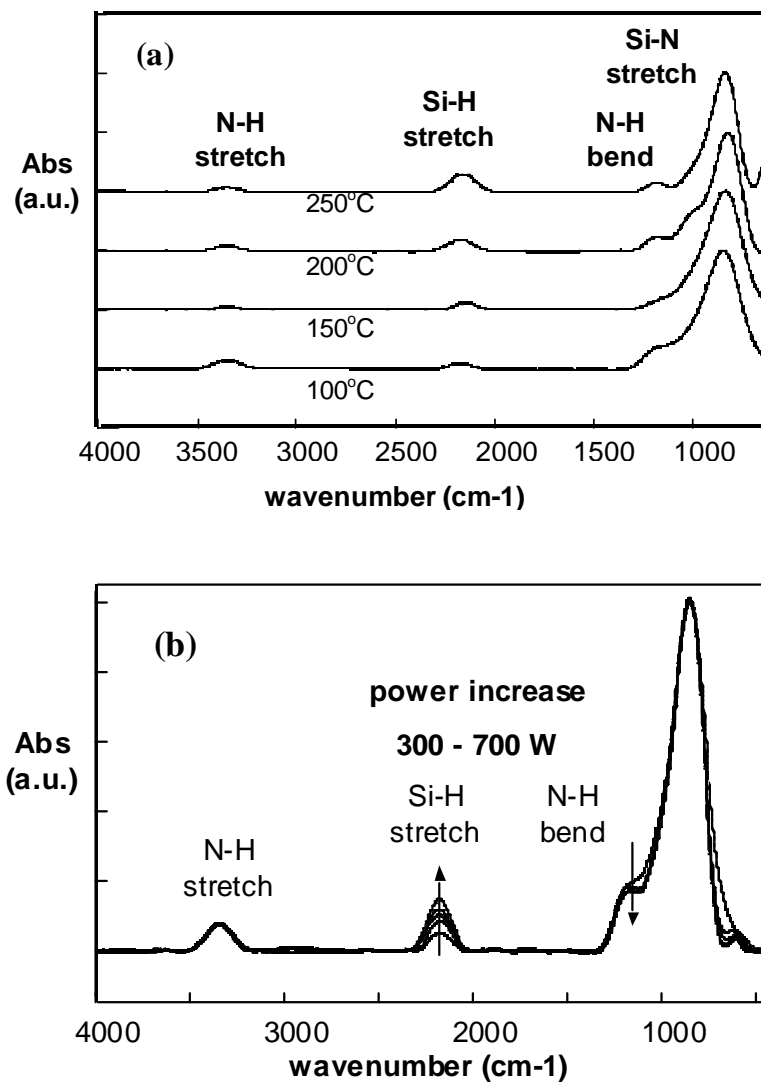


Figure 45. FT-IR spectra of PECVD  $\text{SiN}_x$  films: (a) at 100°C, 150°C, 200°C and 250°C with 700 W rf power, and (b) comparison of characteristic peaks of 100 °C  $\text{SiN}_x$  films with various rf powers.

Then, the N-H/Si-H ratio, which is the area ratio of the N-H stretch peak ( $\sim 3350\text{ cm}^{-1}$ ) / the Si-H stretch peak ( $\sim 2190\text{ cm}^{-1}$ ), decreases with the increase of temperature. The 250°C-deposited film has a wider Si-H stretch peak than the N-H stretch peak, which is opposite to that reported in the literature.<sup>28,29,47</sup> This is probably due to the difference in the rf frequency, *i.e.*, 50 kHz in this work and 13.56 MHz in others' work.<sup>17,29,48</sup> Fig. 45(b) shows that the size of the N-H stretch peak is almost independent of the plasma power at 100°C. The size of the Si-H peak increases with the increase of the plasma power. The FT-IR of the 100°C-deposited film remains the same even after being exposed to air for several months. This indicates that the bulk of the film is stable, *e.g.*, the room temperature oxidation is limited to the surface layer.<sup>25</sup> It was observed that the relationships discussed in Fig. 45(a) and (b) were consistent over large ranges of substrate temperature and plasma power. In addition, the influence of the plasma power to the film structure, *e.g.*, the (N-H /Si-H) ratio at 100°C, is more pronounced than that at 250°C.

Figure 46 shows ESCA spectra of Si<sub>2p</sub> of SiN<sub>x</sub> films deposited under various temperatures at 500 W. Each spectrum could be fitted into three peaks, *i.e.*, Si-N (101.8 eV), Si-O(N) (102.8 eV), and Si-O (103.6 eV). The last two peaks were formed from unpassivated Si bonds during the exposure to air. The (Si-O+Si-O(N) / Si-N) peak ratio (0.52, 0.32, and 0.31 for 100°C, 150°C, and 250°C, respectively) decreases with the increase of the substrate temperature. Therefore, the high temperature-deposited film is more stable and contains less unsaturated Si bonds than the low temperature-deposited film.

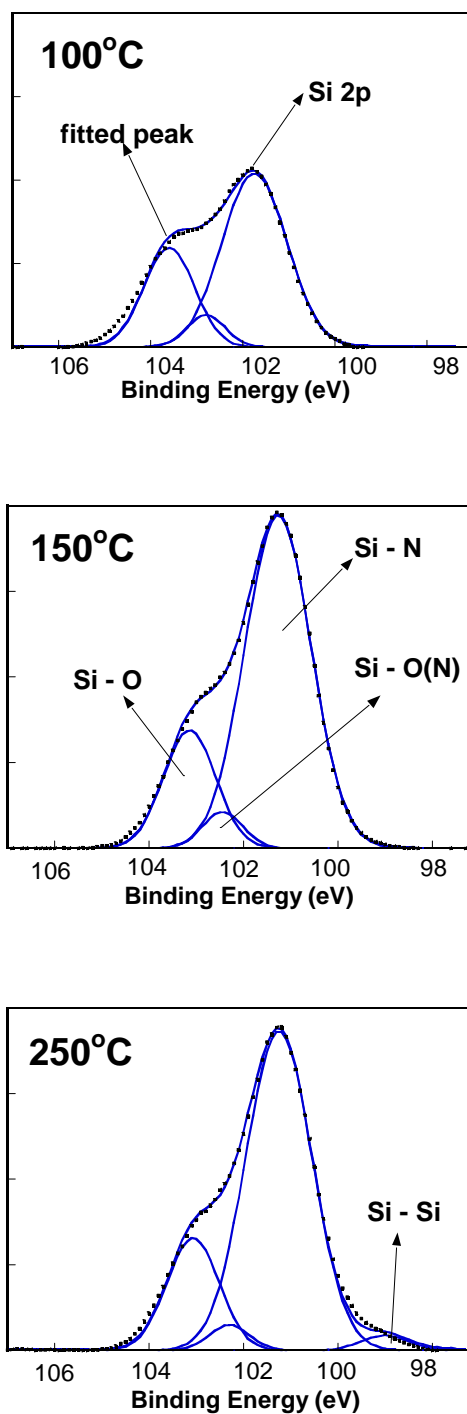


Figure 46. ESCA spectra of Si<sub>2p</sub> peak of SiN<sub>x</sub> films: at 100°C, 150°C, and 250°C with 500 W.

At 250°C, the Si-Si bond peak (99.5 eV) is detected. The Si-Si bond is probably responsible for the RI of the high temperature-deposited SiN<sub>x</sub> as shown in Fig. 44.<sup>24</sup>

Table X shows the FT-IR (N-H stretch/Si-H stretch) peak ratio and ESCA N/Si atomic ratio of SiN<sub>x</sub> films as a function of the plasma power. Both ratios decrease with the increase of the plasma power. In addition, when the two ratios are plotted with respect to the rf power, they show a linear relationship. There can be two interpretations: (i) the increase of power produces more reactive Si-H radicals rather than N-H radicals in the plasma phase, or (ii) the high power makes it easy to selectively remove the N-H component from the film surface due to the hydrogen etching mechanism. Although it is difficult to detect the hydrogen concentration change in the plasma phase, the hydrogen etching mechanism is widely accepted.<sup>28,29</sup> It was indirectly proven by analyzing the easiness of oxidation of the deposited film.

Figure 47 shows the wet etch rate of SiN<sub>x</sub> film in a diluted HF solution (1:20 HF/DI water) with respect to the film's RI. The 100°C-deposited films have low refractive indices and high etch rates. This is consistent with the literature's report that a low refractive index film has a weak chemical resistance as commonly reported, and the low temperature film has a less dense structure than a high temperature one.<sup>16,18</sup> The relationship between the wet etch rate and the refractive index of SiN<sub>x</sub> is useful for the a-Si:H TFT fabrication.

Figure 48 shows the I-V characteristics of metal-insulator-silicon (MIS, Al-SiN<sub>x</sub>-Si wafer) structures. The 100°C-deposited film has a high leakage current of  $2.19 \times 10^{-8}$  Amp/cm<sup>2</sup> at 2.0MV/cm, which is improper for the TFT gate dielectric application.

---

Table X. FT-IR N-H/Si-H peak ratio and ESCA atomic N/Si ratio of SiN<sub>x</sub> as a function of plasma power.

Power	FT-IR (N-H/Si-H) peak ratio	ESCA atomic N/Si ratio
300 W	1.132	0.745
400 W	1.123	0.703
500 W	0.873	0.675
600 W	0.752	0.657
700 W	0.539	0.638

---

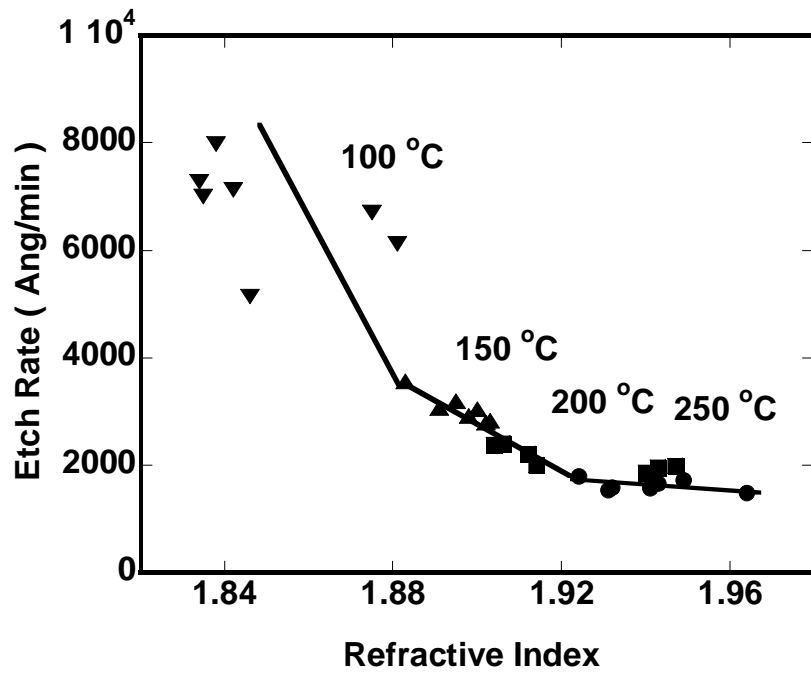


Figure 47. Etch rate profile with various refractive index films from 100°C, 150°C, 200°C, and 250°C.

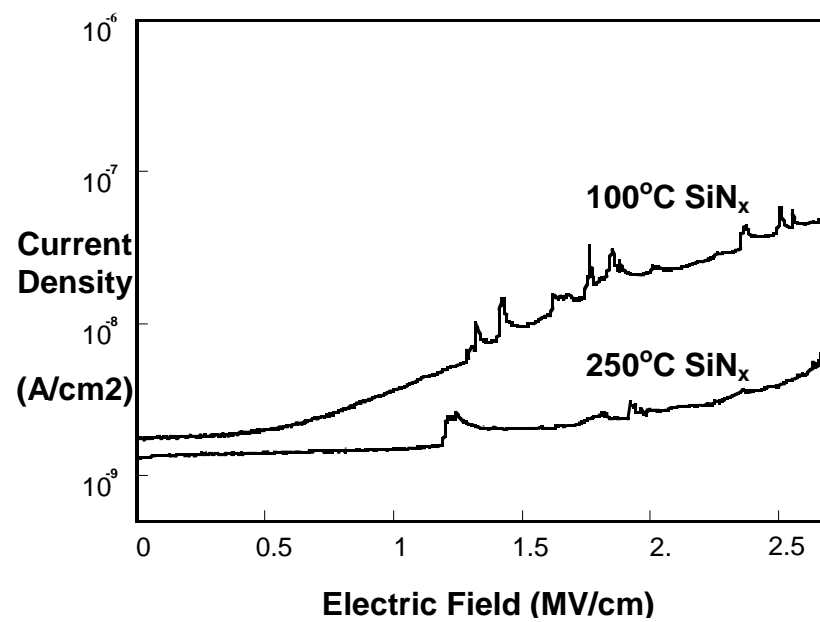


Figure 48. I-V characteristics of metal-insulator-semiconductor (MIS) structure (Al-SiN<sub>x</sub>-Si wafer).

The 250°C-deposited film has a lower leakage current of  $1.16 \times 10^{-9}$  Amp/cm<sup>2</sup> at 2.0 MV/cm, which is applicable for the TFT gate dielectric application. Therefore, SiN<sub>x</sub> film with different chemical and electrical properties could be deposited by varying process parameters, such as temperature and rf power.

## 2. Electrical Characteristics of a-Si:H TFT

Inverted staggered tri-layer a-Si:H TFTs were fabricated. The process and detailed condition were described in Chapter III. The SiN<sub>x</sub> film was optimized for the TFT. A-Si:H TFTs with various SiN<sub>x</sub> gate dielectric films were characterized.

Figure 49 shows the output characteristics of I<sub>ds</sub>-V<sub>ds</sub> curves of an a-Si:H TFT with SiN<sub>x</sub> (SiH<sub>4</sub>/NH<sub>3</sub>/N<sub>2</sub> 30/120/720 sccm) and a-Si:H (SiH<sub>4</sub> 70 sccm). The curves show no severe crowding phenomena, showing that the n<sup>+</sup> layer to intrinsic a-Si:H contacts is close to ohmic.<sup>16,17,48</sup>

Figure 50 shows the transfer characteristics of the same TFT in Fig. 49. The calculated field effect mobility is 0.127 cm<sup>2</sup>/Vs, and the V<sub>th</sub> is 5.944 V with a channel width of 39 μm and a channel length of 88 μm. The measurements were done after one hour annealing at 250°C in atmosphere because it has been reported that the plasma radiation from RIE can increase the TFT threshold voltage and leakage current by damaging the gate dielectric film and the top and bottom interfaces.<sup>47</sup> After the annealing, no V<sub>th</sub> shift and anomalous high leakage current due to RIE process were detected. Interface property between a-Si:H and SiN<sub>x</sub> film is another factor to determine electrical characteristics of a-Si:H TFT.



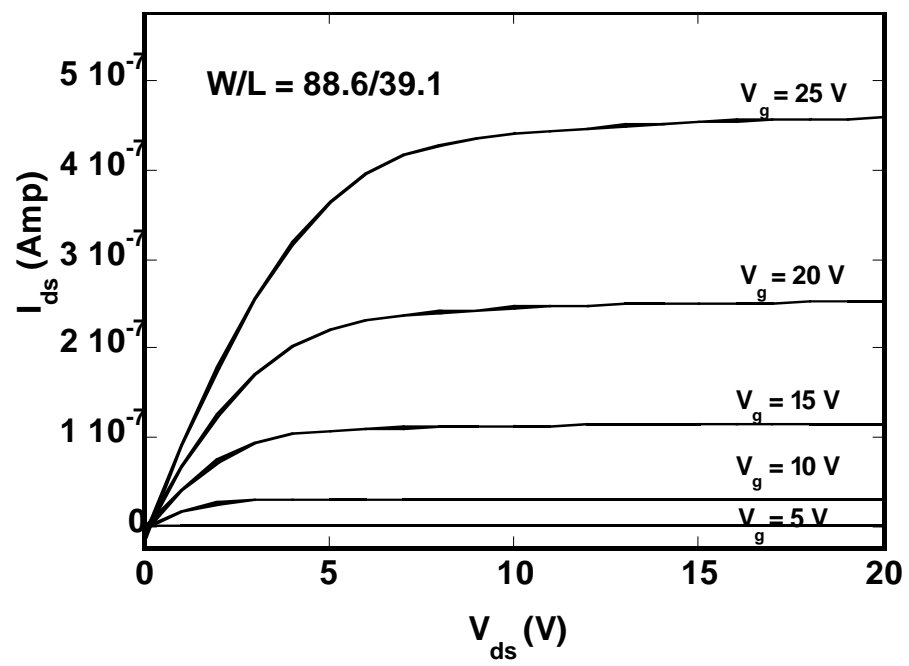


Figure 49. Output characteristics of an a-Si:H TFT,  $I_{ds}$  vs.  $V_{ds}$ .

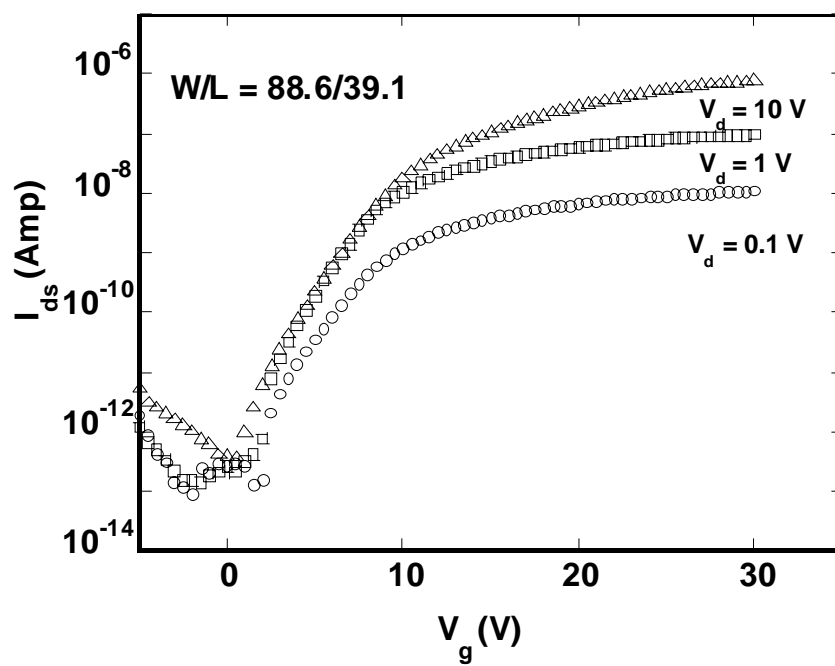


Figure 50. Transfer characteristics of an a-Si:H TFT,  $I_{ds}$  vs.  $V_g$ .

For example, the TFT mobility decreases with the increase of the roughness of the  $\text{SiN}_x$  surface.<sup>16,29</sup> A rough surface can cause a wide tail state and a high defect density at the interface.<sup>17</sup> At a fixed power of the a-Si:H deposition, the interface property between the a-Si:H and  $\text{SiN}_x$  layers is determined by the  $\text{SiN}_x$  deposition process.<sup>16,48</sup> The inverted staggered TFT, when the a-Si:H is deposited on top of the  $\text{SiN}_x$ , usually has better performance than a TFT of a reverse sequence-deposited structure. It is because the inverted staggered TFT has lower band energy and less stress mismatch at the interface.<sup>16,17</sup>

Figure 51 shows the general relationships between the refractive index (RI) of gate  $\text{SiN}_x$  and corresponding TFT threshold voltage,  $V_{\text{th}}$ . There are two graphs with different tri-layer deposition conditions. Fig. 51(a) is from PECVD deposition with 50 kHz (low frequency) rf power, and Fig. 51(b) is from PECVD deposition with 13.56 MHz (high frequency) rf power.<sup>29,48,49</sup> The graph of the 13.56 MHz rf source is replotted from ref. 29. The two graphs have different a-Si:H deposition conditions and TFT channel width/length (W/L: 88/39  $\mu\text{m}$  vs. 100/16  $\mu\text{m}$ ). However, Fig. 51(a) and (b) simultaneously show that a small range of refractive indices, *i.e.*, 1.87-1.89 or 1.85-1.90, has the lowest values of  $V_{\text{th}}$ .<sup>16,29,49</sup> Though the two graphs show the same trend about the  $\text{SiN}_x$  RI vs.  $V_{\text{th}}$ , the low frequency condition has a higher overall  $V_{\text{th}}$  (4.7–7.6 V) than the high frequency  $V_{\text{th}}$  (2.0–4.5 V). This is probably due to more serious plasma damage of the low frequency at the interface of the a-Si:H and gate dielectric  $\text{SiN}_x$  than that of the high frequency.

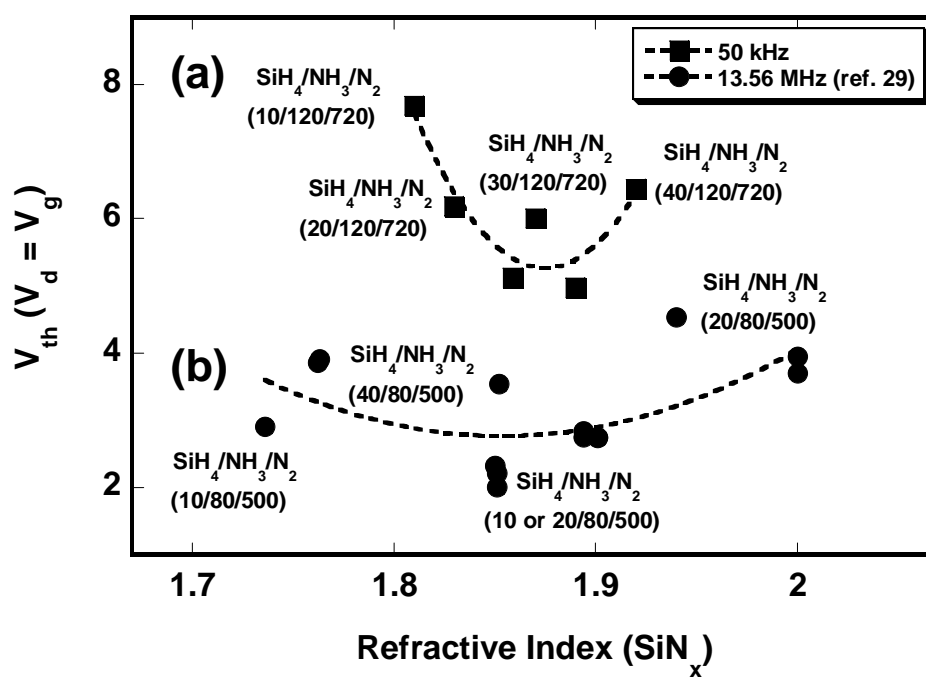


Figure 51. Refractive index effect on TFT threshold voltage  $V_{th}$ , PECVD SiN<sub>x</sub> at 500 mTorr, 250°C (reference<sup>29</sup>).

The TFT prepared from the 50 kHz PECVD process has the lowest  $V_{th}$  when the gate  $SiN_x$  was deposited from  $SiH_4/NH_3/N_2$  30/120/720 or 40/160/720 sccm, 500 mTorr, and 700 W. The RI of the  $SiN_x$  film increases with the increase of the  $SiH_4$  flow rate when the  $NH_3$  and  $N_2$  flow rates are fixed. This is due to the increase of the Si-Si bond in the film.<sup>24</sup> Therefore, the  $SiH_4$  flow rate in the  $SiN_x$  deposition process can affect the  $V_{th}$  of the a-Si:H TFT.

Figure 52 shows the RI of the gate  $SiN_x$  vs. the field effect mobility of TFT. The TFT with the highest  $\mu_{eff}$  occurs with the  $SiN_x$  gate dielectric RI in the range of 1.87 to 1.90. The same TFT also has a lower  $V_{th}$  than other TFTs, as shown in Fig. 51.

Figure 53 shows the ratio of  $I_{on}/I_{off}$  with respect to the RI of  $SiN_x$ . The  $I_{on}$  current was measured at  $V_d = 10$  V and  $V_g = 30$  V. The  $I_{off}$  was measured at the minimum current at  $V_d = 10$  V and  $V_g = -5$  V - 0 V. Typically, the requirement for an a-Si:H TFT is to have the  $I_{on}/I_{off}$  ratio above  $10^6$ .<sup>16</sup> From Fig. 53, the  $SiN_x$  gate dielectric film deposited from  $SiH_4/NH_3/N_2$  30/120/720 or 40/160/720 sccm shows the maximum  $I_{on}/I_{off}$  ratio. Therefore, both two films could be used as the gate dielectric of a high-performance a-Si:H TFT.

The  $SiH_4$  gas flow rate for a-Si:H deposition influences the TFT threshold voltage and field effect mobility at a fixed pressure of 250 mTorr. As the  $SiH_4$  flow rate increases, the  $V_{th}$  decreases and the mobility increases. Particle formation during a-Si:H deposition is critical to the performance of TFT. When the gas flow rate is high, the residence time of reactive radicals will be short in order to reduce the chance of forming a-Si:H particles which will deteriorate the morphology of a-Si:H film.<sup>21,24</sup>

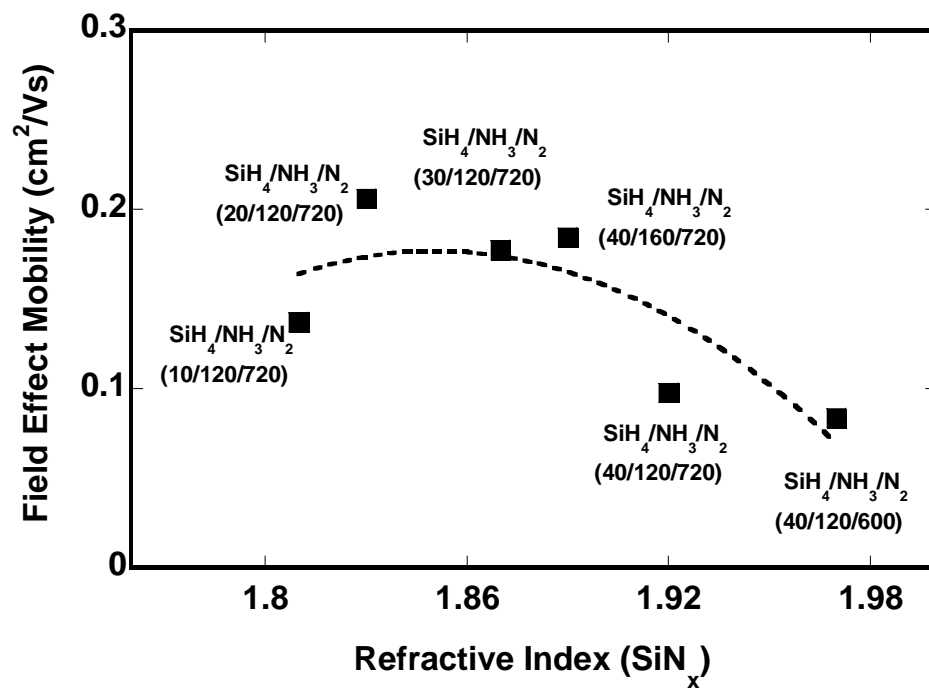


Figure 52. Refractive index effect on TFT field effect mobility  $\mu_{\text{eff}}$ , at 500 mTorr, 250°C.

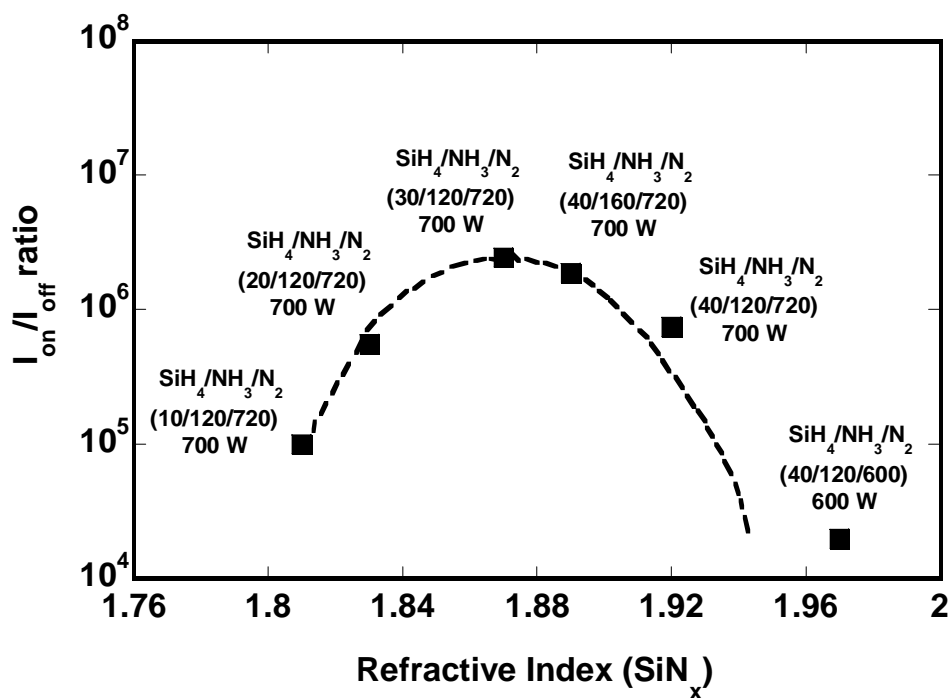


Figure 53. Refractive index effect on TFT  $I_{on}/I_{off}$  ratio, PECVD  $SiN_x$  at 500 mTorr, 250°C.

The TFT characteristics are dominated by the first 100 Å of the a-Si:H layer adjacent to the gate dielectric interface.<sup>48</sup> If the content of hydrogen in a-Si:H is low, a

large number of dangling bonds are formed at the a-Si:H/SiN<sub>x</sub> interface, which results in a high density of interface states. The high defect density represents low field effect mobility and high threshold voltage.<sup>17,29,47,48,50</sup> To increase the content of hydrogen at surface, H<sub>2</sub> plasma can be used.<sup>48</sup> However, the H<sub>2</sub> plasma can not only passivate dangling bonds, but also selectively etch the N containing group in the SiN<sub>x</sub> layer.<sup>28,29</sup> Therefore, the H<sub>2</sub> plasma process needs to be optimized in order to obtain the best TFT characteristics.<sup>49,50</sup>

### 3. Electrophoresis of TFT-Connected Microchannel Device

An a-Si:H TFT can be connected to the microchannel electrophoresis device to stabilize the current. In principle, the microchannel electrophoresis functions as a variable resistor of which the resistance increases drastically with the arrival of a protein to the detection electrode. Since the a-Si:H TFT could be fabricated at a low temperature, the entire TFT-microchannel electrophoresis system could be fabricated on various substrates.

The channel of device was made of a SU-8 sidewall and SiN<sub>x</sub> bottom surface with a depth of 30 μm, width of 500 μm, and length of 0.5 cm, as previously described in Chapter III. To improve PAGel affinity to the SU-8 channel surface, the microchannel device was treated with O<sub>2</sub> plasma by RIE with O<sub>2</sub> 5 sccm at 100 mTorr, 100 W, and room temperature.

Figure 54 shows (a) an inverted staggered tri-layer a-Si:H TFT connected to the microchannel device, and (b) the equivalent circuit. The TFT (W/L: 88/40 μm) has a



field effect mobility of  $0.127 \text{ cm}^2/\text{Vs}$  measured at the saturation  $I_d$  current region, a  $V_{th}$  of  $5.944 \text{ V}$ , and a leakage current ( $I_{off}$ ) below  $10^{-12} \text{ Amp}$ .

Figure 55 shows I-t curves of (a) the TFT alone, (b) the TFT-connected gel-filled microchannel with no protein in the feed reservoir, and (c) the TFT-connected gel-filled microchannel with protein in the feed reservoir. The three TFTs in Fig. 55 were operated under a gate bias of  $40 \text{ V}$  for a long period of  $2400 \text{ sec}$ . The  $I_{ds}$  decreases with time. Since the interface quality decays exponentially with time, the current of the TFT alone, or the TFT gel-filled microchannel system, decreases with  $\log t$ .<sup>51,52</sup> After the  $4800 \text{ sec}$  operation, the  $V_{th}$  shift was increased to  $14.8 \text{ V}$ . For the protein-loaded TFT-microchannel system, the current shows drastic drops for each size of protein arrival on the detection electrode. In addition, as the total resistance of the system sequentially increases associated with the gel-filled microchannel and protein sample loading, the current range also decreases.

Without a TFT, the I-t curve fluctuated drastically at the beginning of the operation, *e.g.*,  $t < 300 \text{ sec}$ .<sup>11</sup> The same phenomenon was also reported by others.<sup>7</sup> There are many possible causes for this fluctuation. For example, the system was not equilibrated when the voltage was initially applied. During the electrophoresis, the voltage drop between the two reservoirs of the microchannel is the total applied voltage minus the  $V_{ds}$  of the TFT. In this study, the voltage drop contributed by the TFT was very small, *i.e.*,  $0.02 \text{ V}$ , even after the  $2400 \text{ second}$  operation.

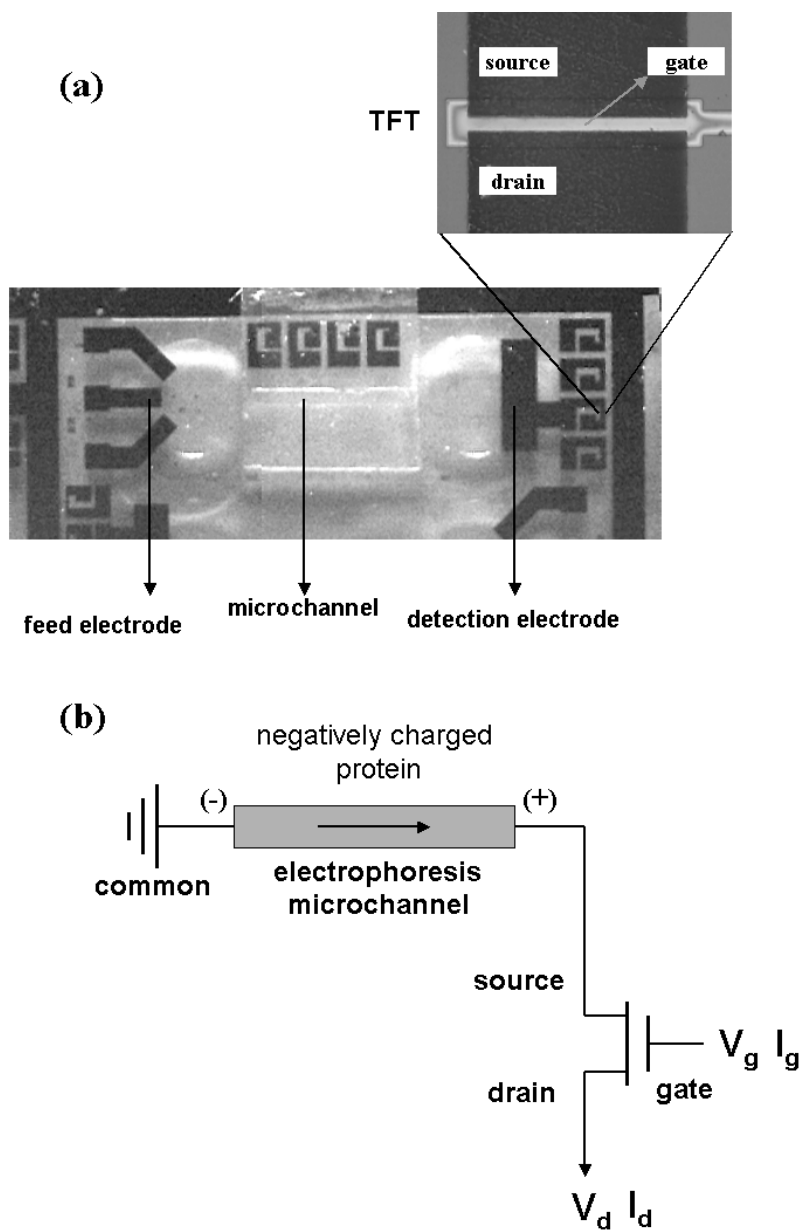


Figure 54. TFT-connected microchannel device: (a) an inverted staggered tri-layer a-Si:H TFT-connected to the microchannel device, and (b) the equivalent circuit.

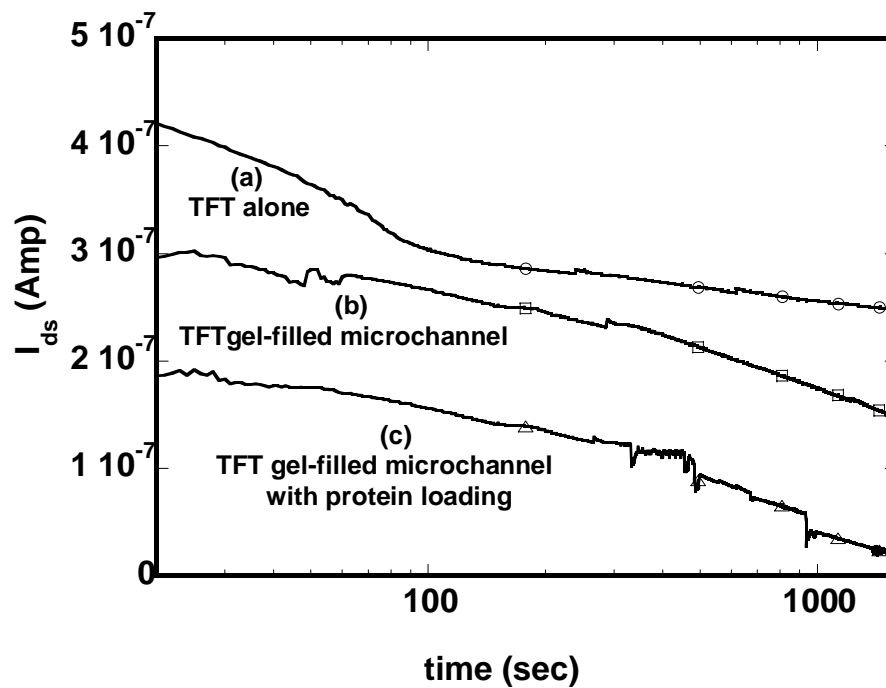


Figure 55. The I-t curves of (a) the TFT alone, (b) the TFT-connected gel-filled microchannel with no protein in the feed reservoir, and (c) the TFT-connected gel-filled microchannel with protein in the feed reservoir.

The voltage drop by the TFT could be either directly measured (0.02) or calculated by subtracting the total applied voltage (10 V) by the voltage drop between the two

reservoirs of the microchannel (9.98 V) through a separate measurement. Therefore, the applied voltage between the two electrophoresis electrodes was almost constant, *i.e.*, close to 10 V.

Figure 56 shows the  $dI/dt-t$  curves of (a) a gel-filled microchannel device of which the channel was formed from a Si trench, (b) a gel-filled microchannel electrophoresis device of which the channel wall was made of SU-8 and the channel bottom was made of  $\text{SiN}_x$  and was oxidized, and (c) the (b) microchannel device connected to a-Si:H TFT. The Si-based microchannel device of Fig. 56(a) has a sputtered  $\text{SiO}_x$  surface at the channel region. Both the SU-8 microchannel devices of Fig. 56(b) and (c) have a PECVD  $\text{SiN}_x$  surface at the channel bottom region and a SU-8 surface at the channel sidewall. The protein mobility decreases with the increase of its molecular weight. These results are consistent with those of the conventional electrophoresis. In addition, a very low electric field was applied in this experiment, *i.e.*, 10 V/cm, while the literature's micro-devices were often operated at a high field, *e.g.*, 100-600 V/cm.<sup>4-7</sup> The peak intensity of a TFT-connected system has a ( $dI/dt$ ) at least one order of magnitude lower than that of a device without a TFT. When the TFT is connected into microchannel electrophoresis, the current level is confined and regulated to the level of the TFT performance because the TFT is a voltage-driven device. Since the peak time for protein detection was after 300 sec, the decay of the  $\text{SiN}_x$ /a-Si:H interface quality of the TFT would be significant with that period as discussed in Fig. 55.

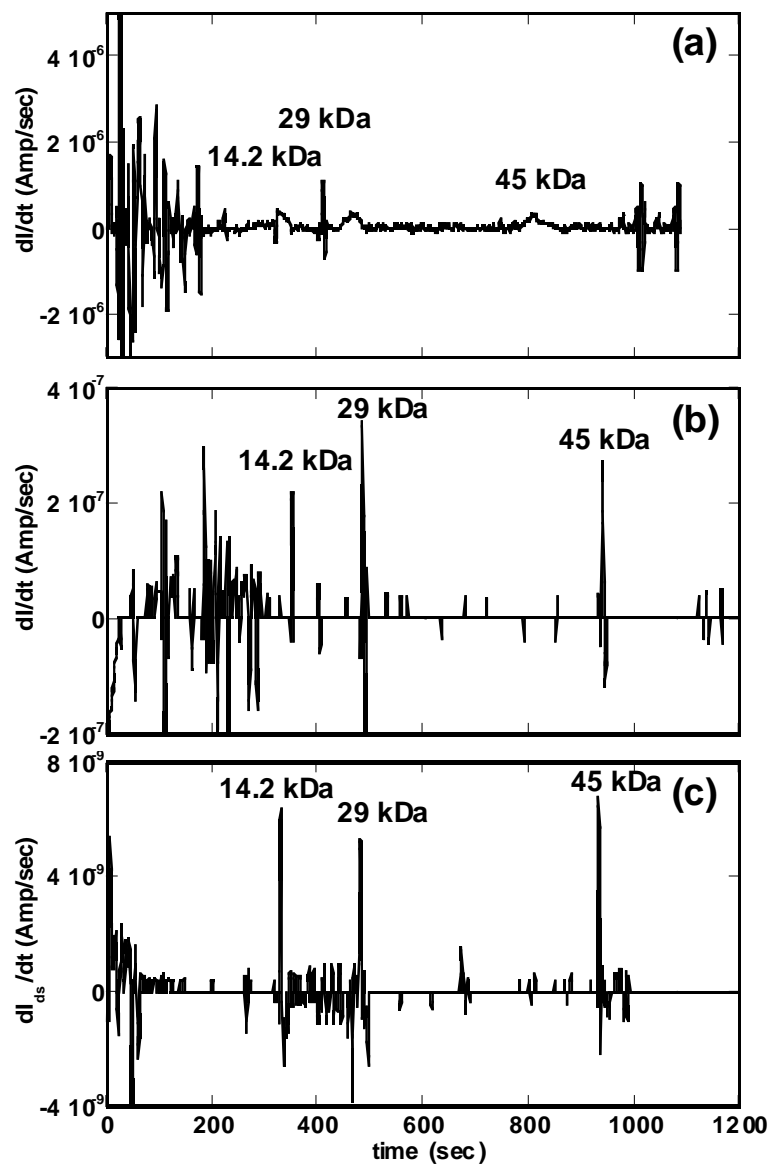


Figure 56. The  $dI/dt$ - $t$  curves: (a) a gel-filled Si-based microchannel device, (b) a gel-filled SU-8 microchannel device, and (c) a gel-filled SU-8 microchannel device connected to a TFT.

Therefore, when the protein is separated on the microchannel device alone without a

TFT, the entire current's readings are high.

Figure 56 clearly shows that the addition of a TFT improves the performance of electrophoresis by removing the severe initial current perturbation. Since Fig. 56(b) and (c) contain the same kind of microchannels, the peak times for the three proteins are the same. The migration speeds of  $\alpha$ -lactalbumin (14.2 kDa), carbonic anhydrase (29 kDa), and ovalbumin (45 kDa) are estimated to be 5.5, 3.8, and 1.9 cm/hour under 10 V/cm. The migration speeds of the Si-based microchannel, *i.e.*, Fig. 56(a), are 5.4, 3.85, and 2.22 cm/hour under 11.8 V/cm, separately.

Figure 57 shows the protein mobility *vs.* the molecular weight of protein in (a) a slab-type SDS-PAGE, (b) a gel-filled Si-based microchannel device, (c) a gel-filled SU-8 microchannel electrophoresis device, and (d) a gel-filled SU-8 microchannel electrophoresis device connected to an a-Si:H TFT. For the same protein, the mobility is the same in all three microchannel devices. The mobility in the microchannel is higher than that in the conventional slab-type because of the band curving, as discussed in Chapter V. The microchannel with the SU-8 structure has much lower noise intensity than the Si-based microchannel. This difference comes from the properties of channel surfaces. The Si-based microchannel has the sputtered  $\text{SiO}_x$  surface at the channel's bottom, while the TFT microchannel has the PECVD  $\text{SiN}_x$  at the channel's bottom and the SU-8 surface at the channel's sidewall. For example, the differences of surfaces can determine the extent of forming electro-osmotic flow (EOF), which affects the current noise during the microchannel electrophoresis.<sup>3,7</sup>

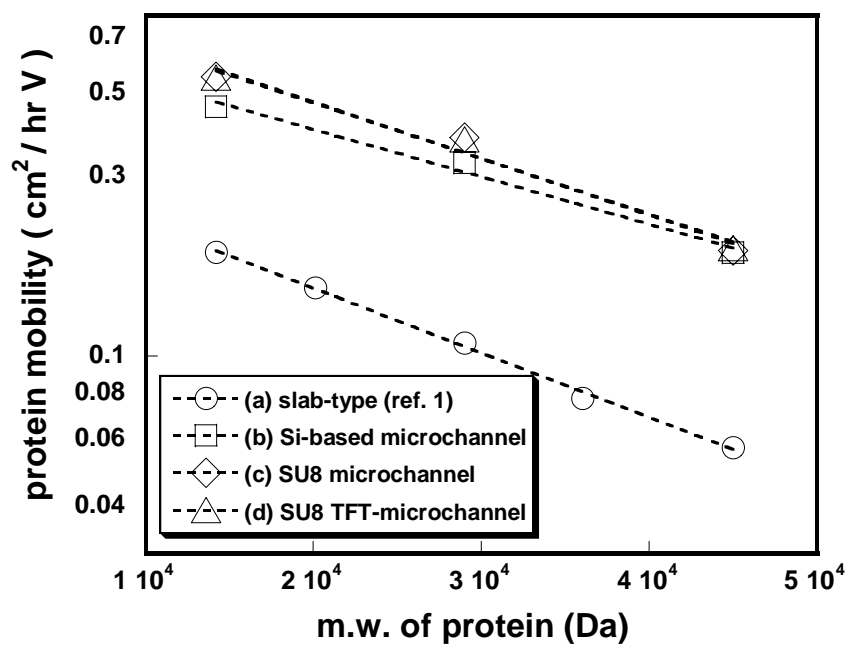


Figure 57. The protein mobility vs. the molecular weight of protein by electrophoresis: (a) a slab-type SDS-PAGE (reference<sup>1</sup>), (b) a gel-filled Si-based microchannel device, (c) a gel-filled SU-8 microchannel electrophoresis device, and (d) a gel-filled SU-8 microchannel electrophoresis device connected to the TFT.

The mobilities of proteins in both Si-based and SU-8 microchannel are higher than those of the slab-type electrophoresis.<sup>2,3</sup> This also indicates that the microchannel device improved the mobility of protein, as proven in Chapter V with the Si-based microchannel. Therefore, the TFT-connected microchannel device with the SU-8 sidewall and SiN<sub>x</sub> bottom surface proved highly efficient.



## CHAPTER VII

### CONCLUSIONS

In this dissertation, proteins were separated and identified with a microchannel electrophoresis device. DNA fragments were separated and identified with a similar microchannel surface electrophoresis. Fabrication methods of the microchannel device were investigated in detail. Experimental results showed that the device could be explained with a simple contact resistance model.

This dissertation was organized in the following way: Chapters I and II included background knowledge of the electrophoresis of protein and DNA, plasma process, PECVD films, and a-Si:H TFTs. Chapter III studied physical, chemical, and electrical characterization of the microchannel device, as well as the fabrication method. Chapter IV focused on modification of the microchannel surface. Chapter V included results on the electrophoresis of protein and DNA. Chapter VI was for the process of PECVD SiN<sub>x</sub> deposition and the device's electrical characteristics of the corresponding a-Si:H TFT. Based on these discussions, an a-Si:H TFT-driven electrophoresis for protein separation and identification was examined.

In Chapter I, a conceptual introduction of electrophoresis and challenges associated with capillary or microchip electrophoresis were discussed. The development trend of the capillary or microchip electrophoresis system by LIF was included and then, the basic applications of a-Si:H TFTs were given.

In Chapter II, the theoretical background of the electrophoresis, the basic mechanism of the capillary or microchip electrophoresis by LIF, and practical requirements for protein and DNA electrophoresis were discussed and then, the basic principles of plasma process and the applications of PECVD thin films for a-Si:H TFT fabrication were discussed. Typical electrical characteristics of a-Si:H TFT were also represented.

In Chapter III, the experimental setup, fabrication methods, characterization techniques, corresponding fundamental theories, and numerical methods were explained in detail. The fabrication process of the microchannel included metal (Mo, Cr) sputtering, the photomask process with PR, anisotropic Si etching by KOH, the negative photomask SU-8 process, PECVD deposition of a-Si:H and SiN<sub>x</sub>, n<sup>+</sup> etching by RIE, and oxidation or hydrogenation by plasma or solution. The characterization techniques and theories included ellipsometer, ESCA, FT-IR, and SEM; and electrical analysis included I-t, dI/dt-t, I<sub>ds</sub>-V<sub>d</sub>, and I<sub>ds</sub>-V<sub>g</sub>.

In Chapter IV, it was shown that the efficiency of the microchannel devices was mainly determined by the surface property of the device. The first part of the chapter discussed the relationship between the contact angle and the surface modification methods using a protein solution as the example. Several conclusions were drawn: (i) surface modification of a polymer was helpful for protein electrophoresis by increasing the surface wettability, (ii) most substrates except plain glass were suitable for the microchannel surface from the protein adsorption examination, and (iii) surface interaction between the gel or protein and the substrates could be monitored by the

contact angle measurement. The second part of the chapter dealt with the relationship between a protein solution's contact angle and the modified surface. The following conclusions were drawn: (i) for silicon containing surfaces, the chemical bond state of silicon confirmed by ESCA determined the contact angle of a DNA solution, (ii) for non-interacting surfaces with DNA, the concentration of solute determined the DNA affinity by changing viscosity of solution.

The first part of Chapter V presented the new microchannel device for protein electrophoresis with different configurations. Different channel structures with and without gel filling and protein existence were investigated based on the resistance model. Solutions containing three different sizes of proteins were separated with this new device. There was a peak in the  $dI/dt-t$  curve for each protein because of the increase of the contact resistance during the adsorption of protein on the detection electrode surface. Proteins could be separated at a higher rate with the new device than with the conventional slab-type electrophoresis. A high separation and detection efficiency was obtained with a large cross-sectional area of the microchannel and a small detection electrode. The mobility of protein increases with the increase of the channel's cross-sectional area. The second part of the chapter investigated that the separation and identification of DNA fragments using the new type of surface electrophoresis device. DNA fragments were separated based on the mobility difference along the channel bottom surface. Based on the contact angle measurement and surface chemical analysis, the oxidized silicon and glass were found to be suitable materials for the bottom substrates. The channel surface structure, which could be changed by various solution or

plasma treatments, was a key factor affecting the separation efficiency. The ionic strength of the DNA buffer solution was also critical to the separation efficiency.

The first part of Chapter VI was dedicated to analysis of the process parameters of PECVD  $\text{SiN}_x$ , *i.e.*, gas flow rate, temperature, and rf power, which determined RI, Si-H/N-H ratio, Si/N ratio, etching rate, and leakage current of the  $\text{SiN}_x$  films. The second part included relationships between the RI of  $\text{SiN}_x$  and a-Si:H TFT characteristics, *i.e.*,  $V_{\text{th}}$ ,  $\mu_{\text{eff}}$ , and  $I_{\text{on}}/I_{\text{off}}$  ratio. It was found that a TFT with a gate  $\text{SiN}_x$  RI in the range of 1.87 to 1.90 has the lowest  $V_{\text{th}}$ , the highest  $\mu_{\text{eff}}$ , and the highest  $I_{\text{on}}/I_{\text{off}}$  ratio. The third part concluded that, when an a-Si:H TFT is connected to the microchannel device, a unique operational principle was observed. Solutions containing multiple proteins were separated and identified with this new TFT-connected microchannel device. An improved device performance was achieved by removing undesirable current (I) perturbations, which typically exist during the microchannel electrophoresis. The TFT connected to the microchannel acted as a current regulator to reduce signal noise from the detection electrode. Therefore, the introduction of the TFT to a microchannel electrophoresis device makes its system more stable and reliable.

In summary, new conceptual microchannel devices for protein and DNA electrophoresis have been developed and discussed. Separation and identification of protein or DNA were clearly realized in the devices. The performance and efficiency of these kinds of devices were improved with a microelectronic device such as a-Si:H TFT.

## REFERENCES

1. B. D. Hames and D. Rickwood, *Gel Electrophoresis of Proteins: A Practical Approach*, B. D. Hames, Editor, p. 4, Oxford University Press, Oxford, UK (1990).
2. J. Sambrook, E. F. Fritsch and T. Maniatis, *Molecular Cloning: A laboratory manual*, Cold Spring Harbor Laboratory Press, New York (1989).
3. P. Camilleri, *Capillary Electrophoresis, Theory and Practice, 2<sup>nd</sup> Ed.*, P. Camilleri, Editor, p. 364, CRC Press, Boca Raton, FL (1998).
4. A. D. Woolley and R. A. Mathies, *Proc. Natl. Acad. Sci. USA*, **91**, 11348 (1994).
5. S. Yao, D. S. Anex, W. B. Caldwell, D. W. Arnold, K. B. Smith and P. G. Schultz, *Proc. Natl. Acad. Sci. USA*, **96**, 5372 (1999).
6. C. L. Coyler, S. D. Mangru, D. J. Harrison, *J. Chromatogr A*, **781**, 271 (1997).
7. Y. Liu, R. S. Foote, C. T. Culbertson, S. C. Jacobson, R. R. Ramsey, J. M. Ramsey, *J. Microcolumn Sep*, **12**, 407 (2000).
8. S. B. Brahmasandra, V. M. Ugaz, D. T. Burke, C. S. Mastrangelo, M. A. Burns, *Electrophoresis*, **22**, 300 (2001).
9. Y. Kuo and H. H. Lee, in *Proc. SPIE Conf. Micorfluidics and BioMEMS*, C. H. Mastrangelo and H. Becker, Editors, p. 102, **4560**, Bellingham, WA (2001).
10. Y. Kuo and H. H. Lee, *Electrochem. Solid St.*, **4**, H23 (2001).
11. H. H. Lee and Y. Kuo, in *Proc. 1st IEEE conf. Sensors*, F. Maloberti and J. R. Vig, Editors, p. 454, **2**, Piscataway, NJ (2002).
12. B. Guo, J. Anzai and T. Osa, *Chem. Pharm. Bull.*, **44**, 800 (1996).

13. N. R. Cabilio, S. Omanovic and S. G. Roscoe, *Langmuir*, **16**, 8480 (2000).
14. S. M. MacDonald and S. G. Roscoe, *J. Colloid. Int. Sci.*, **184**, 449 (1996).
15. R. Foerch, N. S. McIntyre, D. H. Hunter, *J. Appl. Polymer Sci. A*, **28**, 193 (1990).
16. Y. Kuo, *Amorphous Silicon Thin Film Transistors*, Y. Kuo, Editor, p. 187, Kluwer Academic Publishers, Norwell, MA (2004).
17. Y. Kuo, *J. Electrochem. Soc.*, **142**, 2486, (1995).
18. R. A. Street, *Technology and Applications of Amorphous Silicon*, R. A. Street, Editor, p. 4, Springer-Verlag, Berlin, Germany (2000).
19. N. Pernodet, V. Samuilov, K. Shin, J. Sokolov, M. H. Rafailovich, D. Gersappe, and B. Chu, *Phy. Rev. Lett.*, **85**, 5651 (2000).
20. Y. -S. Seo, V. A. Samuilov, J. Sokolov, M. Rafailovich, B. Tinland, J. Kim and B. Chu, *Electrophoresis*, **23**, 2618 (2002).
21. S. A. Campbell, *The Science and Engineering of Microelectronics Fabrication*, Oxford University Press, Oxford, UK (1996).
22. M. A. Lieberman and A. J. Lichtenberg, *Principles of Plasma Discharges and Materials Processing*, John Wiley & Sons, Ltd., New York (1994).
23. S. K. Ghandhi, *VLSI Fabrication Principles, Silicon and Gallium Arsenide*, John Wiley & Sons, Ltd., New York (1994).
24. A. R. Reinberg, *J. Electronic. Mat.*, **8**, 345, (1979).
25. W.S. Liao and S.C. Lee, *J. Electrochem. Soc.*, **144**, 1477, (1997).
26. T. M. Klein, T. M. Anderson, A. I. Chowdhury, and G. N. Parsons, *J. Vac. Sci. Technol. A*, **17**, 108, (1999).

27. S. Bae, D. G. Farber and S. J. Fonash, *Solid State Electronics*, **44**, 1355, (2000).
28. Y. Kuo, *Appl. Phys. Lett.*, **63**, 144, (1993).
29. Y. Kuo, *J. Electrochem. Soc.*, **142**, 186, (1995).
30. B. G. Streetman and S. Banerjee, *Solid State Electronic Devices*, Prentice Hall Inc., Upper Saddle River, NJ (2000).
31. H. G. Tompkins, W. A. McGahan, *Spectroscopic Ellipsometry and Reflectometry - A User's Guide*, John Wiley & Sons, Ltd., New York (1999).
32. J. F. Moulder, W. F. Stickle, P. E. Sobol and K. D. Bomben, *Handbook of X-ray Photoelectron Spectroscopy*, Perkin-Elmer Corp., Eden Prairie, MN (2000).
33. J. C. Vickerman, *Surface Analysis – The Practical Techniques*, John Wiley & Sons, Ltd., New York (1997).
34. H. Gunzler and H. -U. Gremlich, *IR Spectroscopy – An Introduction*, Wiley-VCH Verlag, Berlin, Germany (2002).
35. A. Savitzky and M. J. E. Golay, *Anal. Chem.*, **8**, 1627 (1964).
36. S. M. Sze, *Semiconductor Sensors*, John Wiley & Sons, Ltd., New York (1994).
37. S. A. Campbell, K. Cooper, L. Dixon, E. Earwaker, S. N. Port and D. J. Schiffrin, *J. Micromech. Microeng.*, **5**, 209 (1995).
38. J. M. Shaw, J. D. Gelorme, N. C. LaBianca, W. E. Conley and S. J. Holmes, *IBM J. Res. Develop.*, **41** (1997).
39. C. C. Dupont-Gillain, Y. Adriaensen, S. Derclaye, P. G. Rouxhet, *Langmuir*, **16**, 8194 (2000).

40. T. Kobayashi, T. Sasama, H. Wada and N. Fujii, *J. Vac. Sci. Technol. A*, **19**, 2155 (2001).
41. B. L. Johansson, A. Larsson, A. Ocklind, A. Ohrlund, *J. Appl. Polymer Sci.*, **86**, 2618 (2002).
42. A. Larsson, H. Derand, *J. Coll. Int.Sci.*, **246**, 214 (2002).
43. R. W. B. Pearse and A. G. Gaydon, *The Identification of Molecular Spectra*, John Wiley & Sons, Ltd., New York (1963).
44. E. A. S. Doherty, K. D. Berglund, B. A. Buchholz, I. V. Kourkine, T. M. Przybycien, R. D. Tilton and A. E. Barron, *Electrophoresis*, **23**, 2766 (2002).
45. B. C. Giodarno, J. Ferrance, S. Swedberg, A. F. R. Huhmer and J. P. Landers, *Analytical Chemistry*, **291**, 1245 (2001).
46. J. Horvath and V. Dolnik, *Electrophoresis*, **22**, 644 (2001).
47. Y. Kuo, *Appl. Phys. Lett.* **61**, 2790 (1992).
48. Y. Kuo, *Appl. Phys. Lett.*, **67**, 2173 (1995).
49. Y. Kuo, *Vacuum*, **51**, 741 (1998).
50. Y. Kuo, *Vacuum*, **59**, 484 (2000).
51. J. Kakalios, R. A. Street and W. B. Jackson, *Phys. Rev. Lett.*, **59**, 1037 (1987).
52. M. J. Powell, C. van Berkel and J. R. Hughes, *Appl. Phys. Lett.*, **54**, 1323 (1989).



## APPENDIX

09/12/2004 SUN 22:15 FAX

001/001



**TEXAS A&M UNIVERSITY**  
 Department of Chemical Engineering  
 College Station, Texas 77843-3122  
 (409) 845-3361  
 FAX (409) 845-6446

August, 30, 2004

Permissions Request  
 The Electrochemical Society (ECS)  
 65 South Main Street  
 Pennington, NJ 08534, USA  
 Fax: 609-737-2743  
 E-mail: [copyright@electrochem.org](mailto:copyright@electrochem.org)

## To Whom It May Concern:

I am a doctoral student at Texas A&M University and am writing for permission to include in my dissertation part of the material from *Electrochemical and Solid-State Letters*, "Microchannel Electrophoresis Device for Separation and *In Situ* Detection of Proteins", Vol 4, No. 10, (2001), pp. H23-H25. The dissertation will be made available to the public on the Web through Texas A&M University Libraries. In addition, the dissertation will be microfilmed by UMI Dissertation Publishing (ProQuest Information and Learning), and copies of the dissertation will be sold on demand. Please supply a signed letter granting me permission to use the work. You can mail or fax the permission to:

Hyun Ho Lee  
 Dept. of Chemical Engineering  
 Texas A&M University  
 College Station, TX 77843-3122  
 FAX) 979-845-6446

If you need further information, please feel free contact me by phone 979-845-4489, or e-mail to [hyunho@tamu.edu](mailto:hyunho@tamu.edu).

Thank you very much for your effort in resolving this issue.

Sincerely,

Hyun Ho Lee

Permission is granted to include the above-referenced paper in your thesis, provided that you obtain permission of the other individual authors. In the thesis, please acknowledge the authors and the citation given above, and include the words: "Reproduced by permission of The Electrochemical Society, Inc."

13 Sept. 2004

Mary E. Vess, Deputy Executive Director



**TEXAS A&M UNIVERSITY**  
Department of Chemical Engineering  
College Station, Texas 77843-3122  
(409) 845-3361  
FAX (409) 845-6446

August, 30, 2004

Ms Helen Wilson (Manager)  
Science & Technology Rights Department  
Elsevier Ltd  
PO Box 800  
Oxford OX5 1DX, UK  
Fax: (+44) 1865-853333  
E-mail: [permissions@elsevier.com](mailto:permissions@elsevier.com)

To Whom It May Concern:

I am a doctoral student at Texas A&M University and am writing for permission to include in my dissertation part of the material from *Vacuum*, "Plasma-enhanced chemical vapor deposition of silicon nitride below 250°C", Vol 66, (2002), pp. 299-303. The dissertation will be made available to the public on the Web through Texas A&M University Libraries. In addition, the dissertation will be microfilmed by UMI Dissertation Publishing (ProQuest Information and Learning), and copies of the dissertation will be sold on demand. Please supply a signed letter granting me permission to use the work. You can mail or fax the permission to:

Hyun Ho Lee  
Dept. of Chemical Engineering  
Texas A&M University  
College Station, TX 77843-3122  
FAX) 979-845-6446

If you need further information, please feel free contact me by phone 979-845-4489, or e-mail to [hyunho@tamu.edu](mailto:hyunho@tamu.edu).

Thank you very much for your effort in resolving this issue.

Sincerely,

A handwritten signature in black ink that reads "Lee Hyun Ho".

Hyun Ho Lee



13 September 2004

Our ref: HG/SS/Sept 04/J083

Hyun Ho Lee  
Texas A&M University  
hyunho@tamu.edu

Dear Dr Lee

VACUUM, Vol 66, 2002, pp 299-303, "Plasma-enhanced chemical..."

As per your letter dated 30 August 2004, we hereby grant you permission to reprint the aforementioned material at no charge **in your thesis, in print and on the Texas A&M University web site** subject to the following conditions:

1. If any part of the material to be used (for example, figures) has appeared in our publication with credit or acknowledgement to another source, permission must also be sought from that source. If such permission is not obtained then that material may not be included in your publication/copies.
2. Suitable acknowledgment to the source must be made, either as a footnote or in a reference list at the end of your publication, as follows:  
  
"Reprinted from Publication title, Vol number, Author(s), Title of article, Pages No., Copyright (Year), with permission from Elsevier".
3. Reproduction of this material is confined to the purpose for which permission is hereby given.
4. This permission is granted for non-exclusive world **English** rights only. For other languages please reapply separately for each one required. Permission excludes use in an electronic form other than as specified above.
5. This includes permission for UMI to supply single copies, on demand, of the complete thesis. Should your thesis be published commercially, please reapply for permission.

Yours sincerely

Helen Gainford  
Rights Manager

Your future requests will be handled more quickly if you complete the online form at  
[www.elsevier.com/locate/permissions](http://www.elsevier.com/locate/permissions)

## VITA

Name            Hyun Ho Lee  
Address        95 Dong 107 Ho, Banpo APT, Banpobon-Dong 1245, Seocho-Ku, 137-813, Seoul, Republic of Korea

## Education

Mar. 1988 ~ Feb. 1992, B.S., Chemical Technology, Seoul National University, Seoul, Korea

Sep. 1997 ~ Aug. 1998, M.S., Chemical Engineering, Stanford University, California, U.S.A.

## Publications

1. M. Ristova, Y. Kuo, and H.H. Lee, *Appl. Surf. Sci.*, **218**, 44, (2003).
2. Y. Kuo and H.H. Lee, *Vacuum*, **66**, 299 (2002).
3. Y. Kuo and H.H. Lee, *Electrochem. Solid St.*, **4**, H23 (2001).

This dissertation was typed by Hyun Ho Lee.